Physical and mechanical properties study of CsI scintillation crystals and design of the mechanical structure for the Mu2e Electromagnetic Calorimeter at Fermilab

Author:
Daniele Pasciuto

Supervisors:
Prof. Matteo Martini

Dr. Stefano Miscetti

Dr. Luigi Montalto

Contents

Introduction

This Thesis presents the study of the mechanical and optical properties of the un-doped Cesium Iodide (CsI) crystals employed in the electromagnetic calorimeter of the muon-to-electron-conversion (Mu2e) experiment at Fermi National Accelerator Laboratory (Fermilab, US). This has required some tailored solution and procedures for crystal testing and investigation. In addition, critical mechanical parts have been carefully designed and developed since they are in contact and strongly interact with the crystals.

The Mu2e experiment is being developed at Fermilab by an international collaboration of universities, institutes of research and laboratories and will search for the neutrino-less coherent conversion of a muon into an electron in the field of an aluminum nucleus. The experimental goal is to improve the sensitivity of previous similar experiments by four orders of magnitude and reach a single event sensitivity of 3×10^{-17} on the conversion rate with respect to the muon capture rate in aluminum [1].

The sensitive material employed by the electromagnetic calorimeter is a matrix of 1348 un-doped CsI crystals that convert the impinging electron into an electromagnetic shower and ultimately into light through scintillation. To achieve the ambitious Mu2e physics goals, the selected crystals have to satisfy very high-quality standards in terms of geometrical, mechanical and physical properties. This has required development and implementation of a QC.

Since Cesium Iodide shows a slightly level of hygroscopicity and improper handling and storage may compromise the optical performance of the material, specific procedures have been developed for storage and manipulation.

Moreover, the cost of the material and the considerable amount of time necessary to replace a damaged unit, have posed rigorous constraints on the design of the mechanical parts that are placed in contact with the crystals to minimize the risk of damage during calorimeter assembly, installation and operation.

Additional constraints derive from the hostile Mu2e operation environment in terms of vacuum and radiation levels and magnetic field intensity.

This Thesis improves the current knowledge of several aspects of Cesium Iodide crystals performance stability and characteristics, including the study of the optical transmittance deterioration due to the exposure to a humid environment, propose procedures and systems for crystals assessment and investigations and the development of possible recovery procedures.

To perform these studies numerous research institutions have been involved, including the Italian National Institute of Nuclear Physics, Fermi National Accelerator Laboratory, the Università Politecnica delle Marche and the University of Pisa.

chapter 1 reports a brief description of the Fermilab Muon Campus and the Mu2e experiment.

chapter 2 describes the Mu2e electromagnetic calorimeter main components.

In chapter 3 a more detailed description of the calorimeter mechanical component is shown.

chapter 4 describes the procedures adopted for the Quality Assurance of the production CsI crystals; this includes a description of the set-up apparatus and the results of the crystals survey, with a detailed analysis of the major dimensional problems encountered. The description of the procedure adopted to build a column of crystals is reported along with the mathematical models employed to predict the actual envelope of the column after crystals stacking.

chapter 5 reports the study of the effect of humidity on CsI crystals, the description of the developed set-up used to measure the optical degradation and the possible crystals recovery methods based on crystals exposure to high temperatures in dry environment.

chapter 6 describes the Inner Cylinder design and the several employed FEM models.

chapter 7 shows the pressure contact effects on CsI crystals; the FEM analysis and the experimental set-up and experiments are thoroughly describes.

chapter 7.3 reports my conclusions on the work described in this Thesis.

Chapter 1

The Mu2e Experiment

This Chapter reports the physics motivations and experimental techniques employed by the muon to electron conversion experiment (Mu2e), located at the *Fermi National Accelerator Laboratory* (Illinois - USA). I also reported an overview of the Fermilab accelerator complex which provides the high intensity muon beam line, along with the necessary particle detectors. The Italian National Institute of Nuclear Physics (INFN), in collaboration with the California Institute of Technology (Caltech) and Fermilab, is responsible for the design and construction of the detector named *electromagnetic calorimeter*. At the moment of writing this Thesis, the calorimeter has been almost completely designed. The construction of some parts of the detector has begun in 2020 and they will be completed within spring 2021. The calorimeter assembling is expected to start in SiDet facility at Fermilab at the beginning of summer 2021, in order to be ready to installation in the first half of 2022, when commissioning data are expected to be taken.

1.1 The Standard Model

The theory named Standard Model of particle physics provides a satisfactory physical model to explain the phenomenology of three among the four known fundamental forces[1][2]. The model provides a satisfactory description of the interactions among elementary particles, and how they are mediated by a "relative exchange" of particles (Figure 1.1). Attempts to include the gravitational force in the Standard Model have not provided satisfactory results yet[2].
Although the Standard Model predictions have been experimentally verified with high precision, we know this theory is incomplete and needs an extension to incorporate phenomena such as *neutrino oscillations*[3] and the existence of *dark matter*[4] which have both been observed experimentally but have not yet found a fully satisfactory theoretical interpretation.

---

[1]The four fundamental forces are: the electromagnetic, the weak, the strong and the gravitational force. The gravitational is the only one not covered by the standard model

[2]The theory able to link together general relativity and quantum mechanics would be the so called "Theory of everything", that would fully explains and links together all the physical aspects of the universe

[3]Neutrino oscillation is a quantum mechanical phenomenon whereby a neutrino created with a specific lepton family number (lepton flavor: electron, muon, or tau) can later be measured having a different lepton family number.

[4]Dark matter is a form of matter thought to account for approximately 85% of the matter in the universe, and about a quarter of its total energy density. Its presence is implied in a variety of astrophysical observations, including gravitational effects which cannot be explained by accepted theories of gravity unless more matter is present than the visible one.

Figure 1.1: Summary table of the elementary constituents of matter, quarks, leptons and gauge bosons. (*Image courtesy of Fehling Dave*)

All the elementary constituents of matter can be classified according to two categories: *fermions*, i.e. quarks and leptons, the 1/2 spin[5] elementary constituents of matter, and *bosons*, the integer spin mediators of the fundamental forces. Fermions are classified according to their interactions (or equivalently, by what charges they carry). There are six quarks (up, down, charm, strange, top, bottom), and six leptons (electron, electron neutrino, muon, muon neutrino, tau, tau neutrino). Quarks carry color charge and interact via the strong interaction. A phenomenon called color confinement results in quarks being very strongly bound to each other, forming color-neutral composite particles (hadrons) containing either a quark and an antiquark (mesons) or three quarks (baryons). The familiar proton and neutron are the two baryons with the smallest masses. Quarks also carry electric charge and weak isospin. Hence, they interact with other fermions both electromagnetically and via the weak interaction. The remaining six fermions are called leptons and do not carry color charge. The three neutrinos do not carry electric charge either, so their interactions are limited to the weak force, which makes them notoriously difficult to detect. However, by virtue of carrying an electric charge, the electron, muon, and tau all interact electromagnetically and weakly. The six quarks and leptons are grouped into three families.
The the first generation of quarks includes:

- The quark up

- The quark down

The second one contains:

- The quark strange

- The quark charm

---

[5]In quantum mechanics the spin is an intrinsic form of angular momentum carried by elementary particles, composite particles (hadrons), and atomic nuclei.

And finally the third one contains

- The quark top

- The quark bottom

The first generation of leptons includes:

- The electron e

- The electron neutrino ν_e

The second one contains the muonic leptons:

- The muon μ

- The muon neutrino ν_μ

And finally, the third one, containing the tauonic leptons:

- The tau τ

- The tau neutrino ν_τ

Each member of a generation has greater mass than particles belonging to lower generations. Ordinary matter (i.e., atoms, neutrons, and protons) is made of particles belonging to the first generation. Specifically, all atoms consist of electrons orbiting around atomic nuclei, ultimately constituted of up and down quarks. The second and third generation charged particles, on the other hand, decay with very short half-lives and are observed only in very high-energy environments. Neutrinos of all generations also do not decay, the pervade the universe and rarely interact with other particles.

In the Standard Model, bosons are defined as force carriers that mediate the strong, weak, and electromagnetic fundamental interactions. The interactions in physics are the ways in which the particles influence other particles. The Standard Model explains such forces as resulting from elementary particles exchanging other particles, generally referred to as force mediating particles (i.e., the bosons), as listed below:

- The photons γ, that mediate the electromagnetic force between charged particles. They are mass-less;

- The W^+,W^- and Z bosons mediate the weak interactions between particles of different flavors. They are massive;

- The eigth *gluons* mediate the strong interactions between color charged particles (the quarks). They are mass-less and with an effective color charge, hence they can also interact among themselves;

- The *Higgs particle* is a massive scalar elementary particle theorized by Peter Higgs in 1964. It plays a unique role in the Standard Model, explaining why the other elementary particles, except the photon and gluon, are massive. In particular, the Higgs boson explains why the photon has no mass, while the W and Z bosons are very heavy. Higgs discovery of CERN Large Hadron Collider has been a recent triumph of the Standard Model [3][4].

1.1.1   Charged lepton flavor violation (CLFV)

The muon and tau are unstable particles, while the electron is stable. The muon decays with a probability of approximately 100% to a muon neutrino ν_μ, an electron e, and an electron antineutrino $\bar{\nu}_e$[6]. In symbols the previous physics process can be indicated as $\mu \to \nu_\mu e \bar{\nu}_e$.

In a small fraction of cases, also other particles with a net charge equal to zero may be produced in the muon decay (e.g., a photon, or an electron-positron[7]pair). In all these processes the lepton flavor is conserved separately for every lepton family. In other words, the final state includes a muon neutrino, which belongs to the same family and has the same lepton number as the parent muon, and also an electron and an electron antineutrino, which have zero lepton number in total, since particles and antiparticles are conventionally assigned opposite lepton numbers.

Searches for Charged Lepton Flavor Violating processes, such as the muon to electron conversion ($\mu \to e\gamma$)[8], with no muon neutrino, nor electron antineutrino in the final state, have so far yielded null results. CLFV processes are expected within the Standard Model with a probability $<10^{-54}$. With the current level of experimental precision, such effects are obviously beyond the experimental reach. Although the Standard Model has been accurately tested, we know it is an incomplete theory. Several extensions of the model include CLFV processes and allow the decay $\mu \to e\gamma$, and also the *coherent neutrino-less muon conversion to an electron in the field of a nucleus* ($\mu N \to eN$), with probability rates sufficient to be measured in the next generation experiments, including Mu2e.

Mu2e has been designed and is currently being constructed at Fermilab to search for the neutrino-less muon conversion to an electron in the field of an aluminum nucleus. The current experimental limit on the branching factor of this process has been set at the level of 10^{-12} by the SINDRUM II experiment [5], performed at the Paul Scherrer Institut at Zurich. The Mu2e sensitivity will allow to observe muon conversion events if this process has a probability of the order of 10^{-17}. However, in case no conversion event is observed, Mu2e will set an upper limit to the probability of the process and will improve the current experimental limit from SINDRUM II of four orders of magnitude.

The international Mu2e collaboration is completing the design of the various detector components and will begin to build the experiment in the year 2020. The construction is expected to be completed within the year 2021. The beginning of data taking is planned for the year 2022 and will continue for about three years. Future upgrades of the experimental apparatus planned for the years 2025 and beyond will further improve the experimental Mu2e sensitivity by a factor of 10.

1.2   The Fermilab accelerator complex

Fermilab is located in Batavia, about 50 km west of Chicago, Illinois (USA). It is a US Department of Energy Laboratory, operated by the Universities Research Association (URA) since its founding in 1967 to 2006 [6]. Since 2007 it has been operated by

---

[6]In particle physics, every type of particle has an associated antiparticle with the same mass but with opposite physical charges (such as electric charge).

[7]the positron is the antiparticle of electron

[8]γ is the symbol representing the photon.

Figure 1.2: Aerial view of the Fermilab site. The Mu2e facility is close
to the center. Many other experiments are hosted in the site (TEVA-
TRON etc . . .)

the partnership between the University of Chicago and the University Research As-
sociation, named Fermilab Research Alliance (FRA). The name Fermilab was given
to the laboratory in 1974 to honor the memory of the Italian Nobel prize Enrico Fermi
[7].
Figure 1.2 shows an aerial view of the laboratory, which has played a major role in
the field of high energy physics for the last forty years. Among its scientific achieve-
ments, it is worth mentioning the discovery of three among the four particles of the
model's third generation: the bottom quark (May-June 1977), the top quark (Febru-
ary 1995) and the tau neutrino (July 2000).

1.2.1   The accelerators chain

The accelerator complex is composed of several stages:

- The first stage is a *Cockcroft-Walton generator*, which turns hydrogen gas into
  H^- ions by flowing it into a container lined with molybdenum electrodes (a
  matchbox sized, oval shaped cathode and a surrounding anode, separated by
  1 mm and held in place by glass ceramic insulators). A magnetron[9] is used
  to generate a plasma to form H^- ions close to the metal surface. A 750 keV
  electrostatic field is applied by the Cockcroft-Walton generator, and the ions
  are accelerated out of the container;

- The second stage is a Linear Accelerator (or *Linac*), which accelerates the ions
  to the energy of 400 MeV (approximately 70% of the speed of light). Just before
  entering the next accelerator, the ions pass through a carbon foil, where they
  lose the electrons producing a H^+ ion beam (called proton beam);

---

[9]A high powered vacuum tube that generates microwaves using the interaction of electrons streams
with a magnetic field, while moving past a series of open metal cavities (cavity resonators).

Figure 1.3: Layout of the Mu2e facility (lower right) relative to the accelerator complex that provides the proton beam to the detector. Protons are transported from the Booster through the MI-8 beamline to the Recycler Ring, where they circulate while being rebounded by a 2.5 MHz RF system. The reformatted bunches are kicked into the P1 line and transported to the Delivery Ring, where they are slowly extracted for the Mu2e detectors
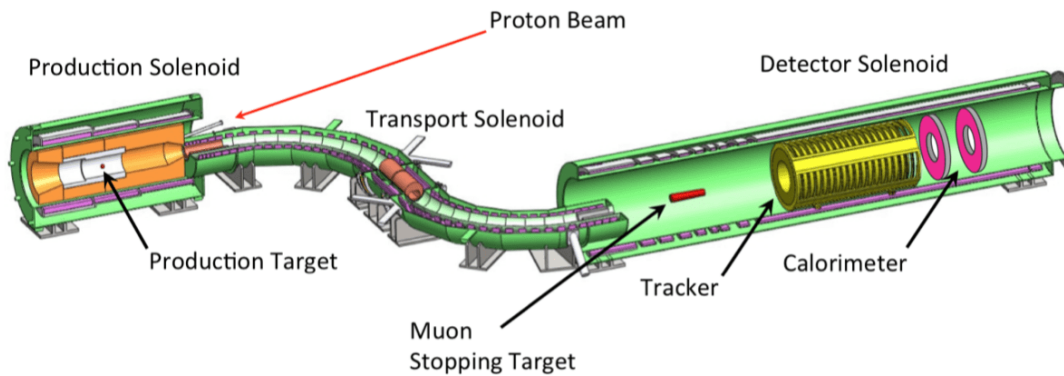
Figure 1.4: Mu2e apparatus: the proton beam enters from the right at the junction between the Production Solenoid and the Transport Solenoid, and strikes the production target. The cosmic ray veto system, which surrounds the Detector Solenoid, and the muon stopping monitor are not shown in this scheme (source: Mu2e experiment data center).

- The third section is the *Booster Ring*. The Booster ring is a 468 m circular accelerator that uses magnets to bend the proton beam in a circular path. The protons coming from the Linac travel around the Booster about 20000 times in 33 ms, in order to multiply the accelerating electric field. Each revolution gives the protons more energy, until the beam leaves the ring at approximately 8 GeV;

- Finally the protons are injected into the *Recycler Ring*, where they circulate while getting rebounded by a 2.5 MHz frequency system. The reformatted bunches are transported to the delivery ring, where they are slowly extracted from the Mu2e detector through a new external beamline (Figure 1.3);

1.3 The Mu2e experimental facility

The Mu2e experimental apparatus is extensively described in the conceptual *Design and Technical Report* [1]. The layout of the muon beam line and the detector system are also shown in Figure 1.4.

1.3.1 Production solenoid

The Mu2e magnet system consists of three large superconducting solenoids. The first component in the chain of magnets is the Production Solenoid (PS), whose role is to collect and focus pions[10] and muons generated in the collision of an 8-GeV proton beam with a tilted high-Z target, by supplying a peak axial field between 4.6 T and 5.0 T and an axial field gradient of about 1 T/m, within a 1.5 m warm bore. The PS is a challenging magnet because of the relatively high intensity magnetic field and the harsh radiation environment that require state-of-the-art conductors in

---

[10]In particle physics, a pion is any of the three subatomic particles: π^+, π^-, π^0 (depending of their net charge). Pions consist of a quark and anti-quark, and are the lightest among the mesons. Charged pions most often decay into muons and muon neutrinos, while neutral pions generally decay into gamma rays.
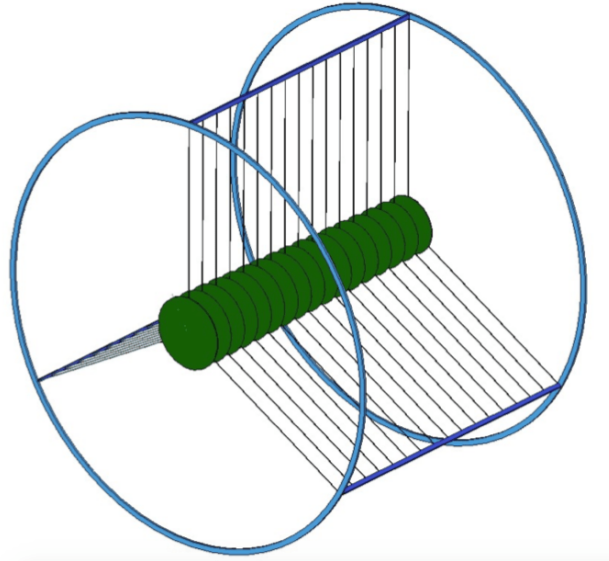
Figure 1.5: The Mu2e stopping target is made of 17 aluminum disks, 0.2 *mm* thick, spaced 5.0 *cm* apart along the Detector Solenoid axis. The disks radii decrease from 8.3 *cm* at the upstream end to 6.53 *cm* at the downstream end (source: Mu2e experiment data center).

terms of the current-carrying capacity and structural strength. The PS coil is protected by a massive Heat and Radiation Shield (HRS).

1.3.2   Transport solenoid

The role of the S-shaped Transport Solenoid (TS) is to filter and transport the muon beam (around 1011 muons per second) to the Detector Solenoid. It is composed of 14 superconducting units (solenoids and toroids) and is divided in five sections:

- a 1 *m* long straight section;

- a 90 degree elbow, with 3 *m* radius of curvature;

- a second 2 *m* long straight section;

- a second 90 degree elbow, similar to the first, that turns the beam line in a direction parallel to the first one;

- a final 1 *m* long straight section.

The resulting length of the Transport Solenoid is 13 *m*. To improve the purity of the muon beam, the Transport Solenoid has an absorber placed in its central part that stops charged particles (mainly antiprotons). A state-of-the-art collimator system is placed in the same zone to select only low energy muons with momentum below 0.08 *GeV/c*. Moreover, the S-shape of the solenoid removes neutral particles, that in absence of an electromagnetic interaction travel in a straight direction.

1.3.3   Detector solenoid

The Detector Solenoid (DS) is 11 *m* long and provides a decreasing magnetic field in the first sector (from 2 *T* to 1 *T*). It hosts the muon stopping target, schematically
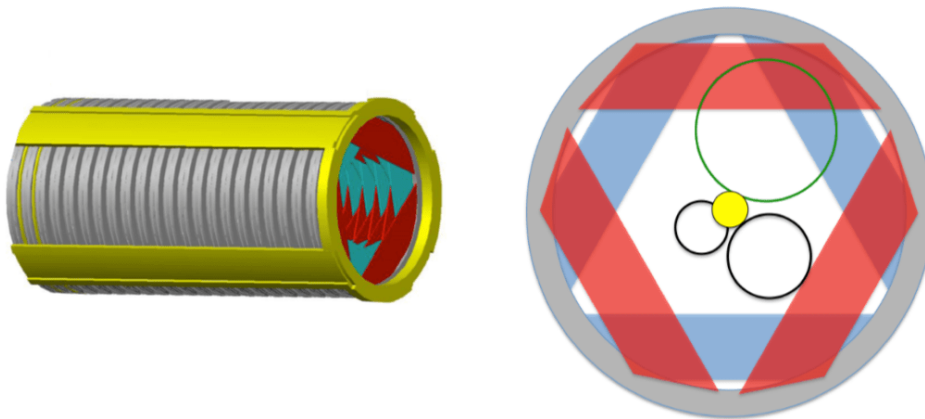
(a) The Mu2e *Tracker*; some of the 18 station of the tracking system are visible on the right.

(b) Cross-sectional wiew of the Mu2e *Tracker*.

Figure 1.6: The Mu2e tracker is composed of 18 tracking system stations. Thanks to the design only electrons with energy above 53 *MeV* are reconstructed. Lower energy electrons pass through the central un-instrumented part of the device and leave no track. This effect is due to the spiral motion of electrical charges in a uniform magnetic field (source: Mu2e experiment data center)

represented in Figure 1.5.

Muons impacting the disks come to rest and replace the electrons lying in the $1s$ orbit of the aluminum atoms. The lifetime of the muon in the muonic atom is 864 ns. The non-uniformity of magnetic field plays an important role in reducing the background coming from high energy electrons transported to the Detector Solenoid. The magnetic field gradient is generated by introducing spacers to change the winding density of the superconducting cable, which is made out of aluminum-stabilized *NiTi*.

The second sector of the Detector Solenoid houses the detectors: the *tracker* and the *calorimeter*, which are described in more detail in section 1.3.4. In this sector the magnetic field is relatively uniform and has the average intensity of 1 *T*.

1.3.4 The tracker and the electromagnetic calorimeter

The Mu2e tracker and electromagnetic calorimeter are placed inside the Detector Solenoid. The Mu2e collaboration decided to use a tracker design similar to the one developed by the MECO collaboration (Figure 1.6) [8].

The tracker resides in a uniform 1 *T* solenoidal magnetic field and in the environmental pressure of approximately $1.33 \cdot 10^{-2}$ *Pa* to reduce multiple scattering[11] to a negligible level. It reconstructs particle trajectories with high efficiency and measures the parameters of the helical trajectories with extreme accuracy.

Given that multiple scattering in the tracker dominates the resolution on the measurement of the helix parameters, the mechanical structure of the detector has been made extremely light. The tracker is made of *straw drift* tubes; and is called T-tracker

---

[11]Scattering produced with lower energy level particles

because the straws are transverse to the axis of the Detector Solenoid. The basic detector element is made of a 20 *μm* sense wire inside a straw tube filled with gas. The straws are 5 *mm* diameter tubes, made of 15 *μm* thick metallic Mylar. The tracker is made of approximately 2000 straws arranged along 18 stations across the 3 *m* tracker length. One tracker plane consists of two layers of straws to improve the reconstruction efficiency and help to overcome the classic left-right ambiguity. A 1 *mm* gap between straws allows for manufacturing tolerance and expansion due to the internal pressure. A larger radius ring outside the active detector region supports the straws and the electronics boards. Each straw has one preamplifier and one time-to-digital converter (TDC) placed on each tip to measure the signal arrival time on both sides. It also uses analog to digital converters (ADC) to measure the total integrated charge, providing useful information for particle identification. The tracker has been designed to observe only electrons with energy greater than 53 *MeV*. Electrons below this threshold travel undetected in the central un-instrumented volume of the tracker. They are approximately the 3% of the total electron flux coming from muon decays. Since momentum resolution is a crucial factor to suppress critical backgrounds, the tracker is required to have a momentum resolution better than 180 *keV* for 100 *MeV* electrons.

The Mu2e calorimeter provides additional energy, position, and timing information to improve particle trajectory reconstruction performed by the tracker. The two detectors use complementary physical and technological processes to perform their measurements, to rely on uncorrelated error sources. This helps to reduce backgrounds and provides a cross check to verify the quality of signal events. The calorimeter operates in the same solenoidal magnetic field and vacuum level of the tracker. It handles a large flux of particles, mostly a low energy background of protons, neutrons and gamma rays produced by muon captures in the stopping target. It also handles the large flux of electrons coming from muons decays in the aluminum stopping target, and other produced particles during the beam injection. A more detailed description of the calorimeter is reported in chapter 2.

1.3.5   Cosmic ray veto

Cosmic ray muons can initiate background processes and generate particles that interact with the detectors and produce undesired noise. Simulation shows that approximately one background event generated by cosmic ray muons may be erroneously reconstructed as a conversion electron signal per day. This source of background should and can be reduced to a negligible level introducing passive and active shielding.

The *Cosmic Ray Veto* (CRV) surrounds the entire volume occupied by the Detector Solenoid and the downstream part of the Transport Solenoid. It consists of four layers of extruded scintillator strips with silicon photosensors and aluminum absorbers. The cosmic-ray induced background rate will be monitored between beam spills and when the beam is turned off. This allows to perform a direct measurement of the background levels. The study of the background rate will be initiated as soon as the Detector Solenoid and the cosmic ray veto are in place.

1.3.6   Trigger and data acquisition system

The Trigger and Data Acquisition (TDAQ) systems provide hardware and software tools to record the digitized data read from the detectors. The TDAQ synchronizes

and controls the data-streams received from the detectors. We have estimated that the online detector bandwidth requirement for the DAQ is around 100 GB/s in streaming mode.

The TDAQ also combines information from all the detector data sources and applies filters (triggers) to reduce this rate by a factor of several thousands before the data get delivered to the offline permanent storage. Essentially, this is obtained by applying standard cross checks to validate the consistency of data coming from the detectors and performing an event reconstruction as accurate as possible within the timing constraints.

Chapter 2

The Electromagnetic Calorimeter

The Mu2e electromagnetic calorimeter has been designed to complement the straw tracker and the cosmic ray veto in rejecting backgrounds to reach the required sensitivity for the muon conversion processes. The calorimeter has been designed to perform several complementary functions which include measuring particles energy, timing and position, aiding track reconstruction performed by the straw tracker, strengthening particle identification and the capability to reject muons and antiprotons interactions mimicking the conversion electron signal. Moreover, the calorimeter provides a fast signal that can used as standalone trigger primitive [9]. In order to perform these numerous and complex functions, while operating in the "harsh" Mu2e environment, in terms of radiation levels, vacuum and magnetic field intensity, the design of the calorimeter has required several years of work to optimize the geometry, the architecture, the choice of materials and the assembly procedure.

2.1 Physical requirements

The Mu2e Collaboration has performed an extensive simulation campaign to determine the necessary calorimeter performance: [1].

- energy resolution better than $\sigma_E/E = \mathcal{O}(10\%)$ (at 105 MeV), to distinguish it from the ≈ 40 MeV energy deposit from 105 MeV/c muons mimicking the signal;

- timing resolution better than ≈ 0.5 ns (at 105 MeV), to ensure that the energy deposits in the calorimeter are in coincidence with the arrival of the conversion electrons;

- position resolution ($\sigma_{r,z}$) better than 1 cm, to match the position of the energy deposits with the extrapolated trajectories of the reconstructed tracks;

- be able to keep an efficient operation in the high-radiation Mu2e environment and maintain its functionality while exposed to radiation levels up to ≈ 15 krad/year in the hottest region and to a neutron flux equivalent to $10^{12} MeV/cm^2/year$, inside an evacuated region (10^{-4} Torr) of the Detector Solenoid that provides 1 T axial magnetic field. The radiation limits include specific safety factors related to Monte Carlo evaluation ($\times 3$), lot of production ($\times 2$) or rate value ($\times 2$) in case of electronics.

- fast response to handle the experimental high rate ($\tau < 40ns$);

- temperature and gain stability within + 0.5%, to preserve the energy resolution;
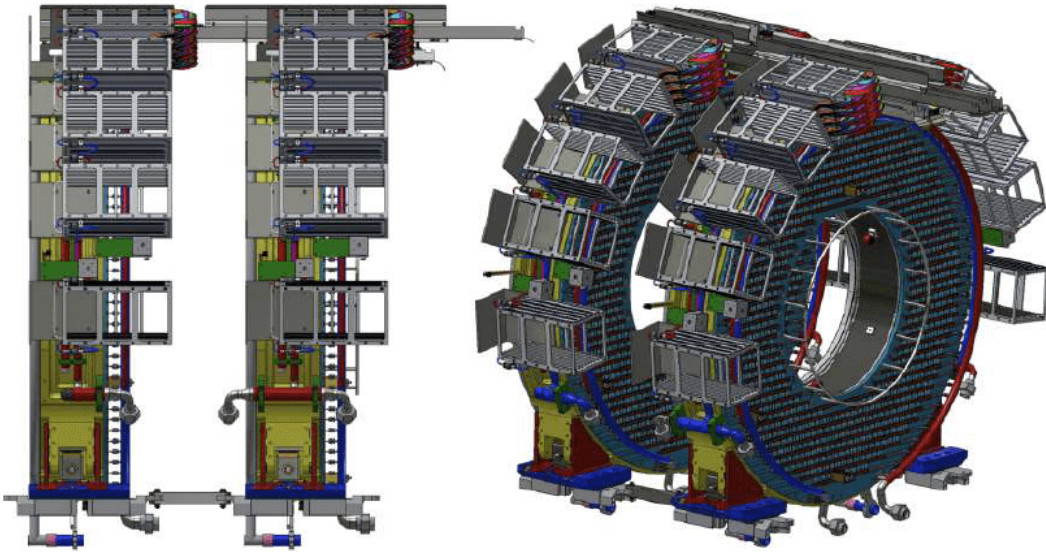
Figure 2.1: Side (left) and angular (right) CAD view of the two disk
of the calorimeter.

- reliability and redundancy to operate in vacuum for one year without any interruptions.

2.2 Calorimeter design

After a long R&D activity, in 2015 the Mu2e Collaboration released the final calorimeter Technical Design Report and the detector design was chosen [10] [11]. The Mu2e calorimeter design is based on two disks with dimensions optimized to maximize the acceptance for conversion electrons. Figure 2.1 shows the design of the calorimeter: two annular disks with an inner diameter of 700 mm and an outer diameter of 1320 mm posed at the distance of 700 mm along the beam-line, which corresponds to approximately half pitch of the helical conversion electron trajectory. Each disk is composed of 674 Cesium Iodide (CsI) square base scintillating crystals of $34 \times 34 \times 200 mm^3$ wrapped with a 150 μ foil of Tyvek. The scintillating light is readout with two SiPMs per crystal to improve reliability. The SiPM are directly connected to the Front-End Electronics (FEE) boards are mounted on the rear side of each disk, while the boards which provide voltage distribution, slow control and perform SiPM signal digitization are hosted in crates positioned on the external lateral surface of each disk. Each FEE/SiPMs/crystal system has its own independent power and readout channels. Digitization electronics provide a sampling at 5 ns to allow a high-resolution timing reconstruction and pileup separation. A laser flasher system provides light to each crystal for relative calibration and monitoring purposes. A distributed pipes system, mounted on the front side (facing the beam) of each disk, with a radioactive liquid source circulating inside, provides and absolute and a channel-by-channel energy scale calibration.

2.2.1 CsI Crystals

Crystals of different materials have been considered by the Mu2e Collaboration:

Property	BaF_2	LYSO	CsI	$PbWO_4$
Density $[g/cm^3]$	4.89	7.28	4.51	8.28
Radiation length $X_0[cm]$	2.03	1.14	1.86	0.9
Molière radius $[cm]$	3.10	2.07	3.57	2.0
Interaction length $[cm]$	30.7	20.9	39.3	20.7
$dE/dx[MeV/cm]$	6.5	10.0	5.56	13.0
Refractive index at λ_{max}	1.50	1.82	1.95	2.20
Peak luminescence $[nm]$	220,300	402	310	420
Decay time $\tau[ns]$	0.9, 650	40	26	30, 10
Light yield (compared to NaI(Tl)$[\%]$	4.1, 36	85	3.6	0.3, 0.1
Hygroscopicity	None	None	Slightly	None

Table 2.1: Comparison of crystal properties for LYSO, BaF_2, pure CsI and $PbWO_4$.

- Lutetium-Yttrium OxyorthoSilicate (LYSO) [12];

- Lead Tungstate ($PbWO_4$);

- Barium Fluoride (BaF_2) [13];

- pure undoped Cesium Iodide (CsI)

Table 2.1 reports the main physical properties of crystals that have been taken into account to build the calorimeter. In the Mu2e Conceptual Design Report [14] of 2012, the calorimeter baseline design was based on LYSO crystals. Since that date, an extensive R&D program was carried out to study this option [15][16]. Unfortunately, the cost of a LYSO calorimeter resulted too expensive and not affordable, due to the exponential increase in the lutetium price. The option of $PbWO_4$ was excluded for its low light yield. The last two materials, BaF_2 and CsI crystals, were then considered, because they have very similar properties in terms of light output and radiation length. BaF_2 has a fast scintillation light component (0.9 ns) at the wavelength of 218 nm, but has also an important slow component above 280 nm with a decay time of $\approx$650 ns. Therefore, BaF_2 needs to be coupled with a photosensor which can suppress the slow component being, as normally called, "solar blind".
Since the R&D campaign necessary to develop the necessary "solar-blind" photosensor in this wavelength region turned out to be aggressive, this option was considered too risky and was abandoned. Because of their properties and for a good matching with new generation photo-sensors, CsI crystals were considered a good compromise. For these reasons, CsI was selected as the final scintillator choice [16][17] after the construction and test of a reduced-scale prototype named "Module 0". The chosen length of the crystals (200 mm) corresponds to approximately 10 radiation lengths (X_0), however when considering the average conversion electron incidence angle (50°) on the crystal surface, the effective crystal length becomes $\approx$300 mm that corresponds to an acceptable shower containment of 15 X_0. Pure CsI has an emission spectrum [18] characterized by a fast emission peak at the wavelength of approximately 315 nm, with a decay time of about 30 ns, and a very small fraction of a slow emission with a decay time of $\approx 1\mu$s due to residual impurities in the crystal growth. Each crystal is wrapped to Tyvek sheet to reflect approximately 90% of the scintillation light, and Tedlar sheets are added between consecutive crystals to eliminate
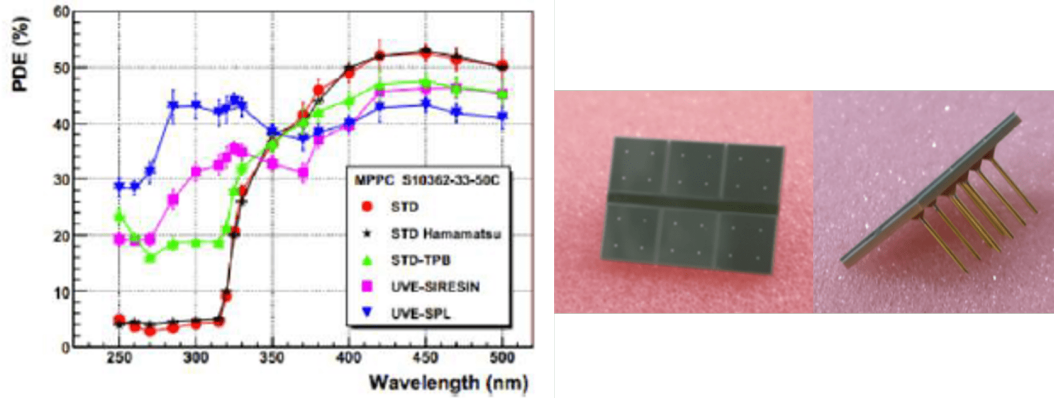
Figure 2.2: Left: PDE measured as a function of the wavelength for four SiPM prototypes. The typical PDE values of the standard SiPM S10362-33-50C from Hamamatsu are shown for comparison. These measurements were performed at 25°C and include effects of cross-talk and after-pulses. Right: photograph of the SiPM selected by the Mu2e Collaboration.

residual cross-talk effects. To minimize the thermal coupling and to avoid the use of glue or other materials that could generate outgassing in vacuum or deteriorate with radiation, an air gap of 2 mm has been left between the crystal face and the photosensors. Moreover, this approach allows to easily replace a failing sensor readout unit.

2.2.2   Photosensors

The Mu2e calorimeter photosensors operate in a 1 T magnetic field, which drove the choice of the solid-state photodetector such as Silicon PhotoMultipliers (SiPMs). To ensure an optimal coupling with the CsI scintillation emission spectrum, the photosensor should provide a good quantum efficiency at the wavelength of 310 nm. The calorimeter will be accessible for maintenance only once a year, so the photosensors must have a good reliability and avoid any deterioration of the expected calorimeter performance. Redundancy is a good mean to increase reliability, so each crystal is equipped with two photosensors with independent readout, for a total of 2696 SiPM and electronics channels. SiPMs are photon-counting devices made by one planar matrix of several avalanche photodiode (APD) pixels of the same shape, dimensions and construction features that are operating in Geiger mode. The SiPM operates at inverse polarization above the breakdown voltage and its pixel is coupled to a quenching resistor [19]. For the Mu2e calorimeter a custom SiPM has been designed consisting of a large area 2 x 3 array of individual UV-extended 6 x 6 mm^2 SiPM cells. Each cell is composed by 14400 pixels of 50 x 50 μm^2 dimensions. The device Photon Detection Efficiency (PDE) depends on its energy (or wavelength), as shown in Figure 2.2 (left). The PDE is the product of three main factors:

$$PDE(\lambda, V_{br}) = QE(\lambda) \times \epsilon_{av}(V_{br}) \times F \qquad (2.1)$$

where $QE(\lambda)$ is the quantum efficiency at a given wavelength λ, $\epsilon_{av}(V_{br})$ is the efficiency to trigger an avalanche process in the depletion region produced at the breakdown voltage V_{br} and F (Filling factor) is the ratio between the sensor sensitive
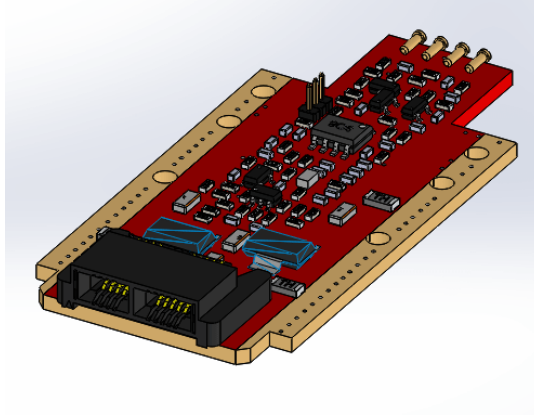
Figure 2.3: CAD drawing of the AMP-HV integrated circuit.

area and its overall transverse dimension. The chosen photosensor for the Mu2e calorimeter is a TSV-SPL SiPM from Hamamatsu [20]. SPL stands for Silicon Protection Layer, meaning an optical layer different from the standard epoxy used for the detection of blue wavelengths. The blue markers in Figure 2.2 show its PDE compared to similar devices [21]. In the UV range, 250-350 nm, the PDE of this UV-enhanced SiPM is of $\mathcal{O}(30\%)$, which is a factor $\approx$6 times better than a standard Hamamatsu SiPM. These devices operate at low voltage while featuring a very high gain, a high PDE, a high-speed of response, an excellent time resolution and a wide spectral response range. Over the breakdown voltage, the SiPM gain is linearly related to its inverse polarization voltage as follows:

$$G = \frac{Q}{e} = \frac{(V_{bias} - V_{br}) \cdot C_{pixel}}{e} \tag{2.2}$$

where V_{bias} is the voltage applied to the SiPM and C_{pixel} is the capacitance of a single pixel. The analog sum of the output of each pixel forms the SiPM output. Assuming all pixels are identical and produce the same amount of charge, the number of impinging photons is directly proportional to the charge output. When a SiPM is hit by one photon, there is a dead time (also called recovery or quenching time), due to the presence of the quenching circuit. The digital nature of the device appears when a large flux of incident photons arrives on the SiPM area, since the number of fired pixels will saturate following the relation:

$$N = N_{max}(1 - e^{-\frac{\mu}{N_{max}}}) \tag{2.3}$$

where N is the number of active pixels, N_{max} is the total number of SiPM pixels and $\mu = N_\lambda \cdot PDE$ is the number of incident photons re-scaled with the PDE. In order to get a linear response on the calorimeter is mandatory to select the N_{max} in a way that the sensors operate in a region of photon flux much less than N_{max}. A basic rule is to keep it below the 5%. All the calorimeter SiPM will be carefully inspected and characterized to validate their performances [22].

2.2.3 Front End Electronics

The Front-End Electronics (FEE) consists of two discrete and independent boards (Amp-HV) for each crystal that are directly connected to the back of the photosensor
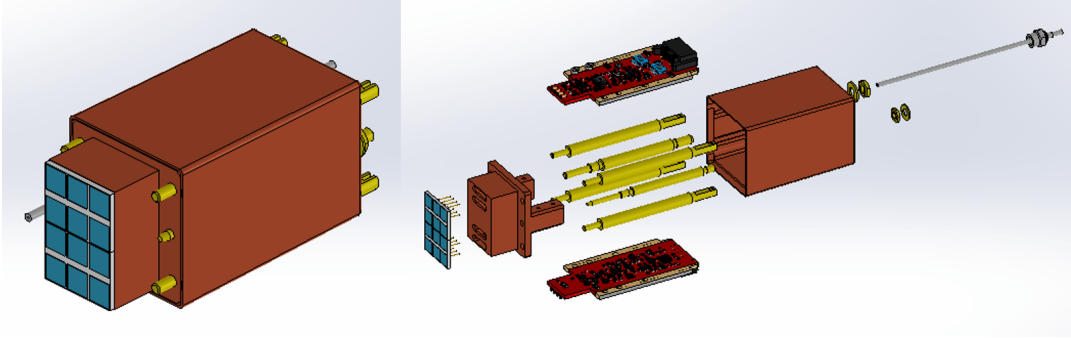
Figure 2.4: Left: assembly of the FEE holder. Right: exploded view
of the FEE holder with all the components. Two SiPMs glued on the
inner copper support, FEE AMP-HV boards, Faraday cage, screws
and optical fiber needle.

pins. These provide both the amplification and shaping stage, and a local linear regulation of the photosensor bias voltage (Figure 2.3). The FEE board also implements the readout of current and temperature sensors, whose values are then transferred to the Detector Control System. The Amp-HV board requirements are the following:

- two settable amplification values: 1 or 2, with a transimpedance low noise amplifier;

- a signal rise time larger than 25 ns (5 times the digitizer sampling time) in order to allow at least five points to determine with precision the signal leading edge and therefore grant a good time resolution;

- a short falling time to improve pileup rejection;

- a high precision and stability in regulating and keeping the operation voltage of the photosensors ($V_{op} < 20mV$);

- sustain a rate of 1 MHz/channel, while maintaining a stable gain, signal shape and the pileup rejection capability;

- a stable output regardless the increase of the average current due to irradiation of the photosensors or the radiation induced noise in the crystals, assuming those contributions to be contained below 2 mA;

- a low power consumption

A pair of Amp-HV chips and one pair of photosensors are arranged in a modular unit called SiPM-holder, as shown in Figure 2.4. The holder is composed of a copper support on which the two SiPMs of each crystal are glued. The support holds also the two FEE electronic boards in thermal contact by means of bridge resistors. The FEE boards are shielded by a surrounding copper Faraday cage. The last component of the holders is the optical fiber needle that transports the light from the laser calibration system to the crystal surface, illuminating by diffusion in the Tyvek the photosensors. Each group of 20 Amp-HV boards are controlled by a dedicated Mezzanine Board (MB), where an ARM controller supervises the distribution of the low and high voltages reference values, while setting and reading back the locally regulated voltages. From each MB, sets of 20 signals are sent in differential way to the
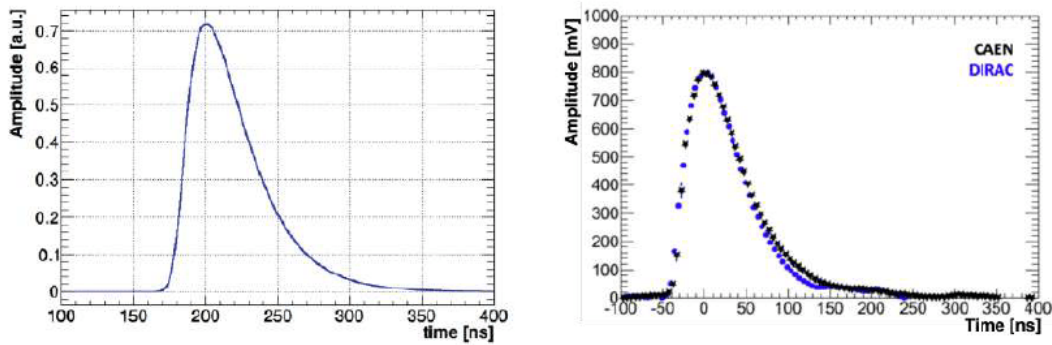
Figure 2.5: Left: Monte Carlo simulation of the CsI + SiPM + FEE waveform. Right: Cosmic event digitized with the DIRAC board (blue dot) and with a commercial digitizer (black star).

waveform digitizer (DIRAC) board (subsection 2.2.5). The parameters read out/set by the MB pass to the DIRAC boards, which then communicate with the TDAQ and the Detector Control System through an optical link. Both disks are subdivided into 34 similar pie-shaped slice sectors, each one grouping 20 crystals.

2.2.4 Trigger Data Acquisition System (TDAQ)

The calorimeter has a total of 2696 fast analog signals to be digitized after being amplified and shaped by the FEE. On average, pulses of 150 ns maximum width with a rise time of > 25 ns are expected as input to the digitization state with a dynamic range of 2 V. The simulated shape of signals is shown in Figure 2.5 (left); this width and shape are the results of convolution between the CsI emission time, the SiPM quenching time and the FEE amplification and shaping parameters. A comparison of the experimental signal obtained with a cosmic event acquired with the DIRAC board and a digitizer from CAEN is reported in Figure 2.5 (right). The two waveforms present a similar amplitude.

The digitizing system contains 140 DIRAC boards arranged in 10 crates per disk. Each DIRAC board is cooled through a copper cold plate that is kept in thermal contact with the highest dissipation components. The cold plate is thermally connected to the crate custom aluminum structure through dedicated cardlocks. Simulations and study of the beam test data were used to optimize the digitization frequency and the bit resolution required to satisfy the Mu2e requirements: 200 Msps and 12 bits of resolution are a good compromise between performance, power dissipation, costs and overall data through-put.

2.2.5 The DIRAC digitizing unit

The DIRAC (Figure 2.6) has to digitize and serialize analog data and send them upstream to the TDAQ system through a transceiver optical fiber. This board must also perform the zero suppression (i.e., remove signals below threshold) and provide the calculation of the baseline, mean charge and timing for each channel by means of running averages. Each board will handle 20 channels. After a long irradiation campaign, the basic components of the board have been selected to stand a Total Ionizing Dose (TID) 3 krad (DC-DC converters, ADCs jitter cleaner, Double Rata Rate memories). For the FPGA, a new radiation hard version has been chosen to be
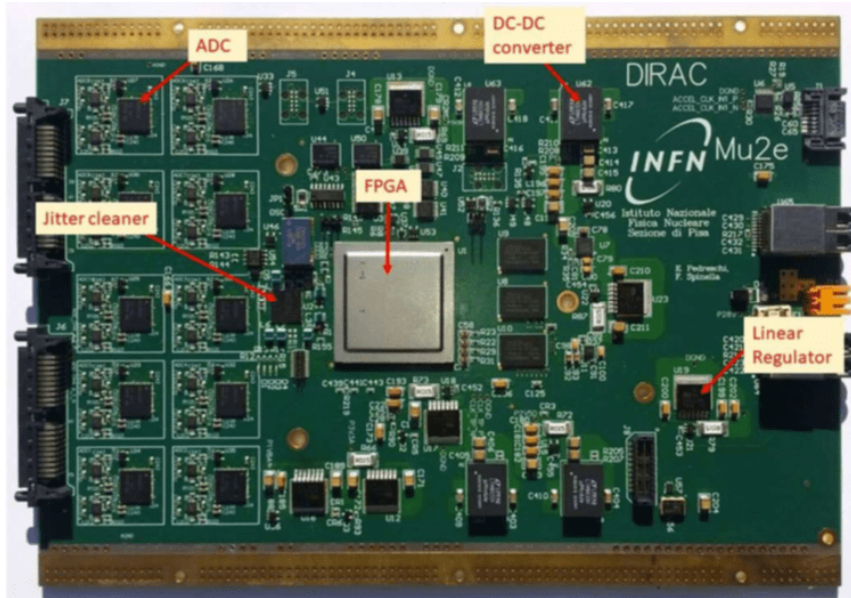
Figure 2.6: Left: Monte Carlo simulation of the CsI + SiPM + FEE waveform. Right: Cosmic event digitized with the DIRAC board (blue dot) and with a commercial digitizer (black star).

consistent with the tracker choice and use the same firmware. The design is based on a FPGA belonging to the Microsemi Smartfusion 2 family, model POLARFIRE. A very accurate jitter cleaner (LMK04828) will reduce the incoming clock jitter to less than 100 ps and distribute it to the ADCs and to the FPGA. Signals will be sampled by 10 double-channels high-speed ADCs (ADS4229) and the FPGA will perform the online operation on data and the transmission to the servers [23].

2.2.6   The Laser calibration system

A laser monitor system is used to control the photosensors gains, charge and timing resolutions, as well as to perform a fast equalization of time offsets. A green light laser has been chosen since its wavelengths is in a region far away from the CsI emission peak (310 nm) and the transmittance changes due to irradiation are expected to be small. The overall system is depicted in Figure 2.7. A pulsed laser sends light through standard collimation optics to an optical splitting system to divide the beam into 8 equal sub-beams. By means of eight 1 mm diameter, 60 m long quartz fibers, the light is brought inside the DS. On each disk, there are four integrating spheres with one input for the incoming fiber, two outputs for the secondary fiber bundles and one output for a monitoring photodiode. Each bundle is composed of 110 silica fibers with 200 μm diameter and Fluorine-Doped Silica cladding, for a total of 880 fibers/disk. The end of each optical fiber is inserted in a dedicated custom needle so to arrive up to the readout side of the detector, where is inserted in the FEE/SiPM holders. In this way, the light arriving from the fibers illuminates the crystal and is readout by the photosensors. A laser pulse corresponding to an energy deposition of 50 MeV is sent at each spill-off period, i.e., once 1.4 s. The laser system is expected to provide a 0.5% equalization of all channels in 25 minutes. While the primary distribution system is placed in the DAQ room, and so far away from the detector, the secondary distribution is mounted directly on the calorimeter
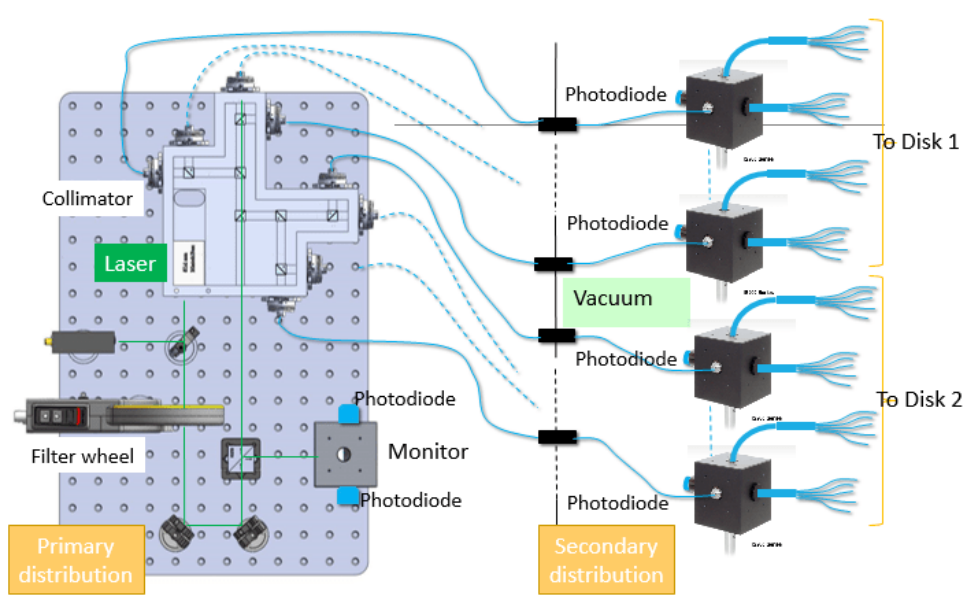
Figure 2.7: Picture of the primary and secondary laser distribution system built in Fermilab.

disks. They are placed between the crates, and they use the same refrigerating system to thermal stabilization, by means of copper bands in contact with crate pipes. On top of each sphere two custom FEE boards are mounted with a photodiode each, to monitor laser pulses directly on the sphere level (Figure 2.8).
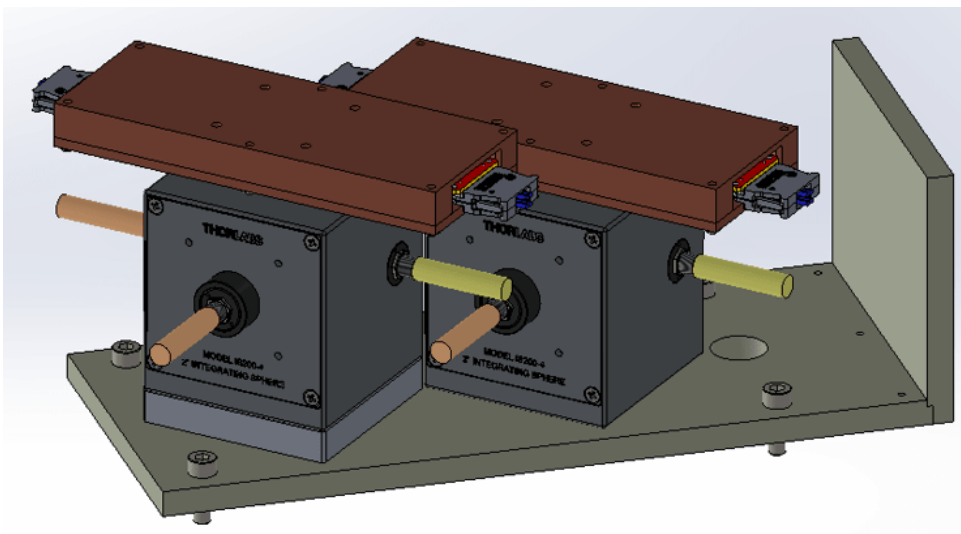Some more details are shown in Appendix 7.3.

Figure 2.8: Cad Module of the laser secondary distribution system.

Chapter 3

The Calorimeter mechanical structures

The calorimeter mechanical structures have been designed to support the crystals matrix obtained by piling them in a self-standing array organized in consecutive staggered rows. The active area of the calorimeter consists of two annular disks of 674 staggered crystals. As anticipated, the crystals have a square parallelepiped shape and are wrapped with 150 μm thickness reflective Tyvek sheets. The total weight of each crystal matrix is $\approx$700 Kg. Figure 3.1 shows an exploded view of all the most important elements composing each disk. Each crystals array is supported by two coaxial cylinders. The inner cylinder (IC) must be as thin and light as possible in order to minimize the passive material in the region where spiraling background electrons are concentrated, and at the same time create a stiff and precise support for the crystals placed above. The outer cylinder is as robust as required to support the load of the crystals. Each disk has two cover plates. The plate facing the beam is made of a sandwich of carbon fiber and an aluminum honeycomb structure to minimize the degradation of the electron energy, while the back plate can be also very robust since it is needed to support the SiPMs, the FEE and the SiPM cooling lines and very low thermally conductive, to avoid cooling down the whole calorimeter structure. The crystal arrangement is self-supporting, with the load carried primarily by the outer ring. The back plane will be built of plastic material with good outgassing properties, like PEEK. It provides support for the FEE electronics and SiPM holders and hosts the cooling pipes to dissipate the power of the electronics and cool down the sensors. The back plate will provide visual access to each crystal. The Front Plate will embed the piping for running the source calibration fluid.

3.1 Envelope and integration

The detector design must fulfil the requirement that the calorimeter has to be integrated in the Detector Solenoid within the available designated volume and all the interferences with other detectors and components. Figure 3.2 shows the longitudinal space available for the calorimeter (top) and its actual occupancy in the current design (bottom). The calorimeter is 1245 mm long. Figure 3.3 shows the transverse occupancy of the calorimeter. Particular care has been put in trying not to fill the transverse area and leave empty volumes to facilitate the evacuation of the area. In the transverse plane a dedicated area for the routing of the straw tracker cabling and cooling pipes has been reserved.
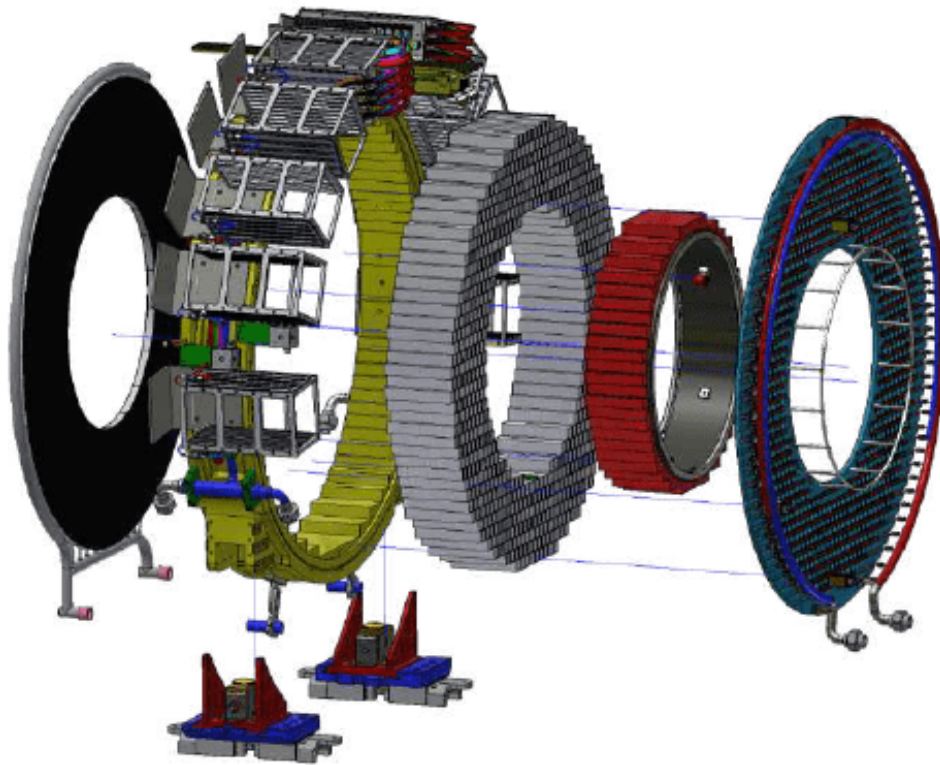
Figure 3.1: Exploded view of the components of the Mu2e calorimeter annular disk.

3.2   Description of the components

The calorimeter is made of two identical disks composed of a number of main parts, listed and described briefly in the following:

- two support feet for transverse adjustment;

- an outer aluminum ring, with integrated steps for crystal supporting;

- an inner carbon fiber ring for crystal supporting;

- a PEEK back plate housing SiPMs and FEE electronics and an embedded cooling system;

- a carbon fiber front plate with the integrated source calibration system;

- a matrix of 674 un-doped CsI crystals (see chapter 4);

- 674 SiPM holder with 2 SiPM each (see subsection 2.2.3);

- 10 crates with a partially embedded cooling system housing 9 Dirac digitizing and Mezzanine boards each, reading 20 channel each;

- a laser distribution system (see subsection 2.2.6).

Some other relatively minor subsystems complete the calorimeter, such as the cabling system, the alignment system, the inner ring heating system and the electronic distribution system.
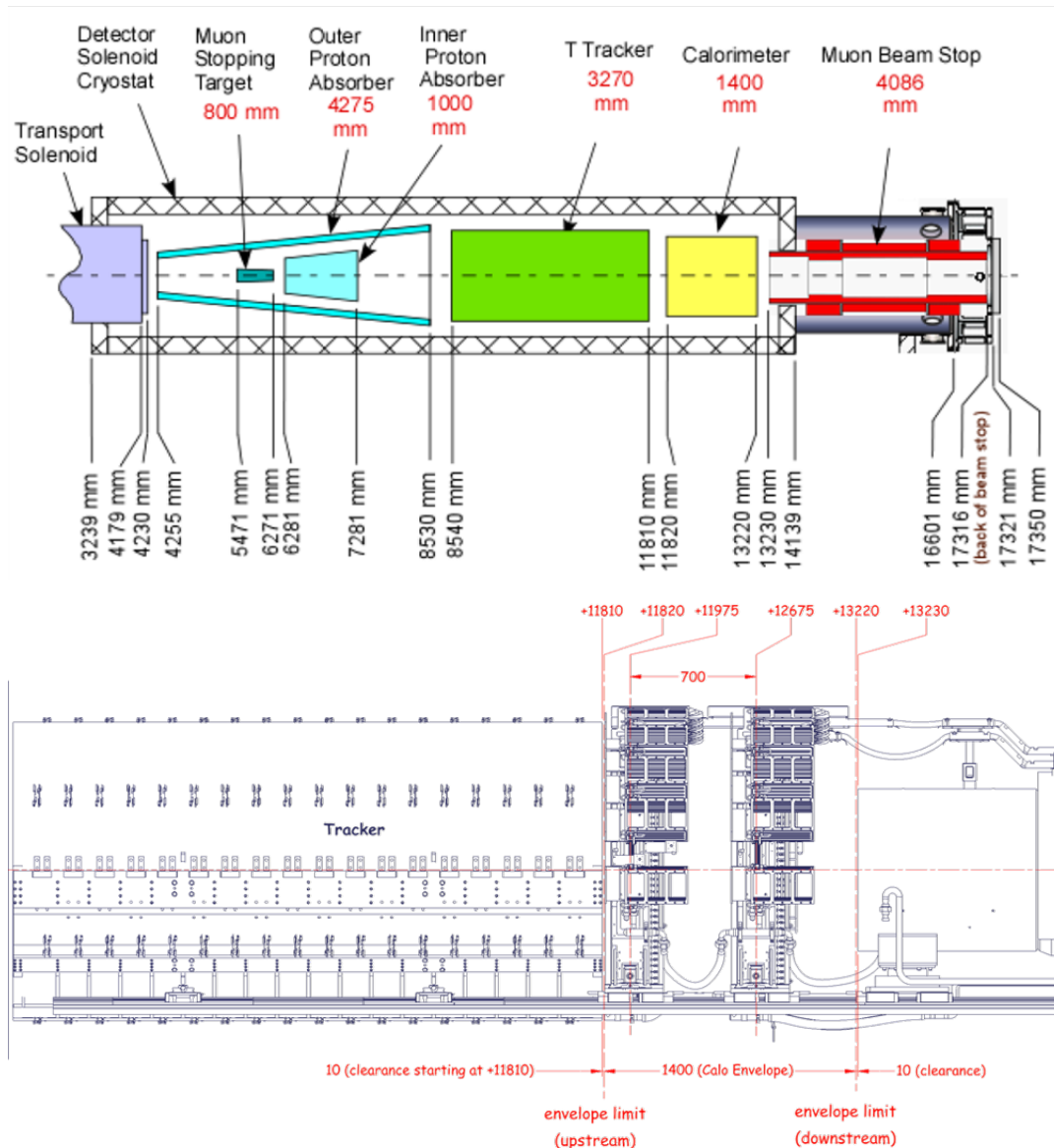
Figure 3.2: Longitudinal space of the calorimeter inside DS: (top) all DS area, (bottom) zoomed around the calorimeter region.

3.2.1 Feet

The calorimeter, the target, the tracker, the muon beam-stop and the closing flange will be connected together to make sure that their relative distances will be precise and fixed. They will move on a rail that will be inside the DS and will be extended outside for the mounting and dismounting procedures. To make this movement smooth without losing any precision, feet (Figure 3.4) are provided with a couple of ceramic linear bearing blocks each, sized properly to hold the whole calorimeter weight.

Another task the feet must fulfill is to adjust the transversal position of the calorimeter. For this reason, an x-y adjusting mechanism is placed in each foot, and will allow to move the calorimeter orthogonality with respect to the beam axis. This alignment will be performed once for all at the beginning of the experiment, and will require
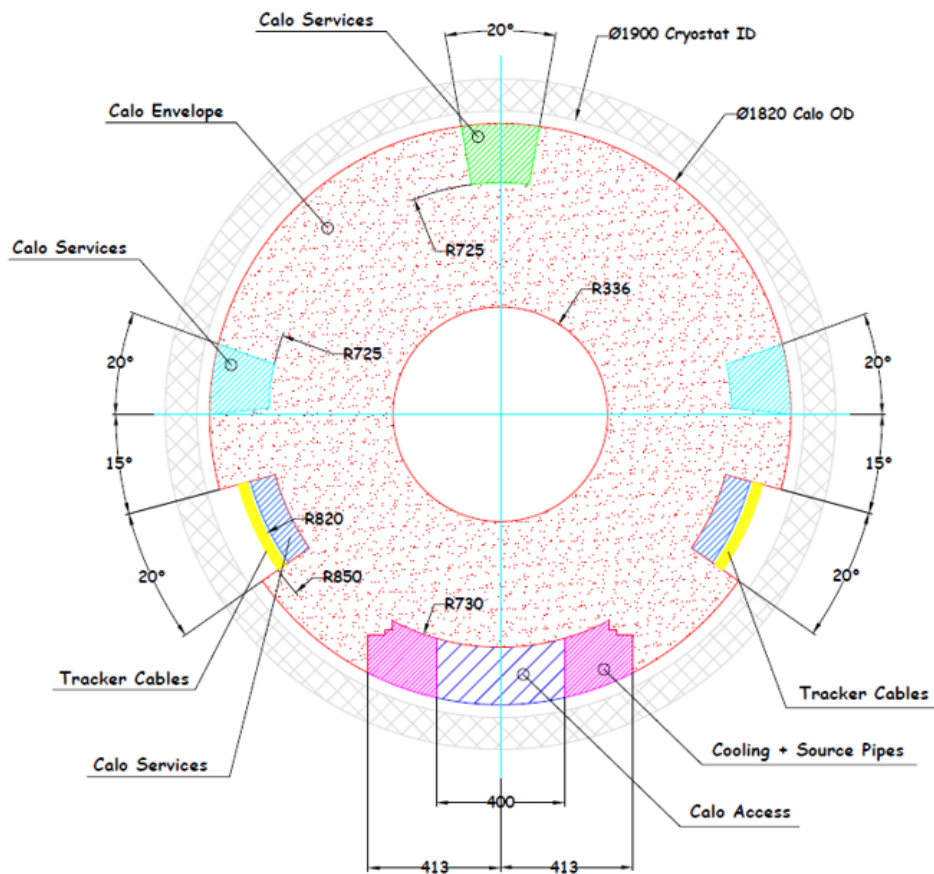
Figure 3.3: Transverse view of the calorimeter with all the service
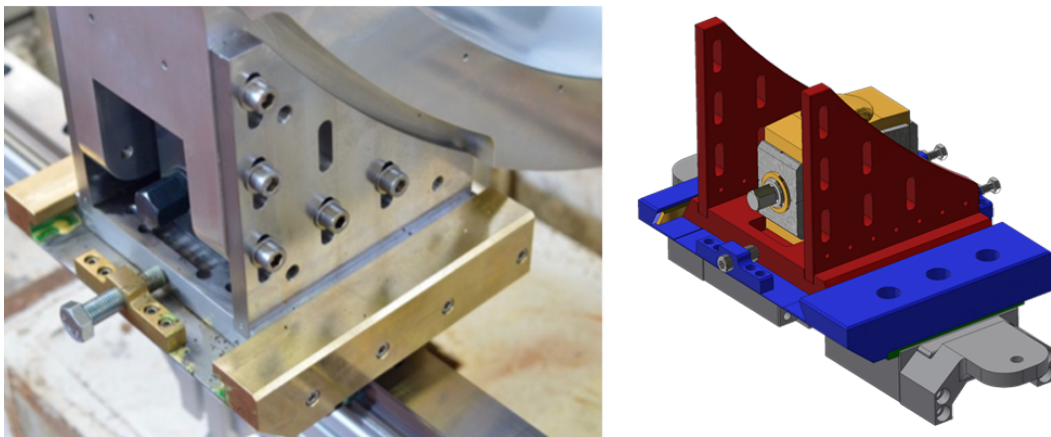areas constraints.

Figure 3.4: Prototype of a calorimeter foot (left). CAD model of the
calorimeter foot (right).

very long time, because the detector train will be pushed in and out several time to
perform a fine adjustment.

The feet are made of not ferromagnetic stainless steel and will be fastened with the
calorimeter aluminum ring through two flanges and several bolts. For the installa-
tion, feet will be placed in advance on the rails, and the calorimeter will be lay down
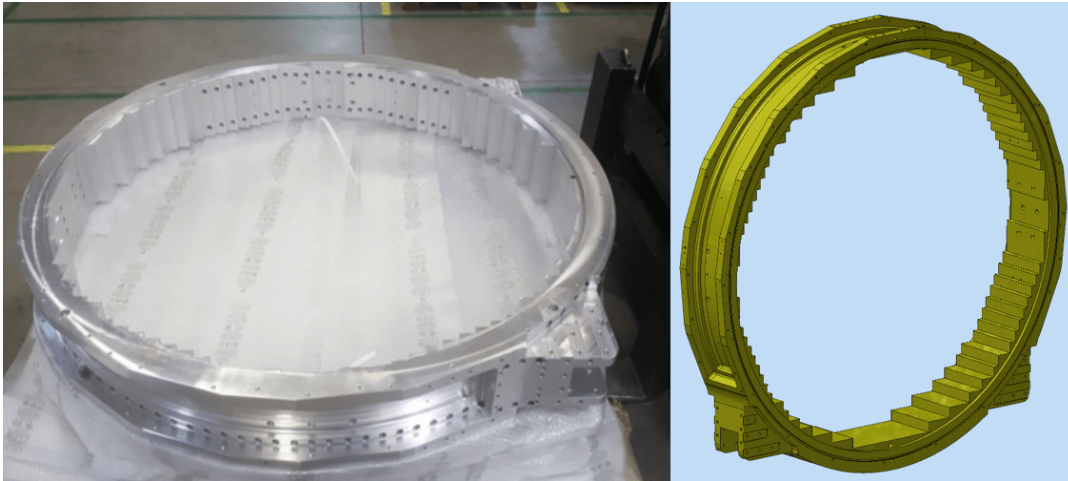
Figure 3.5: One of the two realized aluminum outer ring, just before being shipped at Fermilab (left). CAD model of the aluminum outer ring (right).

on them with a crane, and fasten to them. Once the entire detector train will have been positioned on the rail, feet will be equipped with precise rods to position the two disks at the exact relative distance, and space the calorimeter with the tracker and the MBS.

3.2.2 Aluminum ring

The aluminum ring (Figure 3.5) is the component that must house all the crystals inside, and it cannot allow excessive deformation. As its name suggests, it is an aluminum ring, milled from a bulk block of Al6082 for maximize its stiffness, with all the required steps to host the crystals. It has an outer diameter of 1460mm and a thickness of 146mm. According to the performed FEM analysis, its maximum deformation is 40 μm.

The outer ring will also furnish all the fastening features for the other components, it will house the manifold for the crate cooling system, it will support the surrounding crates, all around it, and it will be used to transport the calorimeter from the Sidet laboratory (where the assembly will take place), to the experimental site, thanks to an outer steel frame it will be connected with.

At the moment of writing this Thesis (March 2021), the aluminum rings have been manufactured, and measured for QC. One of the two rings has been shipped Fermilab, ready for the assembly, and the other one is at LNF to test the assembly procedure of the other components.

3.2.3 Inner Cylinder

The Inner Cylinder is one of the most delicate components of the entire calorimeter. It is indeed, one of the structural components, together with the Front Plate, which the amount of employed material has been carefully optimized. Indeed, all the other structural components are out of the particles trajectory and for this reason the only constraint which limits their stiffness is their volume. The function of the Inner Cylinder is to support all the uppermost crystals and to create stiff surfaces for the crystal positioning.
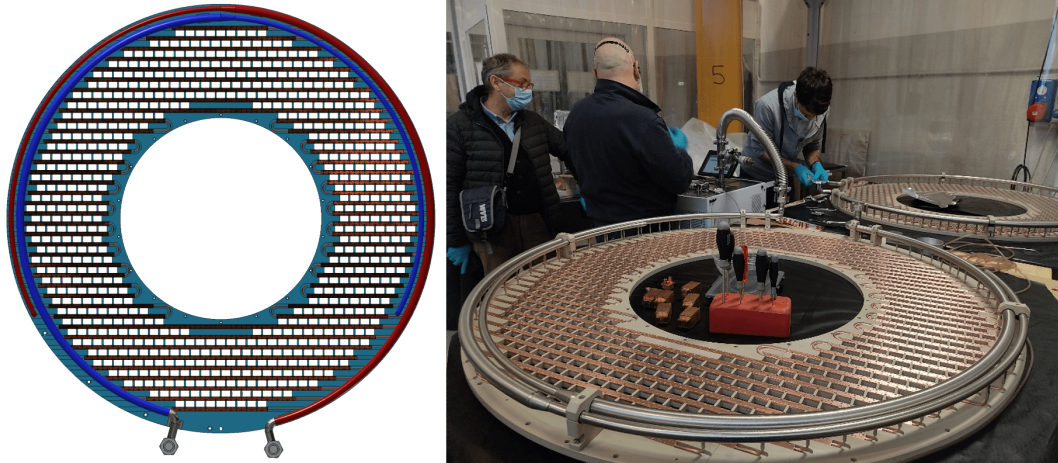
Figure 3.6: CAD view of the 38 pipes network on one calorimeter disk
back plate (left). The two Backplates at Cinel during the final leak test
performed for acceptance (right).

Its design has a key role for the success of positioning and holding the crystal matrix, and very long time has been spent to optimize this component, also to be sure crystals will be not damaged with its contact.
A detailed description of the design of this component and of the work done during my PhD activity are presented in chapter 6.

3.2.4　Backplate

The Backplate (Figure 3.6) has the main function to create a surface where all the SiPMs and FEE electronics can be placed and to keep them in position in the back of the crystals, to support the refrigerating system to cool them down and to thermal isolate the rest of the calorimeter from the cooling lines. For these reasons it has been designed as a machined PEEK plate with all the housing for the SiPMs, in order to bring them very close to the crystal lateral faces. Due to the difficulty to find PEEK plates of large dimensions, it has been realized with the gluing of two halves at Cinel (Vigonza), before to be CNC milled. Moreover, it is composed from the copper cooling lines which are embedded in its design, made of a carved copper beams, brazed with a copper pipes. Each line has a different pattern which has been optimized to be in contact with all the SiPM holders with approximately the same temperature. The lines are connected in parallel to two main distribution stainless steel collectors, one for the inlet and one for the outlet.
At the moment of writing, the two Backplates have been fully realized and tested by the manufacturer, with both pressure test and leak test, achieving a leak rate below $10^{-10} atm\ cc/s$, well inside the specifications. Some other tests for QC will be briefly performed at INFN Pisa, next a mounting test will be assembled at LNF before the shipment to Fermilab for the final calorimeter assembly.

3.2.5　Frontplate

The Frontplate (Figure 3.7) is the final component of the Source calibration system ([24]). It is made of a sandwich of two carbon fiber (CF) skins and an aluminum honeycomb core, properly grooved to house an aluminum thin pipe distribution
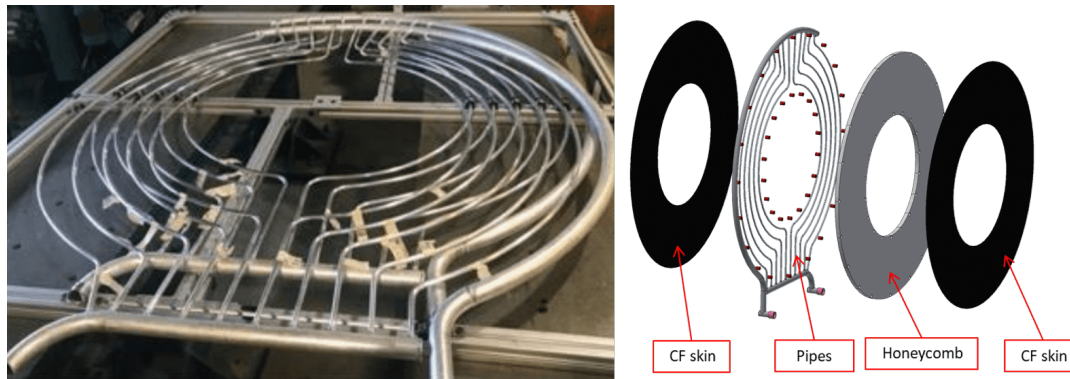
Figure 3.7: The two pipe system of the source that will be inside the Frontplate. (left). The CAD model of the Frontplate with all the components is made of (right).
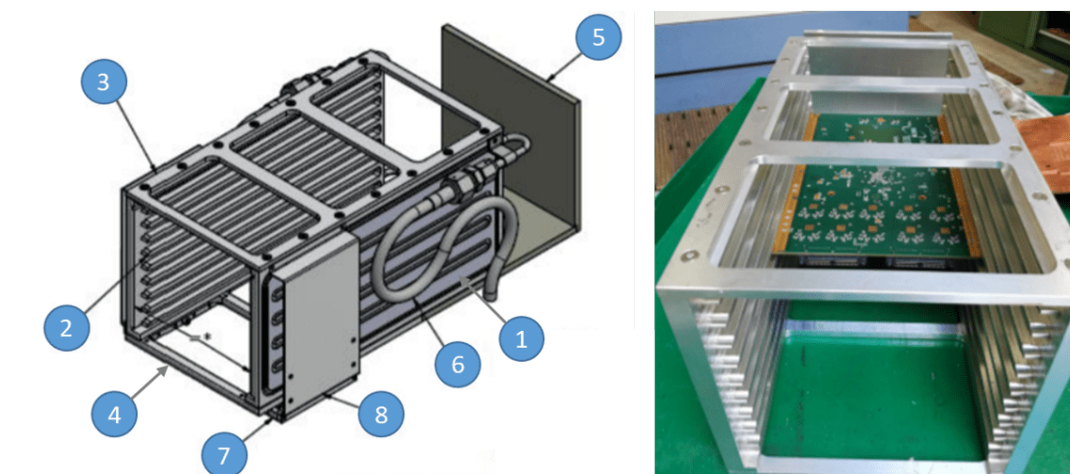

Figure 3.8: On the left the CAD model of a crate with its components: the external wall (1), the internal wall (2), the top (3) and the bottom (4) plates, the tungsten shield (5), the crate pipe (6), the crate cable rack (7) and the cable holding plate (8) . A picture of a crate prototype with a Digitizer board (right).

system. It will be placed in front of the crystals and will be positioned with high accuracy for calibration purposes. Due to its position, it must be very low mass, therefore the use of carbon fiber and aluminum, to interact as less as possible with the detecting particles.

First, pipes will be glued to the carbon fiber skin, to assure a precise positioning, and then embedded in the honeycomb grooved structure. The piping system has been already manufactured at the Argonne National Laboratory, while the mounting of the whole Frontplate, will be held at CETMA (Brindisi) where the Inner Cylinder is also realized.

3.2.6 Crate

The Digitizer boards, coupled with the Mezzanine boards, are placed in dedicated and cooled crates (Figure 3.8) positioned all around the aluminum outer ring. Beneath the crates the inlet and outlet crate manifolds run, with a pipe connection in
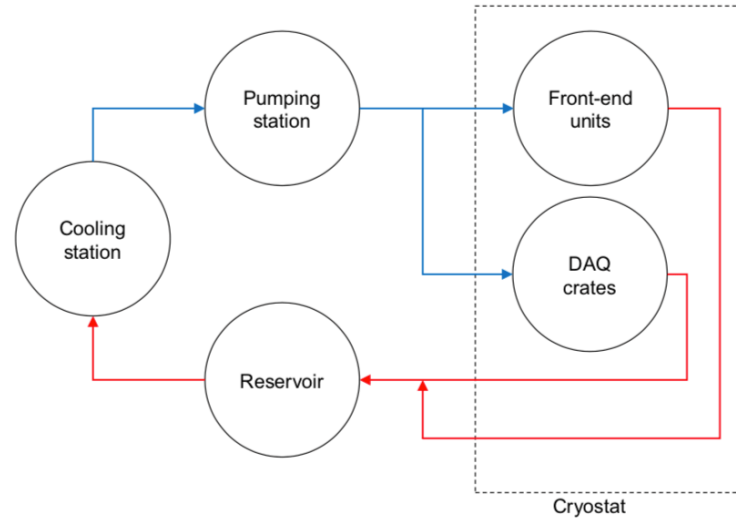
Figure 3.9: Schematic idea of the calorimeter cooling system.

parallel per each crate.

Each crate side is made of two plates TIG welded with a cooling channel milled in the middle of them, in order to have the best thermal performance and to save the very low space available. The front of the crate is made of a tungsten alloy, to protect the boards from the high intensity of ionizing radiation coming from the target. Beneath the crate, a couple of cable racks are installed to keep all the FEE cables in order and fixed to minimize possible damages during installation and maintenance. On the sides there are the two connections with a double Ω-shape to maximize their flexibility and simplify assembling.

Crate components have been realized by the TecnoAlarm (Rome), and they have been tested with high pressure and leak tests for quality purpose, and now they must be mounted and the last components must be welded. After that they will be tested again for any leak, and a mounting test will be performed, also to verify the realization of the crate manifold they must interact with.

3.3   Cooling system

Since electronics will operate inside a vacuum cryostat at 10^{-4} Torr, the cooling is a crucial element of the calorimeter[25]. The consequence of operating in vacuum is that a dedicated cooling system is necessary to remove the power dissipated by the electronic components. In this respect, the most sensitive components are the SiPM since their operational temperature must be kept below $0°C$ to minimize the leakage current induced by the neutron field. We plan to keep the calorimeter SiPM at the temperature of $0°C$ until the radiation absorbed during operation degrades their performance and forces to reduce their operational temperature to approximately $-10°C$. The thermal constraints for the electronic components employed in the DAQ boards are looser since in this case, operational temperatures of the order of $60°C$ are perfectly safe. The cooling system is based on the principle of a low temperature fluid flowing in a hydraulic circuit in thermal contact with the electronic components through a network of pipes. Electronic power is thus removed through
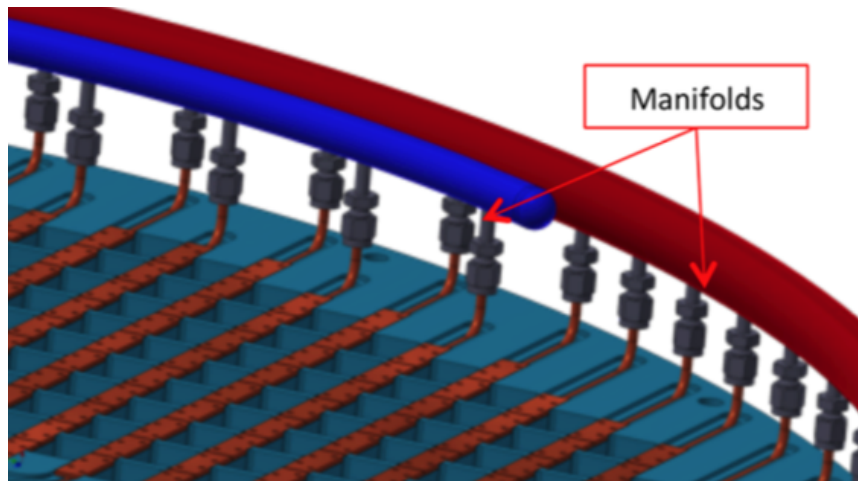
Figure 3.10: CAD details of the manifolds (blue for inlet, and red for outlet) and their connections with the pipe network.
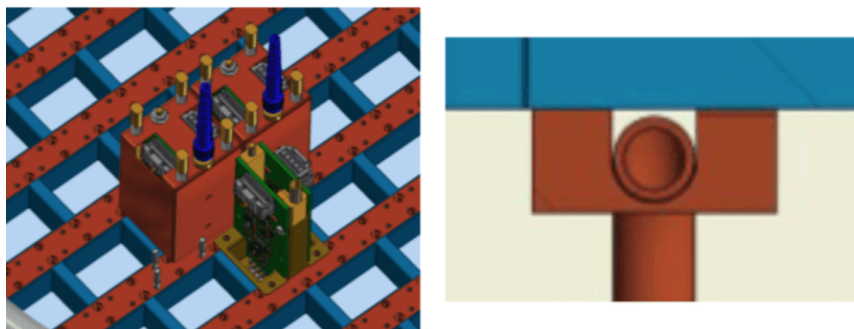

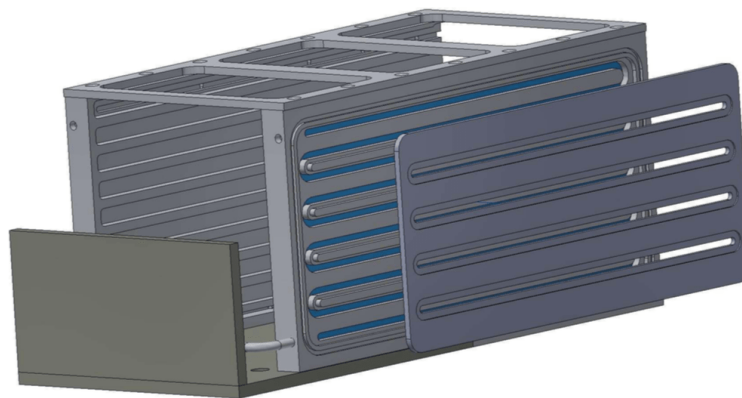**Figure 3.11:** CAD overview of the front end unit cooling system.

Figure 3.12: View of the internal cooling channel in a crate CAD model.

a combination of forced convection (fluid-pipe) and conduction (pipe-target component). The cooling system inside the cryostat is fed by an external hydraulic circuit which includes a cooling station and all the necessary services. The cooling circuits of the front-end units and DAQ crates, which are located in different zones of the detector, are branches of the same circuit. In other words, they share the same cooling and pumping stations outside the cryostat but have independent branches to cool
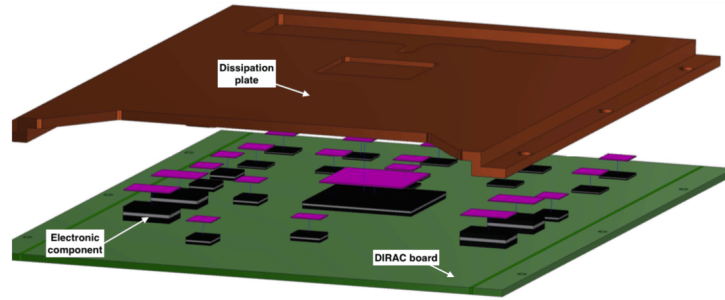
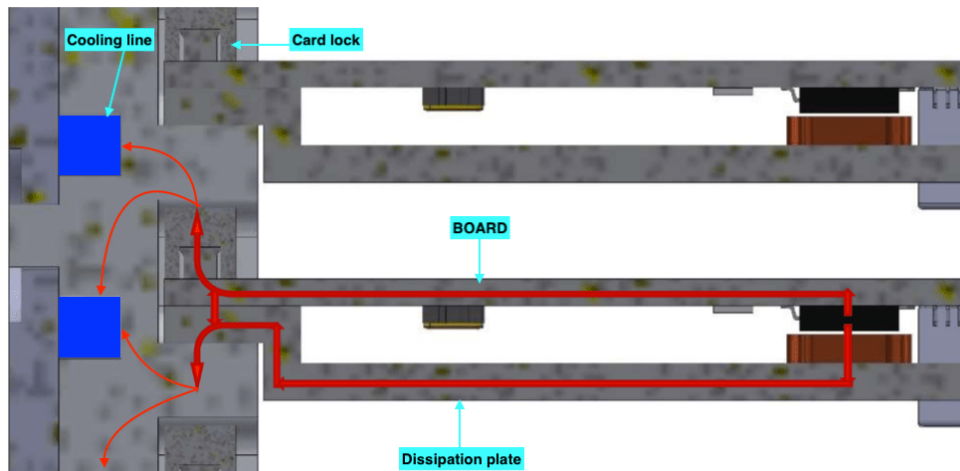**Figure 3.13:** CAD model of the DIRAC board.

Figure 3.14: Cross section of the crate assembly. The red lines reproduce possible thermal paths, while the blue squares represent the cooling lines (the heat sinks). The heat source is the black electronic components.

down the different zones. A simplified scheme of the cooling system is reported in figure Figure 3.9.

All the electronic components have an intrinsic power dissipation in form of heat production (due to the Joule effect). This heat, if not well disposed of, will rapidly increase the temperature of the components until a new thermal equilibrium is reached. In an insulated system like the calorimeter, in which the only form of available heat exchange is the radiation with the cryostat walls, the equilibrium temperature would be quite high in absence of a cooling system. The components of the calorimeter would reach a temperature at which their exchange of thermal power with the cryostat walls would be exactly equal to the incoming thermal power of the electronics. This of course would imply a calorimeter at higher temperature than the cryostat walls (25 °C). This temperature would not be acceptable for the electronics (in particular the SiPM, having requirements $< 0°C$). This is the reason for having a dedicated cooling system to keep the temperature of the sensors and of the electronic components at acceptable values.

Several tests and simulations have been performed over the last years ([26], [27]). In Table 3.1 some results are summarized.

The cooling system for the FEE zone consists of a network of 38 copper pipes connected with the inlet and outlet manifold to the routing system. There are 18 straight

Component	Unit power [W]	Total number	Total power [W]
Outer SiPM	0.16	2128	342
Inner SiPM	0.48	568	274
FEE boards	0.36	2696	957
DAQ crates	296	20	5920
Total			**7492**

Table 3.1: Thermal powers dissipated from the calorimeter electronics.

and 20 curved pipes with 180 degrees elbows for each calorimeter disk. The pipes have an internal diameter of 3mm and an external diameter of 4mm. Because of the small dimensions involved in this pipe network, it is important to have a pure and dirt-free fluid. This will be achieved by means of suitable filters located along the circuit. The pipe network runs between the back plate and the front-end units, removing heat via convection and conduction (Figure 3.10, Figure 3.11). The back plate performs the function of mechanical support for the FEE boards and for the cooling system itself. Each unit is joint to two pipe cases with four screws, and the pipe cases are fastened to the back plate with several screws as well. The pipe cases are made of copper just alike the pipes to reduce the thermal resistance of the path. Each pipe is connected to the inlet and outlet manifold by means of *Swagelok VCR* connectors (fig. Figure 3.10 right), which are brazed with an extremely careful procedure to make sure there is a high quality thermal connection. It is important that the fluid does not leak inside the cryostat because this would deteriorate the vacuum level, as well as produce other environmental problems. Also the cooling lines are brazed to their cases with a similar procedure using a pure silver foil 0.15mm thick. The cooling channels of the crates are directly milled inside their lateral panels (fig. Figure 3.12).The reason for this design is not only to improve the cooling but also for space efficiency. The crates are quite close to each other and have many features on their sides where external cooling channels would be cumbersome. Each crate is connected to the inlet and outlet manifold in parallel by means of Swagelok connectors. The manifolds are then connected to the main external line which supplies the cooling fluid at the right temperature and rate. A custom copper plate over Digitizer and Mezzanine board, fixed to the crate with two cardlocks, ensures the thermal contact between the integrated components and the crate (Figure 3.13, Figure 3.14).

Chapter 4

Dimensional and geometrical analysis of the production CsI crystals

The requirements in terms of physics performance described in the Final Calorimeter Technical Design Report [28] defined a set of specifications on the mechanical, scintillation and radiation hardness properties that the production CsI crystals employed in the calorimeter have to satisfy. The tolerance on the mechanical dimensions and shape is a critical parameter to allow a correct stacking and alignment of the crystals inside the calorimeter disks. At the end of the year 2016, a crystal pre-production selected three international vendors to control the crystals properties and allowed to choose the final providers for the calorimeter construction. The vendors for the Mu2e pre-production crystals were: Amcrys (Ukraine) [29], Saint Gobain (France) [18] and Siccas (China)[30]. Each vendor was required to produce 24 crystals to allow for a full characterization. At the end of the crystal qualification campaign, Siccas and Saint Gobain were selected. Information on the test performed on the pre-production crystals are reported in [31]. The Chapter reports a detailed description of the dimensional tests performed to qualify the production crystals.

The Quality Control (QC) procedure was organized as follows: a batch of 60 crystals were shipped from each producer and received at the FNAL Shipping and Receiving office and then sent to the Mu2e Calorimeter laboratory at SiDET, Lab A [32]. Here a visual survey was carried out to control the absence of large defects such as large notches, dents, scratches or bubbles. Soon after, the mechanical specifications were measured with the Coordinate Measuring Machine (CMM) always in SiDET. Each crystal that did not pass the mechanical requirements was rejected and sent back to the producer. Then the crystals were wrapped and the measurements of the optical properties and Radiation Induced Noise (RIN) were performed. Finally, the crystals were placed in drawers where N_2 was flown to keep the crystals in a humidity free environment. The radiation hardness tests were carried out on a small randomly selected sample in Caltech, Pasadena (USA) [33] [34].

4.1 Dimensional and geometrical survey

The goal of the measurements is to verify the dimensions and geometrical constraints of the CsI un-doped crystals that will compose the Mu2e electromagnetic calorimeter. Because of the calorimeter design, and of the piling up technique we will use in the assembly, very demanding dimensional and shape specifications were
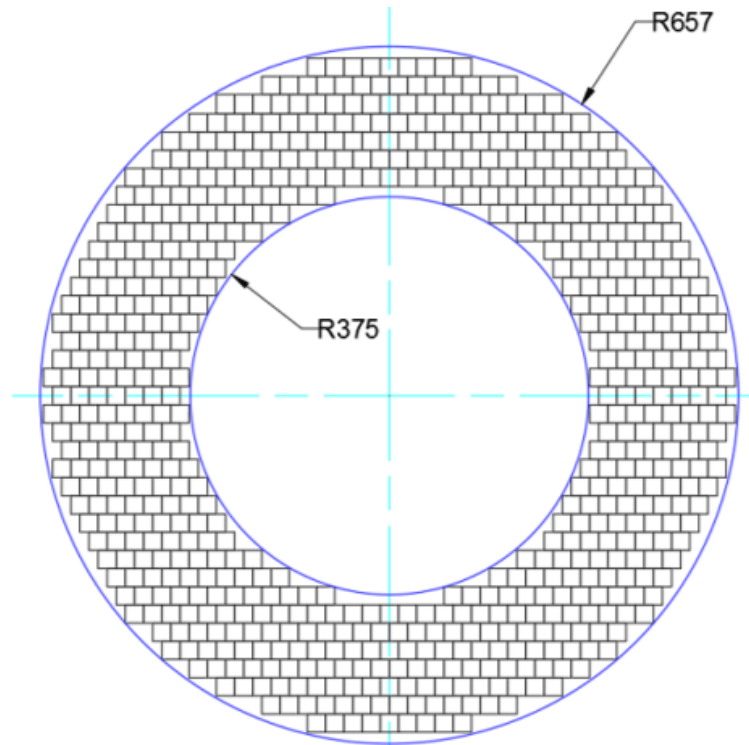
Figure 4.1: Crystals layout in the calorimeter disk. Crystals are placed in a circular region with an inner diameter of 750mm and an outer diameter of 1340mm.

required to the vendors. Each calorimeter disk is composed of 674 staggered crystals, placed in a ring-shaped hollow (Figure 4.1). The perpendicularity and parallelism of the surfaces, more than crystal side dimensions, are very important for a precise alignment of each row and the rising of unwanted peaks of pressure over the crystals matrix.

After considering the disk assembly procedure, a set of mechanical specifications for the CsI crystals have been decided. They are listed in the following, assuming all measurements are taken at the Standard Ambient Temperature of 25°C:

- Each crystal is a rectangular parallelepiped with dimensions 34 mm x 34 mm x 200 mm.

- The mechanical tolerance is of ±0.10 mm for the short sides and ±0.20 mm for the length. To avoid cracking the edges, chamfers of 0.3 mm × 45° must be provided on all edges.

- The crystals shall be free of curves and must have parallel and square sides and faces. In particular, the top and the front surfaces have a flatness constraint of 0.1 mm; the bottom surface has a parallel constraint of 0.1 mm to the top surface; the rear surface has a parallel constraint of 0.1 mm to the front surface; the front surface has a perpendicular constraint of 0.1 mm to the top surface (Figure 4.2).

- The crystals shall be free of cracks, chips and fingerprints. They shall be inclusion-free, bubble-free and homogeneous. The surfaces are defined referring to a duplet of dot marks on the left and top surfaces (as shown in Figure 4.2).
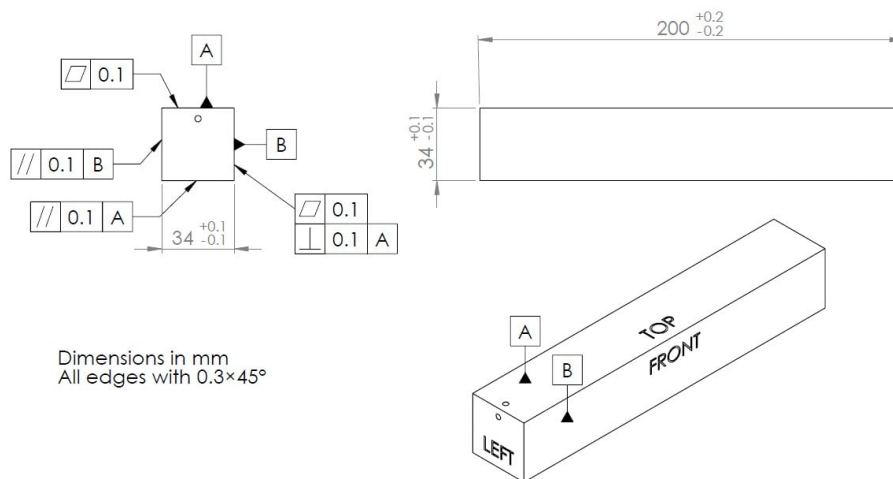
Figure 4.2: Crystal mechanical drawing.

These marks are placed randomly in LabC, when the crystal is unwrapped for the first time once it is arrived at Fermilab from the vendor. The crystal orientation will be maintained constant also in the follow-up QA steps up to the piling up process.

4.1.1 The measurement procedure

Measuring set-up

The measuring process took place in the LabC Clean Room at SiDet (Fermilab). It consisted in the measurement of a finite number of points per surface with a Coordinate Measuring Machine (CMM) [35] [36]. After the operator has defined the orientation of the crystal and has checked its integrity and excluded the presence of any kind of mechanical defects, the crystal is placed on the CMM, ready to be measured. The CMM is a Hexagon machine and the reconstruction software is the PC-DMIS 2013. The repeatability of the CMM is of $\pm 2\mu m$ per axis. The probe is 5 mm diameter ruby ball with a 50 mm long shaft, and with a contact pressure of 2÷5 mg. The setup of the CMM is a granite table with two steel parallels ($1/4'' \times 1/2'' \times 6''$) glued on it. On the top of each parallel, a Teflon foil is placed to reduce the probability of damaging or producing scratches on the crystal surface, which is very delicate. The crystal is placed with the front face aligned to the parallel front small sides and approximately symmetrical between the two parallels.
Before starting the measurement process, the calibration of the probe is performed. Moreover, the CMM operator teaches the machine the location of the crystal to prepare the CMM for the measurement routine. These operations are performed every time the CMM is restarted. Once the CMM has been calibrated, the crystal measurement takes place.

The coordinate system

The first step is the definition of the crystal coordinate system, which the CMM uses as a reference. To do this, the CMM collects 7 points: four on the top surface (#2, 3, 4, and 5), two on the front surface (#6 and 7) and one on the left surface (#1). The
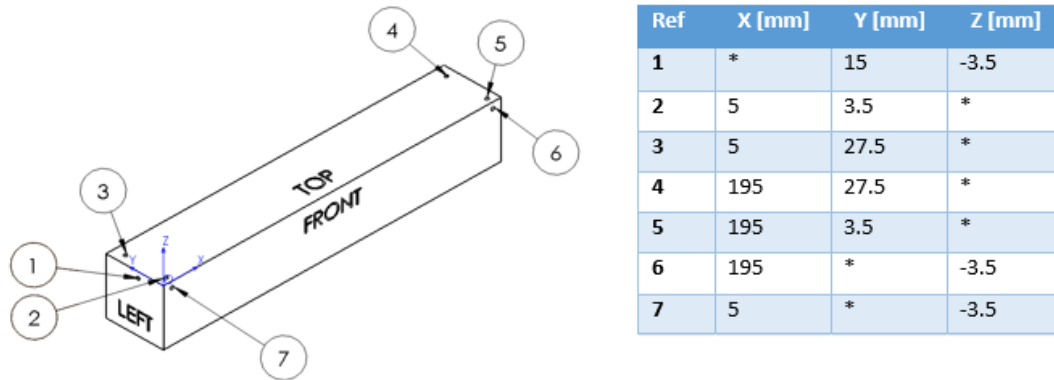
Ref	X [mm]	Y [mm]	Z [mm]
1	*	15	-3.5
2	5	3.5	*
3	5	27.5	*
4	195	27.5	*
5	195	3.5	*
6	195	*	-3.5
7	5	*	-3.5

Figure 4.3: Coordinate system points position.

program creates the best-fit surface of the first set of four points (calling TOP surface). Then it creates the perpendicular surface to the TOP surface passing through the second set of two points (calling it FRONT surface); at the end it creates the surface perpendicular to the TOP and FRONT surface and passes through the last set of one point (calling it LEFT surface). The right-handed coordinate system is defined by the intersection of the three surfaces, as shown in Figure 4.3. In the Table below, the coordinates of the acquired points are showed. The '*' represents the values the CMM acquires and uses to calculate the best-fit planes.

The closeout points

The next step is the acquisition of the 'closeout points' which are reference points to verify the absence of any rigid movement of the sample during the measurement process. The CMM acquires the position of ten points at the beginning of the measurement. The same points are re-measured after completing the crystal survey to check if any movement has occurred in the meanwhile. If there is a discrepancy in these closeout measurements greater than $\pm 15 \mu m$, the measurement will be repeated. Depending on the value obtained, we can understand if the crystal was moved or deformed during the measuring process.

In Figure 4.4 the layout of the closeout points is shown. In the Table below, the coordinates of the closeout points are showed. The '*' represents the values the CMM acquires and check again at the end of the measurement.

The measuring process

At this point, the CMM starts collecting points on the surfaces. There is the acquisition of 20 points on the long surface and 16 points on the short surfaces, for a total of 112 acquisition points. The whole measuring procedure, which includes the coordinate system acquisition and the closeout points takes less than 9 minutes.

After collecting all the data, the software calculates the best-fit surfaces of all the measured surfaces, and then it proceeds and evaluates the sizes of the crystal, the flatness of the surfaces and the parallelism and perpendicularity values. In detail, the software proceeds with evaluating:

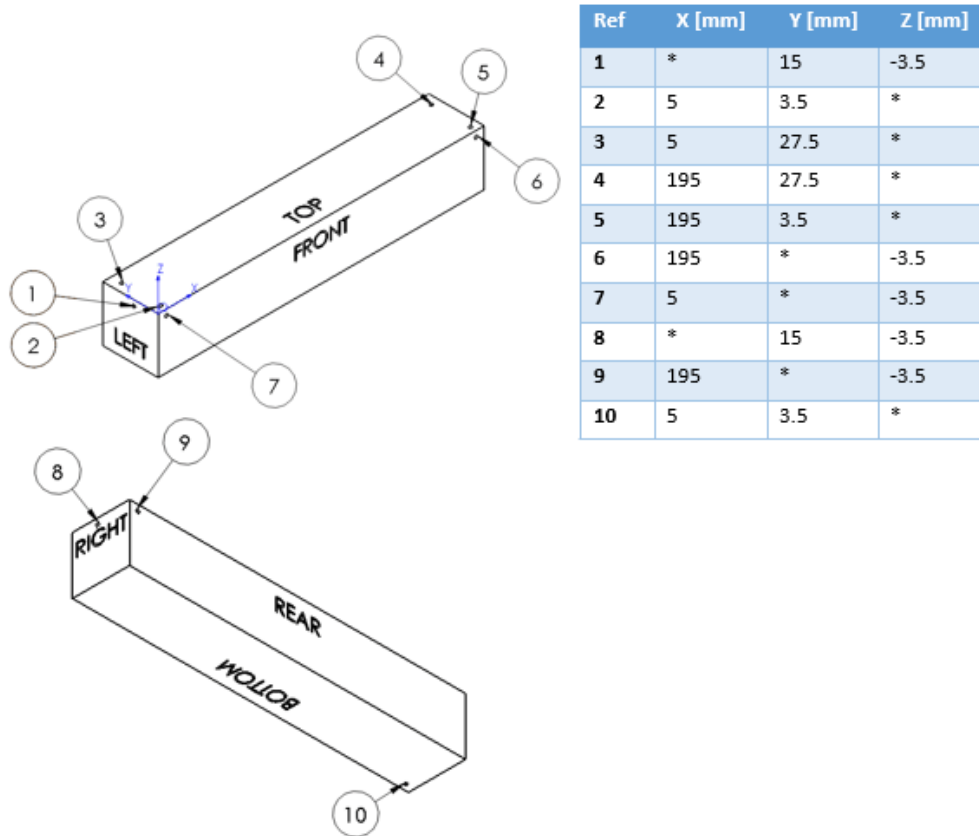- The distance between each couple of opposite points (56 in total);

Ref	X [mm]	Y [mm]	Z [mm]
1	*	15	-3.5
2	5	3.5	*
3	5	27.5	*
4	195	27.5	*
5	195	3.5	*
6	195	*	-3.5
7	5	*	-3.5
8	*	15	-3.5
9	195	*	-3.5
10	5	3.5	*

Figure 4.4: Closeout points position.

- The planarity of each surface (the maximum deviation that each measured point has respect to the best fit plane whose it is part) (6 in total);

- The parallelism of the TOP surface to the BOTTOM surface;

- The parallelism of the BOTTOM surface to the TOP surface;

- The parallelism of the FRONT surface to the REAR surface;

- The parallelism of the REAR surface to the FRONT surface;

- The parallelism of the LEFT surface to the RIGHT surface;

- The parallelism of the RIGHT surface to the LEFT surface;

- The perpendicularity of the TOP surface to the FRONT surface;

- The perpendicularity of the FRONT surface to the TOP surface;

- The perpendicularity of the TOP surface to the RIGHT surface;

- The perpendicularity of the RIGHT surface to the TOP surface.

All data are stored in three different .RTF file:

- Long file, with all the measurement data;

- Short file, with all the evaluated date presented above;
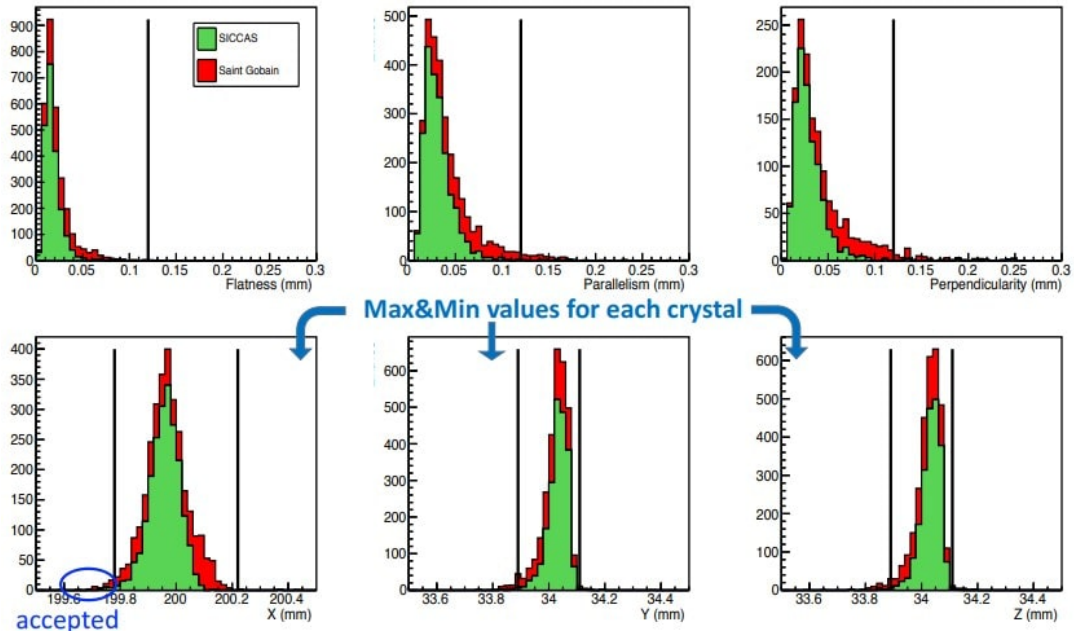
Figure 4.5: Results of the CMM measurements on the production crystals. Flatness (top left), parallelism (top center) and perpendicularity (top right) and the X (bottom left), Y (bottom center) and Z (bottom right) dimensions. The black lines represent the requirements.

- Closeout file, with all the closeout measurement.

The Closeout file is used to check if there has been any movement during the measurement process. The Long file is used to plot the shape of the crystals and for a very good evaluation of its surfaces. The short file is commonly used to the QA process of accepting or refusing the crystal from vendors.

4.1.2   Survey results

As specified at the beginning of this chapter, for the evaluation and consequentially the accepting and rejecting of crystals to the vendor, only a part of the dimensional and geometrical characteristics have been taken in consideration, in detail:

- The distance between each couple of opposite points (34±0.1 or 200±0.2 mm)

- The planarity of the TOP surface (≤0.1 mm)

- The planarity of the FRONT surface (≤0.1 mm)

- The parallelism of the BOTTOM surface to the TOP surface (≤0.1 mm)

- The parallelism of the REAR surface to the FRONT surface (≤0.1 mm)

- The perpendicularity of the FRONT surface to the TOP surface (≤0.1 mm)

At the moment of writing this Thesis (March 2021) all the crystals have been delivered and measured, despite some problems rose up during the production (see section 4.1.3) and stored carefully in nitrogen fluxed cabinet at Sidet waiting for the calorimeter assembling to begin.
In Figure 4.5 the dimensional survey results is presented highlighted the manufacturer.

4.1.3 Dimensional problems

During the process of the crystal dimensional QA some unexpected problems were found probably as the consequence of several causes, such as bad manufacturing or handling process. In this Section the most important ones and how they were managed are briefly described.

Dimensions out of specifications

The most important problem we had to manage has been a large number of crystals produced from the Saint Gobain which were out of specs, especially for the unsatisfactory parallelism and perpendicularity. The vendor must commit the 50% of the whole production and this bad dimension quality had an important impact on the calorimeter schedule. The problem consisted in an 'barrel' shape which characterized many crystals, i.e. a thicker size in the central part of the crystal, and a thinner size on the edge (Figure 4.6). This bad shape was unacceptable, due to the out of specification of those defects, and to the weak and movable structure the staggered crystal wall would have after piling up in the calorimeter.

After some investigation and a survey at the vendor site (Fontainbleu, France), the cause of this defect has been found in the manufacturing process and in a lack of a good QC process. After the formation of the crystal, it is cut manually with some over-left material at the bandsaw. After this process, a sanding and polishing process took place. An expert and qualified technician gently pushes the crystal on a spinning wheel with some abrasive paste and refrigerant solution. Because of the pressure applied from the operator, and because of the different tangential speed velocity of the wheel, the amount of material removed was major in the extremity part of the crystal. So the combination of the handy polishing process with a not precise starting shape resulted in a systematically 'barrel' shaped crystals out of tolerances.

The other problem was the lack of a good QC process afterwards. Crystals were only measured for the parallelism on a granite measuring table with one dial indicator, which can only display the maximum size dimension of the crystal, without any check on the parallelism and perpendicularity. The direct consequence was that a lot of crystals were shipped at Fermilab, requiring a high amount of time in managing, unwrapping stacking and measuring, despite they were out of tolerances. So our QC control was able to figure out the out of specs crystal, that were sent back to the vendor for replacement.

The proposed solution to the Saint Gobain, was to use a milling operation at the first shaping process, in order to have good tolerances to the row crystal and avoid having a sanding process, but only a polishing process, to avoid removing too much material. Moreover, to build a measuring device with multiple dial indicator mounted orthogonally which can show some perpendicular and parallel values after the polishing phase. Those solutions were applied to the vendor, resulting in good quality shaped crystals, but the increase of costs and the very slow production (because of some internal machines availability), forced the company to quit from the contract. So Siccas produced the 250 crystals missing for the calorimeter in late 2020 (Figure 4.7).
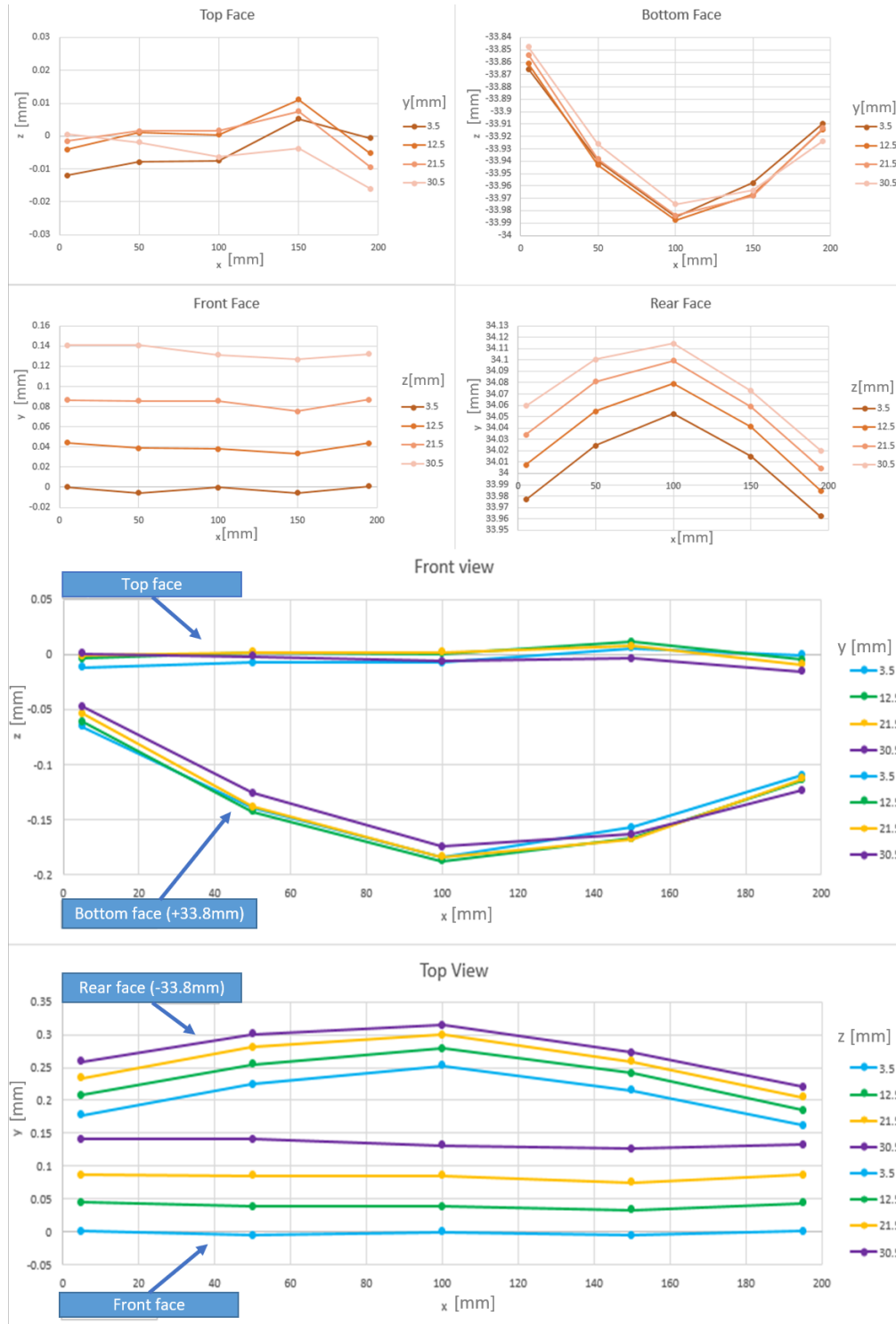
Figure 4.6: Example of a Saint Gobain crystal dimensions. In the left image, surfaces of the four long sides of a crystal have been displayed. In the right image, front an top view of a crystal is shown (sides are off-set by 33.8mm to underline the shape)

Machining chips

A problem that has been found on the Siccas crystals was the absence of a chamfer. This has result in a sharp edge which was easily bumped or deformed. Especially
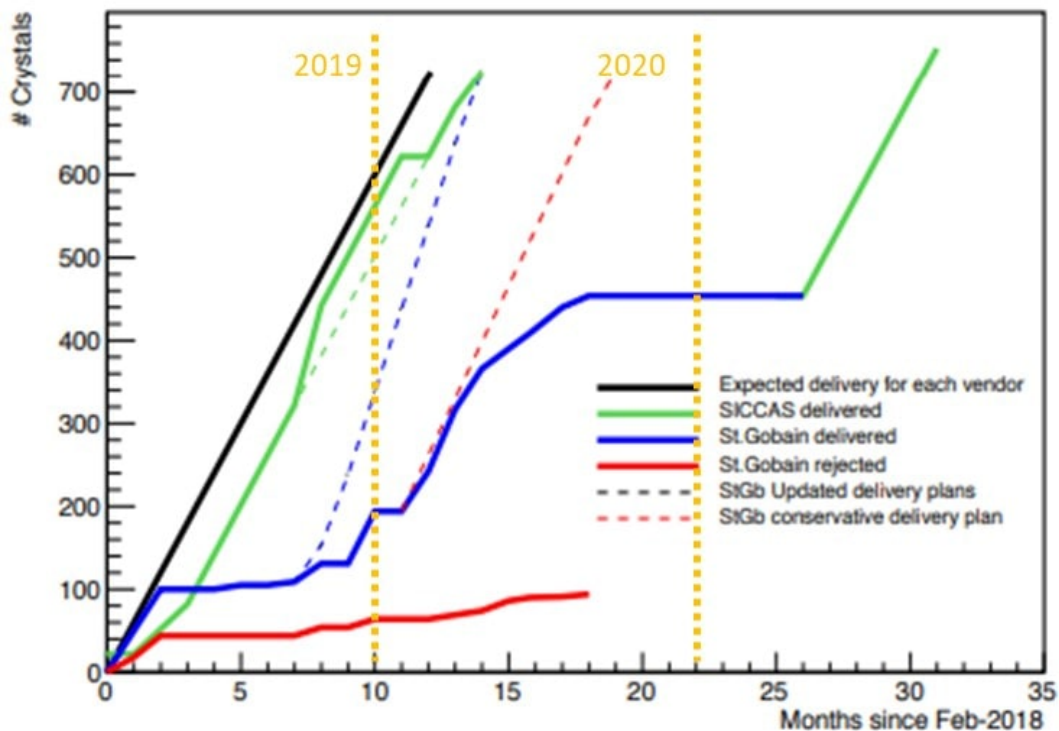
Figure 4.7: Status of the crystal arriving at Fermilab, the black line represents the expected crystals delivery for both vendors, the dashed and the solid green lines represent respectively the expected and the effective delivery plan of crystals from Siccas. The dashed and the solid blue lines and the dashed red line represent respectively the original, the effective and the updated plan of the delivery of crystals from Saint Gobain. The solid red line is the number of rejected crystal from Saint Gobain.

during stacking the edges would be the critical spots were undesired deformations and stresses would take place.

Siccas producer was quickly notified and they provided to add a chamfer machining on the next crystals. The side effect of this was the presence of small machining chips on the crystal surfaces, probably because of a missing cleaning procedure after. Those debris were not seen at firsts visual inspections, but they create an unpleasant consequence. During the measuring procedure at the CMM, sometime a small debris interferes with the measuring tip, resulting in an increased dimension acquired ($\approx 30 \div 60 \mu m$) from the machine, and causing a false out of specs crystal. We were able to notice that because the out of specs values were just localized in one measurement over the multiple points of a surface scan (Figure 4.8). We organized a cleaning procedure after unwrapping the crystals with a clean cloth and pressurized nitrogen.

Size shrinkage

Sometimes a discrepancy of the closeout points has been observed for the changing of sizes because of the humidity level in the clean room. This effect was very pronounced with the Saint-Gobain crystals. Indeed, those crystals have been packed in vacuum bags with in silica gel packages. It creates a very dry environment. The
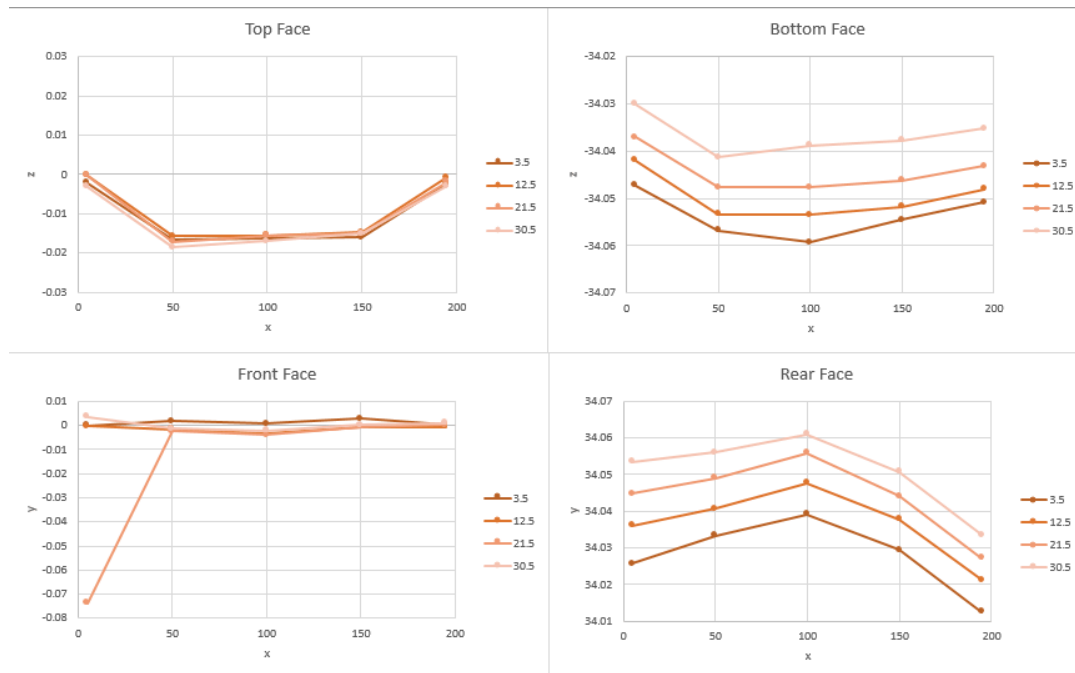
Figure 4.8: Example of a Siccas crystal dimensions. The unnatural point displayed resulted in a debris on the crystal surface. After cleaning and remeasuring that value was in trend with the others of that surface.

relative humidity (RH) in the LabC clean room is below the 40%, and this variation causes the shrinkage of the crystal. To minimize this effect, crystals are usually unwrapped and left exposed at the LabC air for approximately 30 min. This has solved the problem of a possible movement under the measuring process at the CMM.

Corner bumps

Another defect we found on some crystals was a bump on the corner. Indeed the CsI crystal has a very plastic behavior and a very low tensile yield point (See chapter 6). For these reasons it probably happened that during manipulation and shipping, a small bump on the corner was produced. The problem was that the CMM scan program did not take in account localized defects, but only macroscopic surface dimensions (Figure 4.9). In order to avoid bumps that could compromise the staking process in the calorimeter assembling, a dedicated program has been written to check corner exclusively, with a point-to-point probe contact point distance of 1 mm, on a 25 mm^2 surface per side. This process has been applied to the crystal corners who present a naked eye visible bump in the visual inspection, to avoid spending lots of time for an occasional visible defect.

4.2 Crystal piling up measurements

Despite crystal measurements are strictly checked with a dedicated QC process at Fermilab as described before, these are not the only characteristics to keep under control and monitoring before the whole calorimeter structure was complete to be sure to have a precise positioning of crystals in the matrix. Each crystal is wrapped
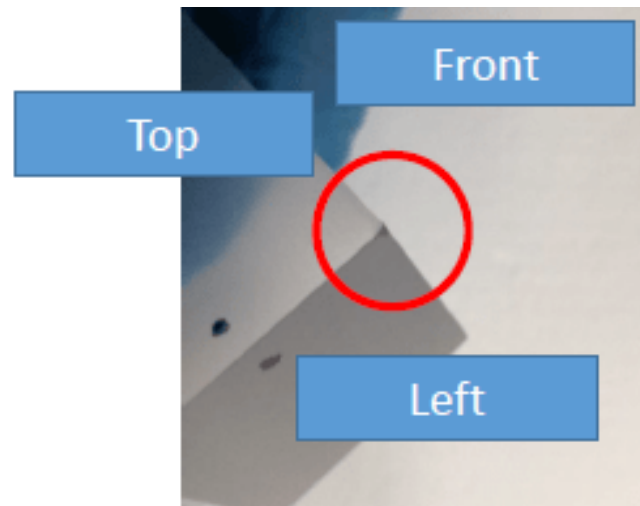
Figure 4.9: Example of a bumped corner on a CsI crystal

with a reflective layer of Tywek and another layer of absorbing light il placed between each crystal to avoid cross talk effects during data acquisition. This means the crystal matrix has different layers of materials which will modify the theoretical crystal positioning. To prevent this shifting and to estimate the real crystal positioning in the calorimeter staggered matrix, some experiments have been performed, mocking up a vertical and horizontal row of crystals and measuring their true position. The results [37] [38] have been used to size the aluminum external step structure and the carbon fiber internal step structure.

Each crystal, once it has been measured and the absence of defects has been verified, is wrapped in a Tywek sheet which cover all the long sides, glued on two frames (one for the LEFT surface and one for the RIGHT one) and closed with a tape on the TOP surface. Next, a lid, with two Tywek square foils is applied on the LEFT of RIGHT surface (it depends by crystal LTU) (Figure 4.10). Because of the process of wrapping, and the tolerances of components, the size of each wrapped crystal can vary, and this effect affects also other crystals when they are piled up vertically and horizontally.

Because of the difficulty to calculate this situation, some tests have been prepared and will be next described, with the aim to formulate a model to predict the real position of each crystal in the final assembly, both for vertical and horizontal alignment.

4.2.1 Vertical set-up

The measuring process took place in the LabC Clean Room at SiDet (Fermilab). It consists in the measurement of a finite number of points on the upper surfaces of a staggered crystal tower with a Coordinate Measuring Machine (CMM). The CMM is a Hexagon and the reconstruction software is the PC-DMIS 2013. The repeatability of the CMM is of $\pm 2\mu m$ per axis. The used probe is 5 mm diameter ruby ball with a 50 mm long shaft, and with a contact pressure of $2 \div 5$ mg. Before starting the measuring process, the calibration of the probe is performed. Moreover, the CMM operator teaches the machine the location of the crystal, in order to prepare the CMM for the measuring routine. These operations are performed every time the CMM is
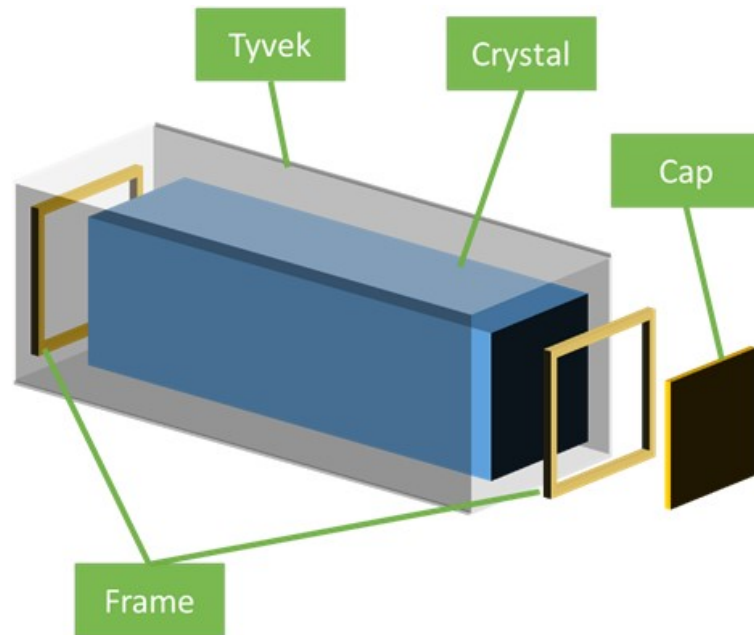
Figure 4.10: Wrapped crystal exploded model.

restarted. Once the CMM has been calibrated, the measurement take place.

We built the staggered tower with crystals, and we placed a fake crystal in each hole in both side of the 3-crystal layer. Fake crystal is made by plastic material and its height is 34.1 mm. We compensated for the difference with Tyvek foils, in order to recreate a flat surface every layer, and to be sure the fake crystals were smaller of all the crystals. The positioning of each crystal has been made similar to what we are going to do during the assembly of the calorimeter, in particular all the caps have been placed upfront, and the aluminum tape on the side. We used the ceramic square for a side hard stop and an iron flat surface on the back. After we built the tower, we compressed the two sides with 3 vices at different heights, and we started measuring top to bottom, removing crystals layer by layer. We un-tighten slightly the vices to remove the crystals if necessary. Because of the height of the ceramic square and of the steel side plate, the last 3 layers have not been compressed on their side. The number of built layers was 21, with 3 and 4 crystals each (alternately) for a total amount of 74 crystals. In the calorimeter we will have a maximum "column" of 37 crystals, but for space constraints on the CMM we had to stop at the 21st one. Because of the presence of the Tyvek cover, a false trigger of the touching probe can occur. This is because the Tyvek layer is not attached to the crystal surfaces, but it can create wrinkles and bubbles, and it can cause a wrong measurement. To eliminate this problem, we used an aluminum crystal we know the dimensions of, as measuring surface. We put it on the top of each crystal before to perform the measurement, and it compressed the Tyvek layer enough to make it flat. We also set up the origin plane using this aluminum block, so our measurements are rightly shifted. The employed coordinate system is shown in Figure 4.11 (left).

4.2.2   Vertical measuring results

All the points acquired per plane have been compared to look at the planarity precision each layer has. We calculated the average height for each top layer plane and
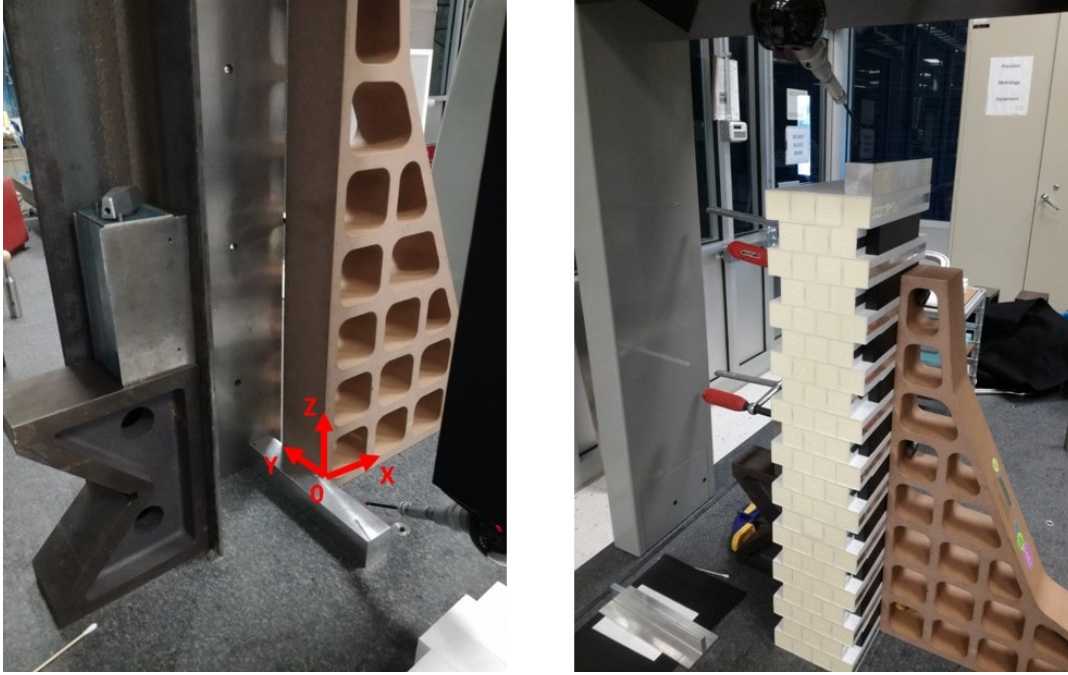
Figure 4.11: Vertical measurement set-up and coordinate system (left). Crystal staggered tower during measurement (right).

its RMS. Next, we calculated a best fit linear regression to have an estimate of what we will have at the 37th layer. In Figure 4.12 RMS values, their calculated errors, and the best fit linear regression are presented. In that figure the first 21 layer-points are the measured data, and the 37th is the estimate with the best fit linear regression, which is 174 $\pm 19 \mu m$. Considering a flat and symmetric distribution (observed in the dataset), the maximum estimated excursion for the 37th layer will be:

$$\delta_p lanarity = \pm \frac{\sqrt{12}}{2} \sqrt{RMS_{37}^2 + errRMS_{37}^2} = \pm 0.303 mm \qquad (4.1)$$

where RMS_{37}^2 is the calculated RMS for the 37th layer with the best fit linear regression (174μm), and $errRMS_{37}^2$ is its error 19μm.

Fixed height model

At this point we tried to create a simple model to estimate the pitch between the crystals. The easiest model we can think of is a fixed height crystal model. The assumption is that each crystal will have the same height, that has been calculated to obtain the best fit linear regression with the data obtained. This kind of model will be very helpful in the design and manufacturing of the calorimeter component, having just one pitch to insert, not depending on the chosen crystals. In Figure 4.13 the residuals between this model (with a crystal fixed height of p = 34.354 mm) and the average of the 'tower' measured layer has been shown. The model keeps in consideration 34 mm per crystal, 0.3 mm because of the Tywek wrapping per crystal, and an additional 0.054 mm correction per layer, because of the not exact shape and positioning of the 'tower'. Even if this model does not perfectly fit the acquired dataset, it still gives us a good average correction to use to define the pitch of the
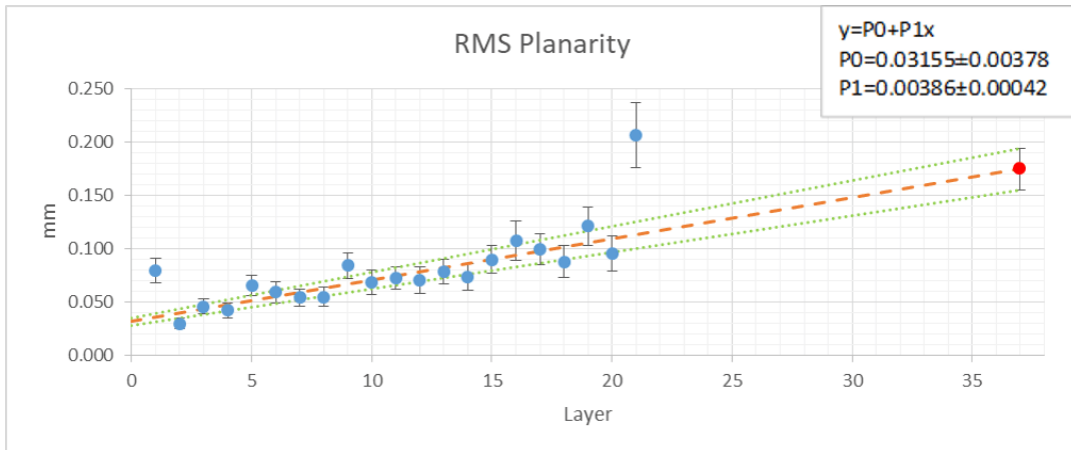
Figure 4.12: RMS values for each layer and best fit linear regression.
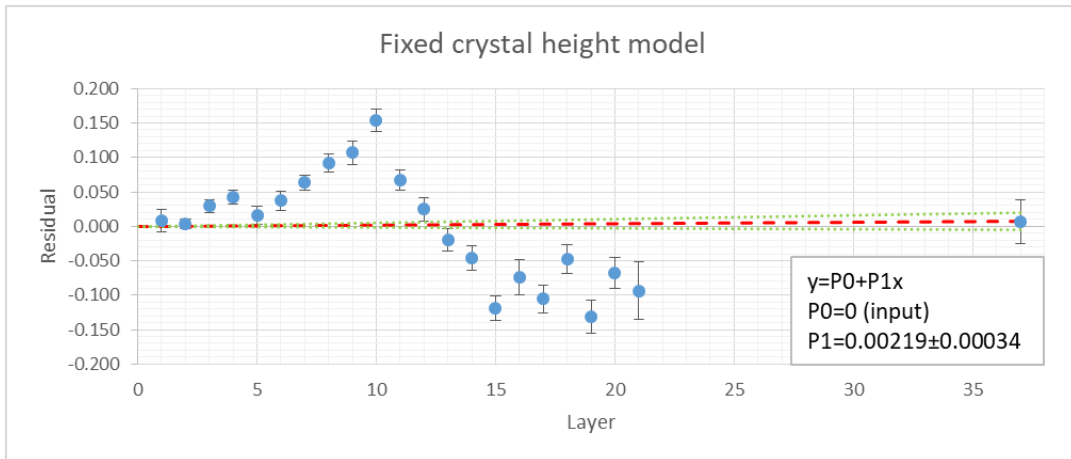The 37th layer point is an estimate.

Figure 4.13: Residuals of the average layer height compared to the
fixed height model.

mechanical structures. The discrepancy between the model and the acquired data is justified by the real height of the crystals. Indeed, the crystals are not exactly 34 mm, but they have some fluctuations. Different model has been tested, but that one which give the best result has been the average of maximum crystal height per layer, and it will be presented in the next paragraph.

Average of maximum model

Each crystal has a parallelepiped shape within some tolerances. It means it can deviate from the theoretical shape, for size and shape. We have collected previously a dataset of measurements for each crystal, defining its shape and size. Those that were out of specs [39], [40] have been discharged, and only the better one has been kept. So we decided to compare the measured tower height with the average of the maximum crystal height used for each layer, with a certain steady correction because of the Tywek and the piling up. In particular, 0.312 mm of thickness has been added to consider this effect, and to get a best fit regression with very negligible accumulating effect layer by layer. The residual has been presented in Figure 4.14.
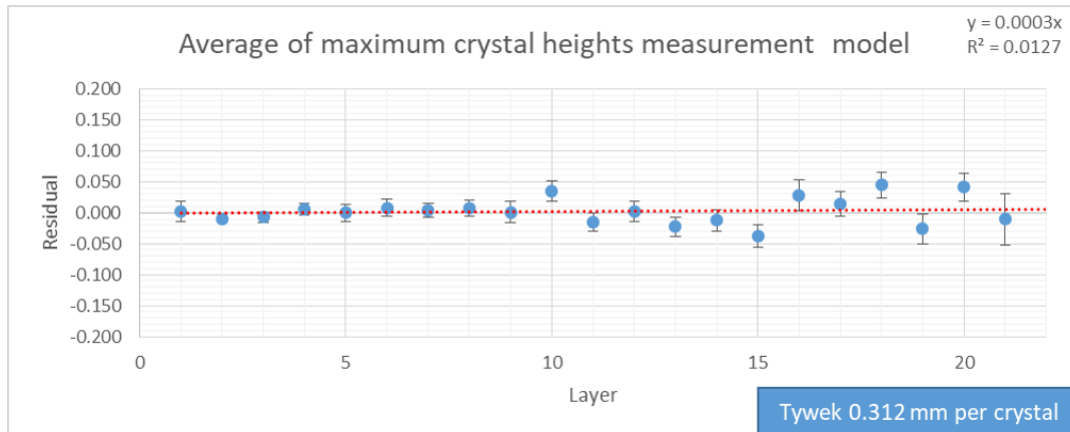
Figure 4.14: Residuals of the average layer height compared to the average of maximum height model.
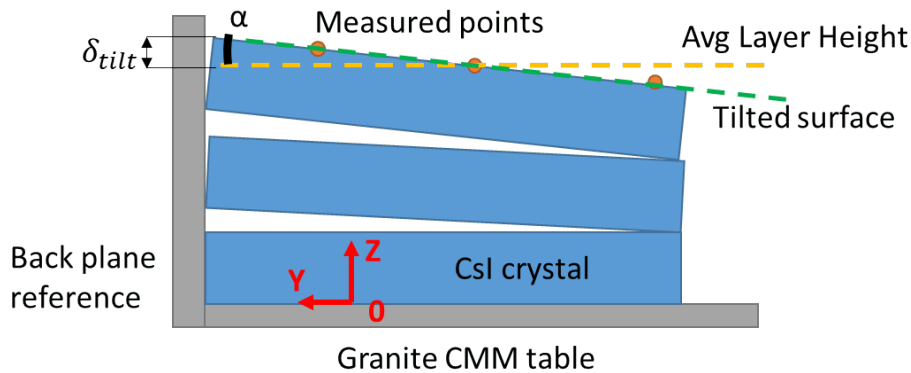
Figure 4.15: Tilting of crystals model.

This model seems to approximate very well the accumulated obtained height, but it is not very helpful in the pitch design process. We used this knowledge, to decide to bin crystals based on their maximum heights, in order to have a layer composed by the same max height crystals. Moreover, we can decide crystals we would like to use and their locations, and have a simulation about their accumulated position before the real stacking procedure, and correct it if anything we dislike will occur. We can also correct the height of the layer adding shims if necessary. We decided to bin crystals with differences of 25 μm but to do not correct anything if below of 100 μm.

Tilt correction

We have tried to see if there was an underlying reason for the large RMS found in each layer. We remind that for each stacked crystal we measure 6 points, 2 close to the front plate, 2 in the middle and 2 in the far side, along the crystal axis. We were therefore able to measure a possible tilt along the x axis. Analyzing those data, we discovered a sort of increasing tilting on the side touching the reference back plate. In Figure 4.15 a representation of this effect has been sketched out. The possible cause of this effect is the positioning of the frames one above each other, exactly
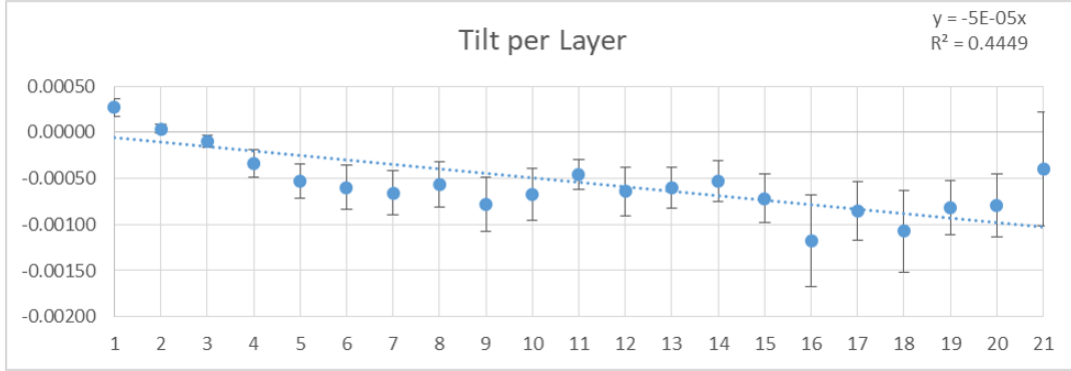
Figure 4.16: Layer tilt angular coefficient.

aligned, and because of their tolerances and their manufacturing process (3D printing), they will be greater than the crystal sides, accumulating this effect layer by layer. On the opposite side, this effect is mitigated due to the not exact length of each crystal, causing a not perfect alignment of the frames on the front side. In Figure 4.16 this effect has been presented and a best fit linear regression used for the estimate of the 37th layer. The value of the parameterized tilting is:

$$m = tan\alpha = 0.00005 \cdot Layer \qquad (4.2)$$

Considering the position of the measured points, the difference of the highest crystal point for each layer and the layer measured average height is:

$$\delta_{tilt} = m \cdot 124.5 = 0.006mm/Layer \qquad (4.3)$$

It means that for the 37th layer we will have an estimate deviation of 0.230 mm of the crystal back upwards. This effect is already taken in consideration when evaluating the top surface error distribution. Summing all the previous effects, we are able to estimate the mechanical pitch of the steps and SiPMs bores inside the calorimeter:

$$Pitch_{vertical} = p + \delta_{tilt} = 34.354 + 0.006 = 34.360mm \qquad (4.4)$$

4.2.3 Horizontal set-up

We performed a similar analysis also for the horizontal direction. The differences are that the crystals are not staggered, and this helps a lot for the positioning and the evaluating process. On the other hand, there is the aluminum tape placed on the side which will modify the crystal dimensions.

Crystals have been placed one by one, starting from a hard stop made of steel V-blocks. All the aluminum tapes have been placed on the side, in the same way they will be placed on the final assembly. We used a steel ruler as reference for the alignment of the crystals. After all the crystals have been placed, a parallel steel block of half inch thickness has been used as reference measuring surface and to surface where to push, to squeeze crystals between them. To perform the squeezing process, a couple of vises have been used and pushed by bare hands applying an approximately equal force between them. The measuring points have been taken randomly on the steel parallel block along its length. We were able to place 33 crystals, which
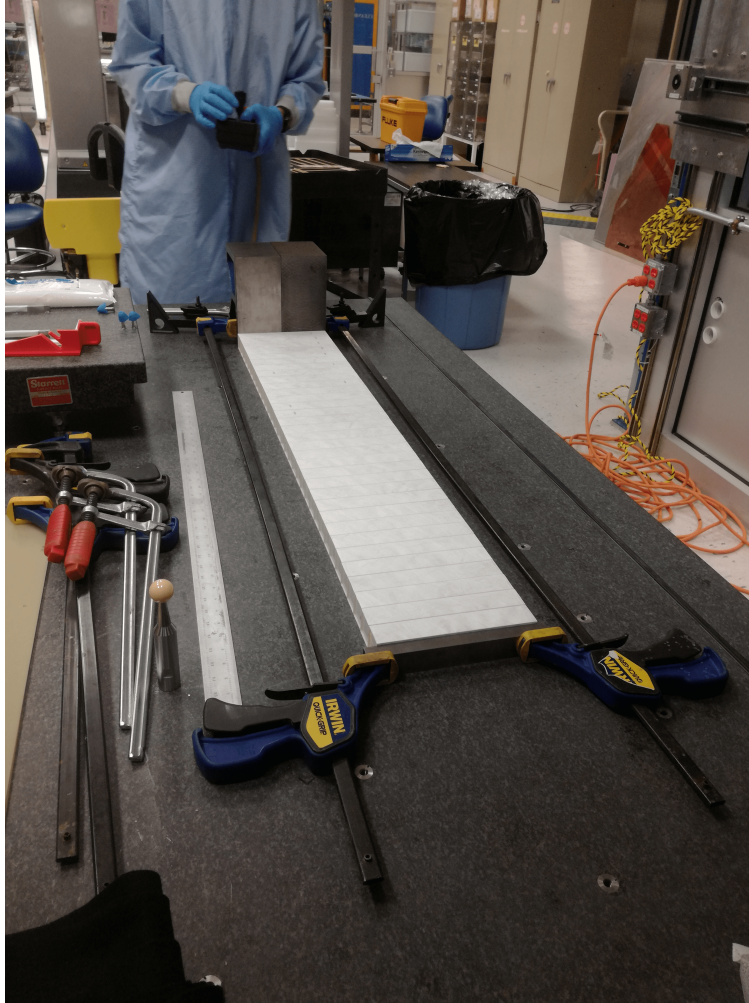
Figure 4.17: Crystal row measurement test.

is the maximum crystal row we will have in the calorimeter disk. After the measurement we had check the reference surface did not move during the measuring process.

4.2.4 Horizontal measuring results

We did not record the crystals which have been chosen during this measurement. We just evaluate the final surface. The average length we got was 1134.304 mm. The model we decided to use was a fixed model crystal width. The crystal width obtained is:

$$Pitch_{horizontal} = \frac{1134.304}{33} = 34.373mm \qquad (4.5)$$

This value can be used as the horizontal pitch for the mechanical design. About the deviation from this value the same effect of the crystal tower showed up. Close to the side used to align the crystals, we obtained a major size. We decided to use this value as possible maximum error:

$$\delta_{lean} = \pm0.939mm \qquad (4.6)$$
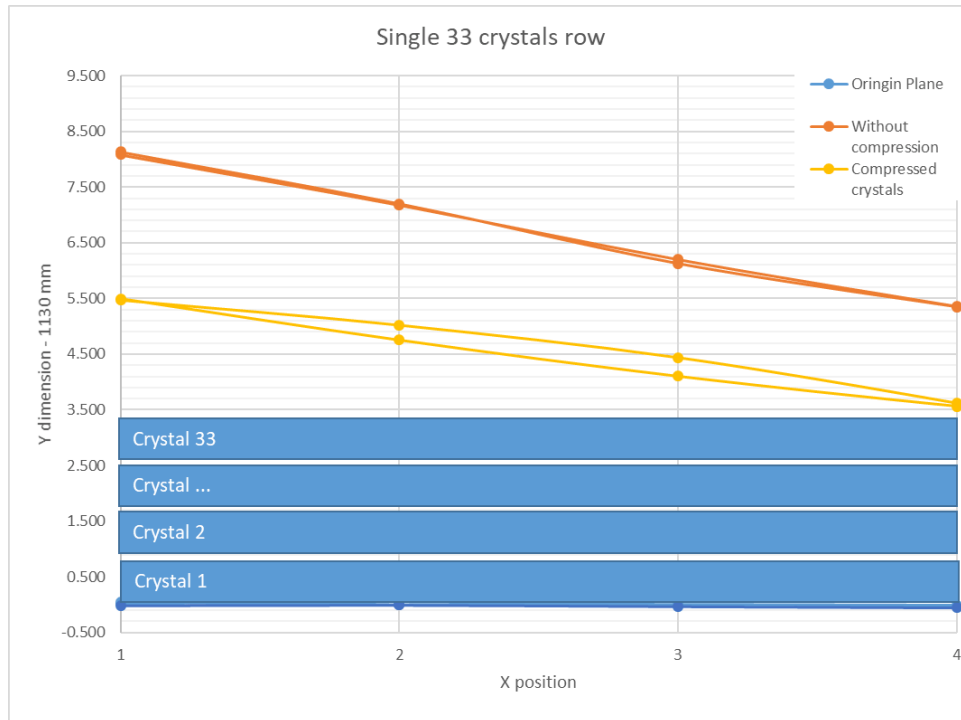
Figure 4.18: Row crystal measurements.

4.2.5 General results

In conclusion, the quantities calculated with this measurement and helpful for the further design of the calorimeter disks are:

- $Pitch_{vertical} = 34.360mm$

- $error_{vertical} = \pm0.303mm$

- $Pitch_{horizontal} = 34.373mm$

- $error_{horizontal} = \pm0.939mm$

The crystal position can be evaluated with the Average of maximum model. Crystals will be divided into groups depending on their height (which is the most critical side). Correction will be done only if greater than 50 μm.

4.2.6 Tedlar correction

These tests have been performed before the decision to add Tedlar between crystals to block cross talking light. This means the previous results need to be corrected with the addition of the Tedlar sheet thickness. Of course a new measurement test would be precious in order to have a more precise result, but because of the urgency of the external aluminum disk machining, it was not possible.
To measure Tedlar, 23 sheets of this material have been packed together and measured in 8 different points randomly chosen. The obtained measurements were:

$$Avg_{23} = 1.156mm; RMS_{23} = 6.18\mu m; \tag{4.7}$$

It means the Tedlar sheets measures: $t_{Tedlar} = 0.050 \pm 0.002mm$.
If we would like to barely correct the obtained data with the Tedlar thickness without any correction, the calculated quantities will be:

- $Pitch_{vertical} = 34.410mm$

- $Pitch_{horizontal} = 34.423mm$

4.2.7 Tolerances consideration

The pitch values shown above represent the average centers used for the preparation of the SIPM holder windows on the FEE disk. The width and precision of such windows depends on the interference with the SiPM holders and it is treated elsewhere. Due to the large spread in the vertical and horizontal position of the crystal stack, the tolerance we assign to the preparation of the windows is somehow relaxed. We used as guideline that the tolerance should not contribute for more than 20% of the maximum variation of the stacking error. The largest stacking error is in the horizontal and corresponds to $\pm 939 \mu m$. Assuming to distribute the holes symmetrically around the vertical axis this get reduced to $\pm 470 \mu m$, 20% of this number is 94 μm. We round this number to 100 μm that we assign as tolerance for the production of the disk windows. Summarizing, for the aluminum ring, the inner step structure and the backplate manufacturing the following values have been used:

- $Pitch_{vertical} = 34.410mm$

- $error_{vertical} = \pm 0.100mm$

- $Pitch_{horizontal} = 34.423mm$

- $error_{horizontal} = \pm 0.100mm$

Chapter 5

Humidity effects on light transmission: development of a measuring system for assessment of optical degradation and preliminary tests

The sensitive part of the electromagnetic calorimeter is the scintillating material, in this case the pure undoped Cesium Iodide crystals. The required optical performance of the crystal and the design of the readout electronics are tightly dependent on the calorimeter physics goal within the experiment. Many studies have been performed in the past on the characteristics of CsI crystal used in calorimeters, such as CLEO II, where the calorimeter was of 7800 thallium-doped Cesium Iodide [41], or kTeV experiment [42], [43] where undoped CsI were used. But the analysis efforts have been focused on the scintillating, radiation hardness and physical properties. A crucial point, not always extensively considered, is the management of the crystals from the end of production to the final arrangement in a safe environment. For the need of the Mu2e calorimeter construction, crystals have been kept as much as possible in low moisture environment (<40%RH) during manipulation process, such as measuring and wrapping. For the stacking time they have been kept into nitrogen fluxed cabinets with almost no humidity inside (<10%RH) (Figure 5.1).

There is a lack of literature about the hygroscopic effect on CsI crystals. The most relevant information we have is the guidelines provided by the manufacturing companies concerning the maximum level of RH% they could be safely exposed to for a long time, without any characterization about the correlation between exposure to humidity, time and damage. What the experience has taught us is that the CsI crystals become opaquer with time, if left in an humidity uncontrolled environment. Moreover, it is important to check if: (a) the crystal degradation process by the moisture absorption is a reversible process or (b) if after an exposure to a dry and hot environment, crystal transmittance can be recovered, in other words if the degradation is just a matter of the amount of water absorbed by the crystal, or if it depends on some sort of irreversible chemical reaction or structural variation.

Because of the lack of information on the effect of the humidity on the CsI crystal properties, there was also a lack of literature on how to evaluate the humidity induced damage. For these reasons, the first steps have been moved to understand how to create a reproducible set up to evaluate the effect on the transmittance on the crystals. It is indeed very important to reduce the variables as much as possible,

Figure 5.1: CsI crystals which have been tested for geometry and optical properties. They are placed into nitrogen fluxed cabinet waiting to be installed inside the calorimeter disk.

to be sure to have (or not) a direct correlation between transmittance and humidity exposure.

This first stage was characterized by the evaluation of the information we got from the manufacturers and from the experience to manage the calorimeter pre-production samples, with lots of brainstorming which brought to a set-up and a method to evaluate the transmittance-humidity correlation. In this chapter the evolution of this set up is presented, with a detailed descriptions of the intermediate steps made to arrive at the final configuration. Further the first tests performed are presented.

5.1   Experimental set up

The experimental apparatus has been implemented at the Interdepartmental Crystal Research & Analysis Center (ICRYS) [44] of Università Politecnica delle Marche. Several versions of the apparatus have been developed over time to refine and tune properly each parameter converging to a reliable and confident measurement system. Even if the upgrades changed some features of the experimental set up, the general structure remained the same:

- a climatic chamber - Challenge 250 (ACS), 224 l with independent regulation of relative humidity (RH%) (from 10% to 98%, precision of 3%) and temperature (T) (from 10°C to 98°C, precision of 0.3°C) - obscured to be light tight, where the crystal and part of instrumentation are placed in;
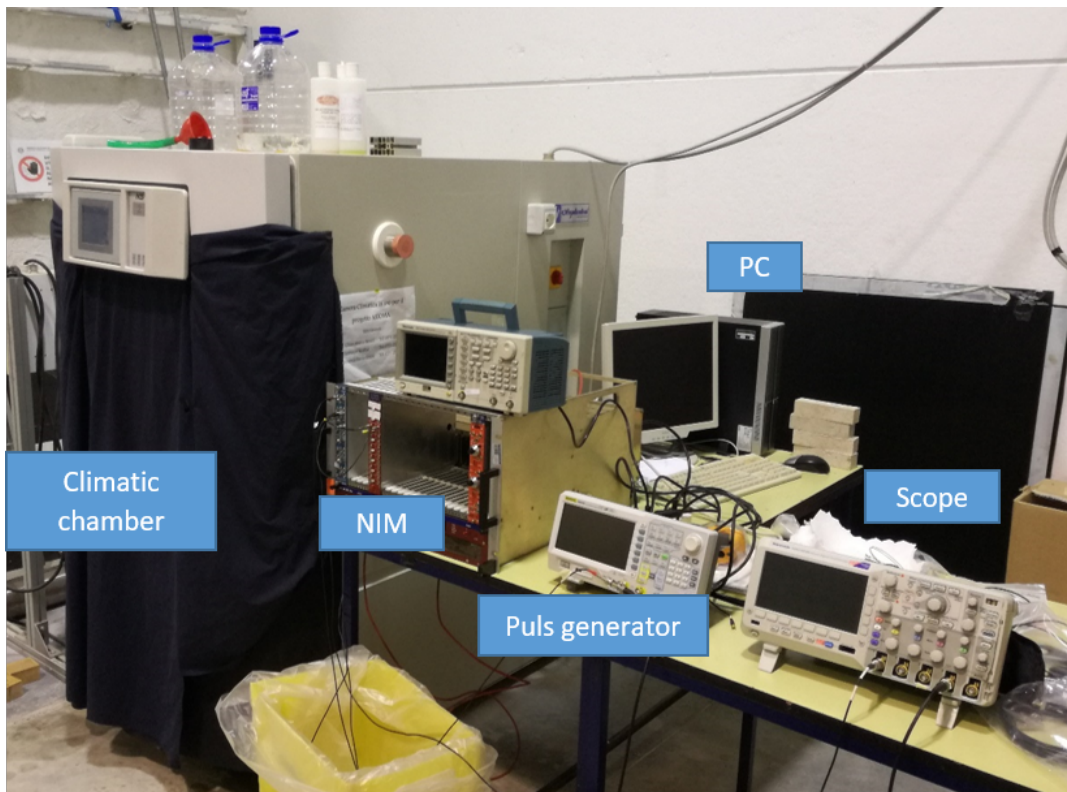
Figure 5.2: Experimental set up at the Università Politecnica delle Marche. It is possible to see the climatic chamber, the NIM unit, the pulse generator and the scope, with the PC as DAQ unit.

- a pulse generator - Tektronix AFG3101 - which generates a square pulse to power up a LED;

- a mechanical structure to keep all the components relatively fixed;

- an UV LED with a frequency of 365 nm, 1 mW power as light generator;

- a light detector (different for the various versions);

- a scope for reading signals generated from the light detector

- a PC for data acquisition and for control and monitor of the climatic chamber and pulse generator, with Windows OS on it, and a LabView software to manage all the tasks.

The goal of this set up is to evaluate the light transmission variation while controlling the humidity level and the temperature. The LED emits light which is transmitted through one of the Mu2e calorimeter crystals (the same used for the Mu2e Calorimeter [40]), wrapped with Tywek, and the light detector evaluate the amount of light transmitted. In this way we are able to monitor if the level of light, and thus the transmittance of the crystal has changed over different ambient condition exposure.

5.1.1 First version - PMT

In the first version of the measurement system, a phototube was used to read the light transmitted through the crystal, facing the small uncovered face, with the LED,
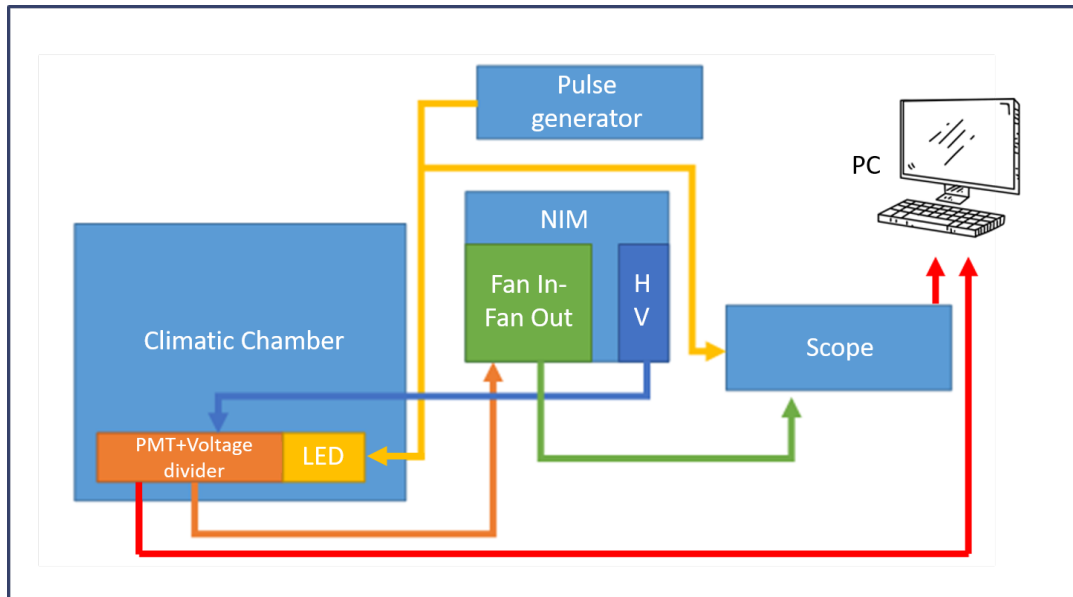
Figure 5.3: Block diagram of the first version set up. The pulse generator sends pulses to both LED and scope for triggering, the HV module in the NIM crate supplies the adequate high voltage to the Photo-Multiplier Tube which send signals to the Fan-in Fan-out module. The decoupled signal is then sent to the scope for the readout and data storage operations.

the crystal and the phototube on the same axis. A 3D printed structure has been developed to keep everything in position, and to shield the HV power supply connections at the VD. The crystal is supported by two small ABS steps which covers a very small crystal surface to keep as much surface as possible exposed to the circulating air flow (Figure 5.2, Figure 5.3, Figure 5.4).

To let the phototube and the voltage divider work properly, a NIM crate with a high voltage board has been used, to supply the 1460V needed. The pulse generator has been set up to 100kHz of frequency with a high level of 5V to power the LED up. The Climatic chamber has been regulated directly with his software (Angelantoni software) while the data recording has been performed with a LabView custom software.

The problem with this set up was the system reliability. There was only one readout system, and it was not possible to understand the source of signal variation in case of anomaly of some of the component. In order to do this a second version was designed.

5.1.2 Second version - SiPMs

To have some sort of signal redundancy, we added a second reading system. Because of availability, a second system made with another PMT and VD was not possible. Moreover, such system would be excessively big in size and it would not fit anymore in the climatic chamber. The SiPMs have been chosen as readout sensor substitutes. The reasons are the very compact size of these sensors and theis wide availability because they are the same used for the calorimeter, and many spare components are available for different other tests.
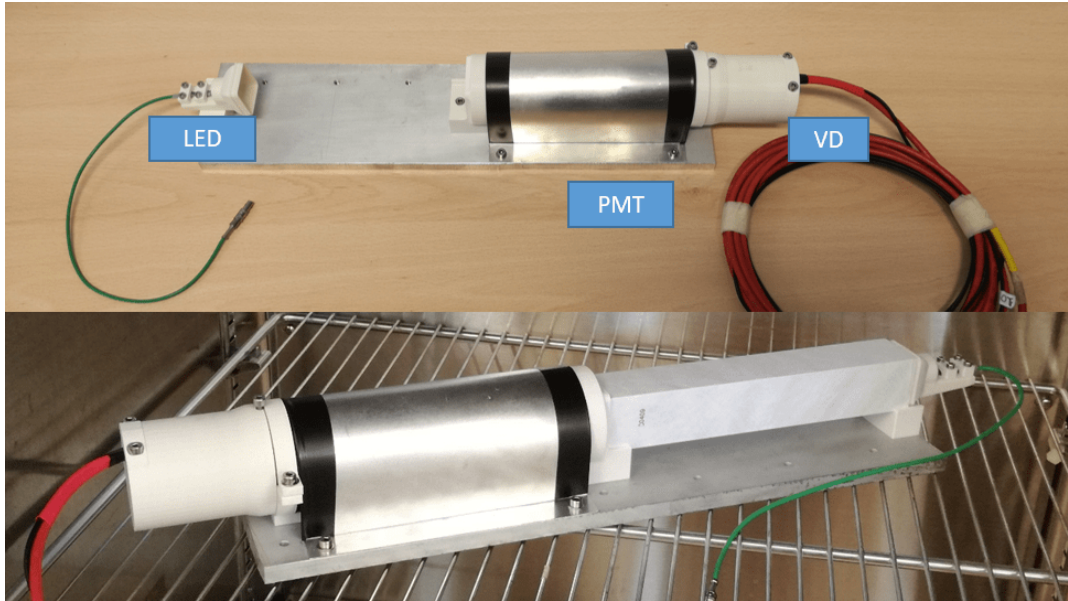
Figure 5.4: Mechanical structure of first set up without a crystal (top) and with a wrapped crystal (bottom). The PMT is protected with an aluminum plate to avoid accidental damage.

The arrangement was approximately the same, with a SiPM placed at one end of the crystal, but a second SiPM was inserted near the LED, in order to measure light emitted from the LED before any interaction with the crystal (Figure 5.5). Because of the bigger amount of light that such SiPM would have collected, with respect to the other one, it has been placed leaned in order to get a less amount of light, but still proportional to the light emitted from the LED (Figure 5.6). Moreover, each Mu2e SiPM has two independent channels to be readout, thus adding redundancy to the system. The high voltage (1460V) was no more necessary, but a 64V power supply for the SiPM was implemented, and a simple electronic circuit was built for the SiPM readout. At this stage, an amplification was not needed since the produced light could be tuned to get a clean signal. The electrical circuit is shown in Figure 5.7. The disadvantage of this design was that the leaning of the reference SiPM was fixed, therefore it was not possible to adjust the light amount for both SiPMs. This translated in a non-linearity of the SiPM response i.e. its gain would decrease for increasing the input light Figure 5.8. A correction of this factor was performed and taken into account, but in order to have a more precise set up we developed a third version, very similar to the one described in the following section.

5.1.3 Third version - SiPMs with splitter

For the third version we upgraded mechanics and electronics, without changing the working scheme of the set-up, or the devices used, continuing to use SiPMs as readout sensor and the same LED as light source (Figure 5.9). The new parts consisted in a crystal optical splitter cube with a 30%-70% splitting ratio placed just after the LED, in order to have a good proportion of light between the Signal SiPM and the reference monitor SiPM. In this way the peak of the signal read from the two sensors has approximately the same starting value, and it was possible to set the amount of light of the LED to let the SiPMs work in the linearity region, i.e. $V = G \cdot photons$
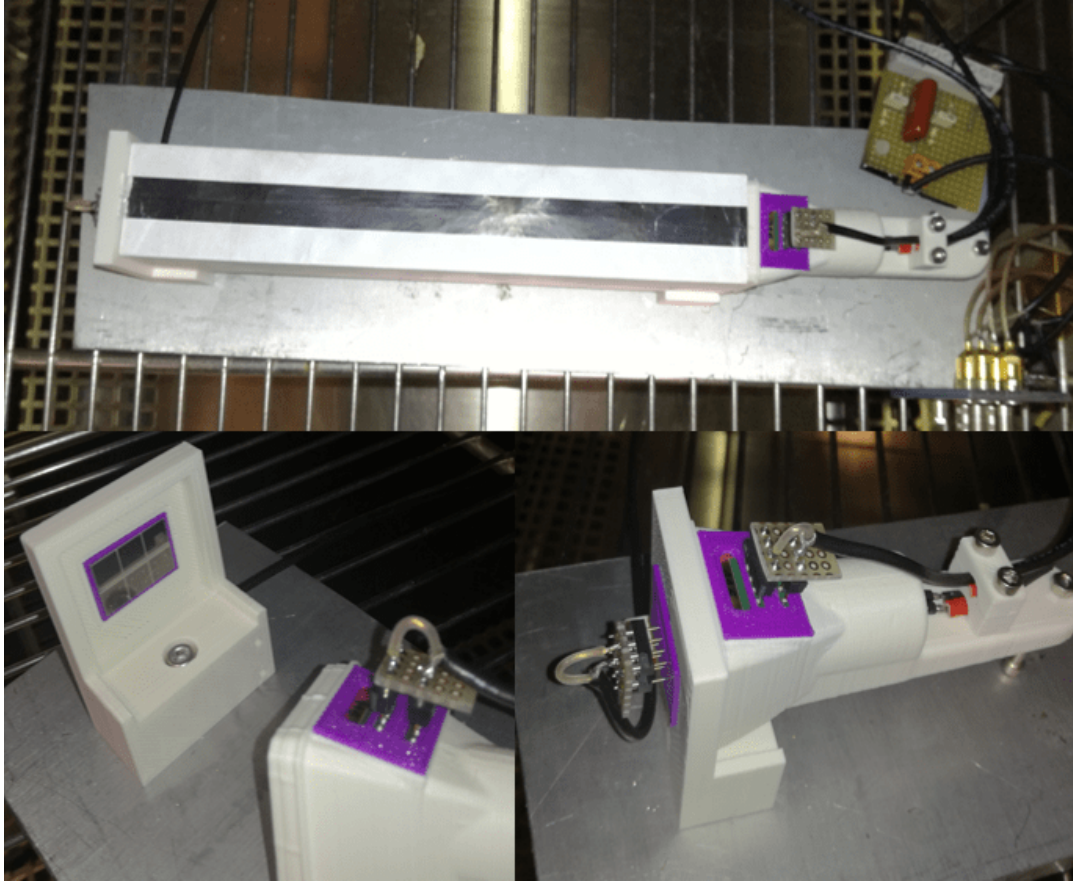
Figure 5.5: Pictures of the version 2 set up. It is possible to see SiPMs in position.

where G does not depend on the number of photons. In Figure 5.10 (bottom) the ratio between the two signals is shown as a function of the emitted light (by varying the LED PS voltage):

Another upgrade which I made was to implement an amplification board for the supply of the LED, to avoid the pulse generator supply directly connected to the LED. This was done to avoid the pulse generator to supply current for the long time needed for the tests, since it was not designed for this purpose. The amplification board is based on a LM7171BIN/NOPB (operational amplifier), with an amplification factor set up to 2. To supply this board a small power supply unit with a $\pm 12V$ output and 2A max current output was used.

A new board was also added to regulate independently up to four channels high voltage power supply ($\approx 54V$); in this way we were able to use one power supply at 60V and regulate four different sub-power supply lines to the four cells used in the set up. Thus, we could set up the proper $V_{Breakdown}$ for each cell easily. All the electronic components were placed inside the climatic chamber, to be sure to keep under control their working temperature environment, and to calibrate set up for those conditions. At the same time, a more robust mechanical support structure was implemented to take the SiPM in a reference and stable position with respect to the crystal (Figure 5.11).
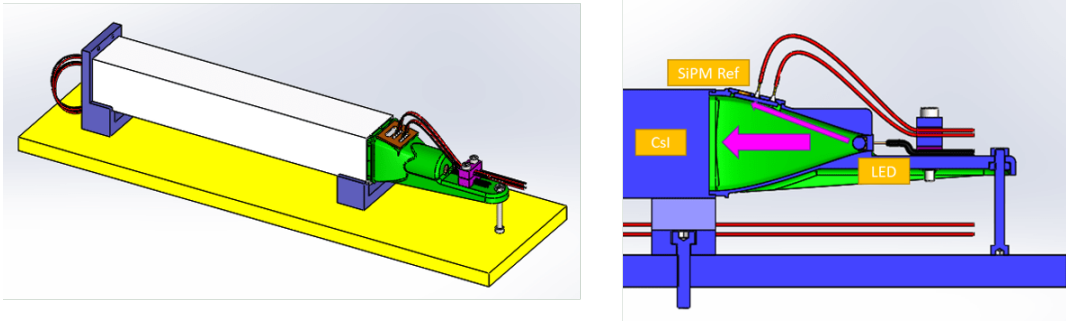
Figure 5.6: CAD model of the second version set up (left). Section view of the set up showing the light path from the LED (right).
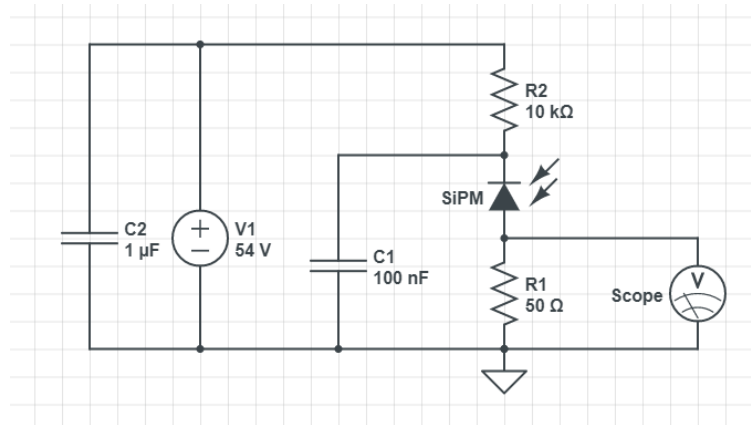
Figure 5.7: Electronic scheme of the circuit built for SiPM readout.

5.2   Data acquisition and post processing

Every time data are acquired, 20 pulses are saved in a file (Figure 5.12) named with a date and a time reference, in order to relate it with the log data of the climatic chamber, and synchronize temperature and relative humidity in the same file. The trigger time is set by the user through the LabView program (Figure 5.13). After that the excel program calculates the 20 pulses average (Figure 5.14), next the following parameters are evaluated:

- t_{peak} [s] time when the peak happened;

- $t_{PED}^i = t_0$ [s] time when PED is starting;

- $\Delta_{PED} = 300ns$ PED elapsed time. It is set by the user;

- $PED = \dfrac{\int_{t_{PED}^i}^{t_{PED}^i + \Delta_{PED}} S^*(t)\, dt}{\Delta_{PED}}$ [V] average value of the signal when there is no light. S(t) is the signal value for time;

- $S = S^* - PED$ [V] signal offset with the background tension;

- $t_{Gate}^i = t_{peak} - 35ns$ [s] starting Gate time. 10 ns are set by the user;

- $\Delta_{Gate} = 350ns$ Gate duration. It is set by the user;
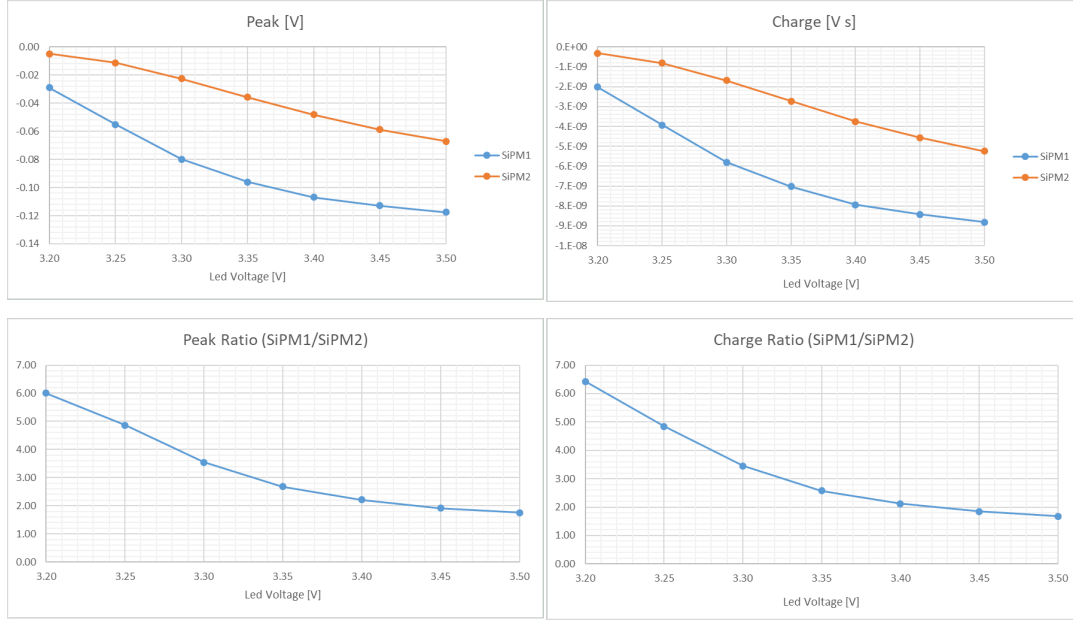
Figure 5.8: Variation of the acquired light in function of the Led voltage power supply, proportional to the amount of light emitted, for the signal SiPM (1) and the reference SiPM (2) (top). The ratio of the two SiPM signals: if there was no dependency from the light, the ratio would be a straight line (bottom).

- $Q = \dfrac{\int_{t^i_{Gate}}^{t^i_{Gate}+\Delta_{Gate}} S(t)\,dt}{R}$ $[V]$ Charge generated from SiPM when light pulse was sent. A value of R=50Ω is used;

- $t^i_{Tail} = 900ns$ Time when tail begins. It is set by the user;

- $\Delta_{Tail} = 100ns$ Tail elapsed time. It is set by the user;

- $Q = \dfrac{\int_{t^i_{Tail}}^{t^i_{Tail}+\Delta_{Tail}} S(t)\,dt}{R}$ $[V]$ Charge generated from SiPM when light is off. It should be close to 0.

This evaluation is performed for both SiPMs. For the data analysis peak and charge values are used to evaluate the crystal performance, singularly or the two SiPM ratio. RMSs and Tail charge values are stored and checked to understand if any anomaly happens during data acquisition.

5.3   Set up calibration

After the set-up has been mounted and properly connected, it requires a calibration procedure. First of all the $V_{Breakdown}$ voltage must be set up at the required value for each cell of each SiPMs, as indicated from the Hamamatsu manufacturer datasheet; next an adequate level of voltage must be set up for the LED, to let the SiPM work in a linear range as described in subsection 2.2.2, this means approximately one twentieth of the maximum number of SiPM pixels. In the final setup, a value of LED PS of 6.7V has been set up and it generates a very clear and distinguishable signal.
The next step has been to evaluate how much the set-up is stable and how it behaves
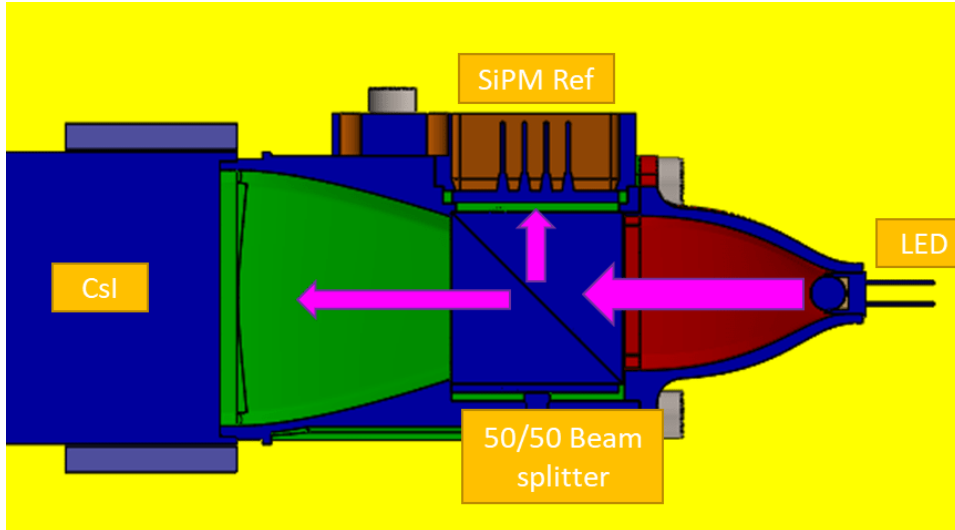
Figure 5.9: CAD model of the third version set up. In this section view the light path from the LED through the splitter cube is shown.

for changing conditions. In particular, it is important to see how the SiPM response will change for temperature fluctuation and for different levels of relative humidity, because we are going to change significantly the relative humidity level and we need to separate the signal variation from the set-up behavior to crystal degradation. For what concerns the temperature, we are not going to change it during measure, but we need to know to have a better estimation of the measurement error, because the climatic chamber has a stability of $\pm 1°C$ during measurements.

In order to do that, the readout SiPM has been exposed directly to the light source, without the crystals between, and in this configuration a thermal cycle and a relative humidity cycle have been performed. Any variation is thus just set-up responsibility, and we can correct for this effect in the acquisition with the crystal.

The Figure 5.15 shows the signal produced by the readout SiPM, superimposed on the temperature cycle, where the time is presented on the X-axis, 1A and 1B are the two readout SiPM cells, and Ref is the reference SiPM cell. From this graph we can understand how the signal is influenced from the temperature level in steady conditions. In Figure 5.16 the correlation between readout SiPM signal and temperature is presented. From these values it is possible extract a linear correlation between temperature and peaks and peak ratios:

$$Peak1A[V] = -0.0091\Delta T[°C] + 0.0328 \tag{5.1}$$

$$Peak2A[V] = -0.0074\Delta T[°C] + 0.0296 \tag{5.2}$$

$$PeakRef[V] = -0.0089\Delta T[°C] + 0.0125 \tag{5.3}$$

$$Peak1A/Ref = 0.0043\Delta T[°C] - 0.8115 \tag{5.4}$$

$$Peak1B/Ref = 0.0044\Delta T[°C] - 0.6232 \tag{5.5}$$

Considering a temperature fluctuation of $\pm 1°C$, the peak temperature stability is better than 0.009V. This error refers to a steady state condition, while the temperature fluctuation is usually very fast (of the order of seconds) and only depends on the chamber control unit. This means that the real temperature signal fluctuation will
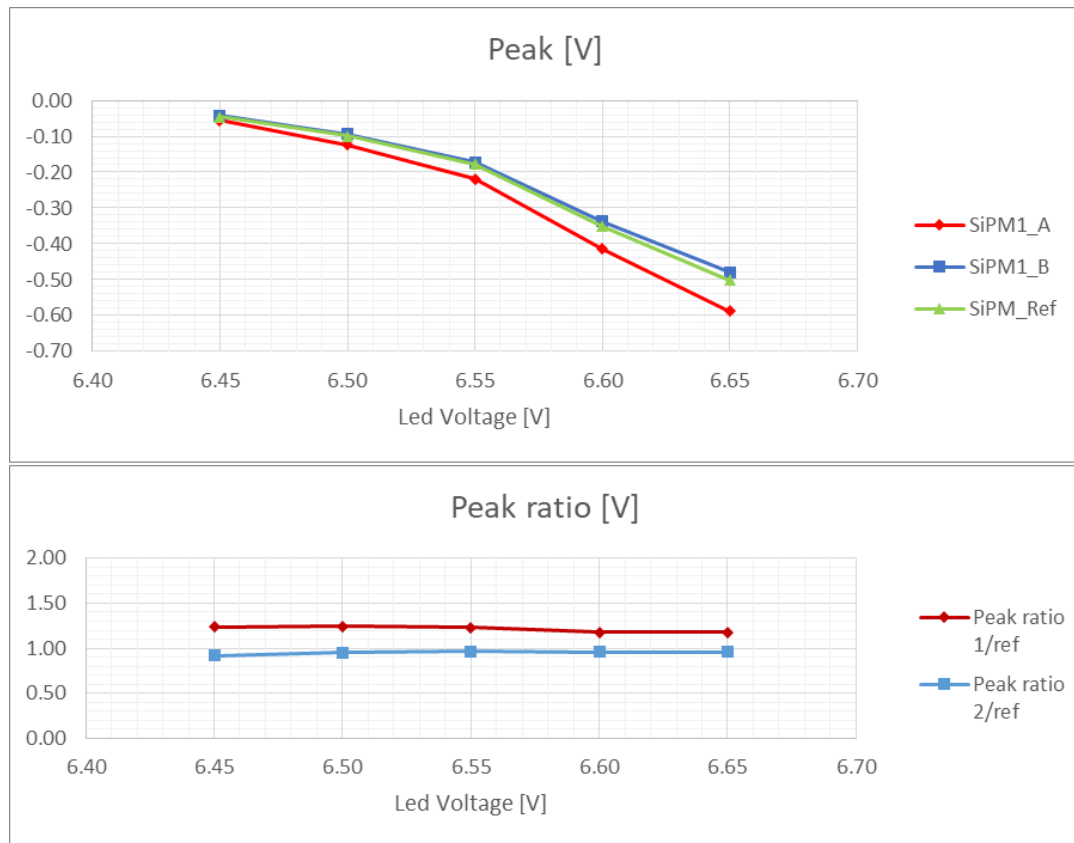
Figure 5.10: Variation of the acquired light as a function of the Led voltage power supply, proportional to the amount of light emitted, for the two cells of the signal SiPM (1) and (2) and the reference SiPM (ref) (top). The ratio of the two SiPM signals: the ratio this time is approximately constant, for both cells of the readout SiPM (bottom).

be smaller than this estimate because of the chamber temperature precision, which is $0.3°C$, the maximum signal resolution is 0.003V for the peak. Considering ratios, for the temperature precision, the maximum error is approx 0.001, that means the temperature ratio error is below 1%. For the relative humidity calibration, the same procedure has been performed. In Figure 5.17 the results are reported for the peak and the charge. As the figure shows, no significant change is due to the humidity level.

5.4 Performed measurements and results

5.4.1 Humidity tests

At this point some tests have been performed. A Mu2e production crystal is properly wrapped with Tywek and placed in the setup. Before this operation, each crystal has been kept sealed in waterproof plastic bags, with silica gel and evacuated for long time storage. After this preparation period, the crystal is quickly inserted inside the climatic chamber, where a $30°C$, 10%RH environment has been already prepared. After one day of exposure to those steady conditions, the relative humidity has risen up to 80% for 6 days, and then lowered down back to 10%. During this time signals
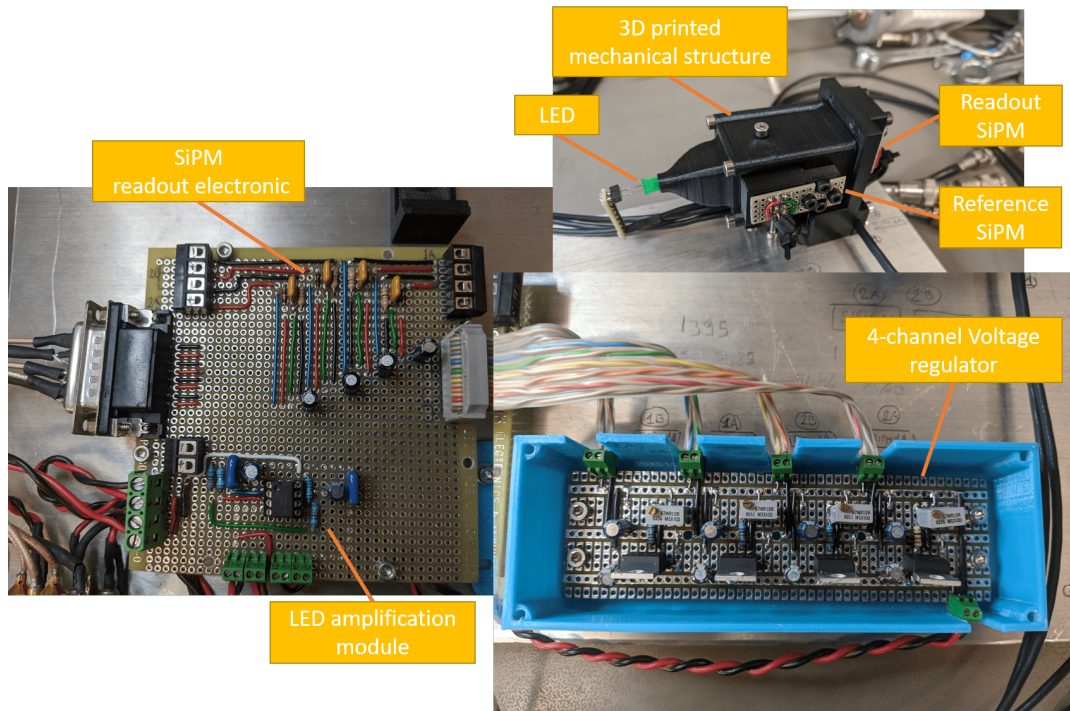
Figure 5.11: In this mosaic image all the main components of the third version have been shown. The readout and reference SiPMs are coupled together for calibration purposes and the crystal is thus missing in this working configuration.

have been constantly recorded, with a frequency of one every 10 minutes.

In Figure 5.18 we can see what happened to the crystal C409. If we look at the peak value of readout SiPM, we can observe it is rising up, apparently. But if we look at the Figure 5.19, we can notice the ratio readout/reference is decreasing, of less than 3%. We can interpret this as the amount of light produced increased[1] but the transmittance of the crystal worsened, due to the humidity increase. Of course it is a very small decrease of transmittance and considering the level of humidity exposure and the amount of time, these tests give us the information that the manipulation of several hours in not very well humidity controlled environment should not be a problem. Moreover, it implies which test much longer are required in order to get a good characterization of humidity damage. At the moment of writing this Thesis, other tests have been planned, with an elapsed time of one month in order to observe a curve that can be mathematically expressed.

5.4.2   Temperature tests

Another kind of test performed with the same experimental setup, was the baking of a crystal. We have taken crystals which had been previously exposed to high humidity level for several cycles and time, and we have kept the crystal to a dry hot environment for several hours, to check if any increase of transmittance would occur. The idea was to evacuate the water absorbed from the CsI and restore or at least

---

[1]The increase of the light emitted was probably due to the environmental changing outside of the chamber, because power supplies and the pulse generator are out of the chamber, or to a degradation of the LED because of the humidity.
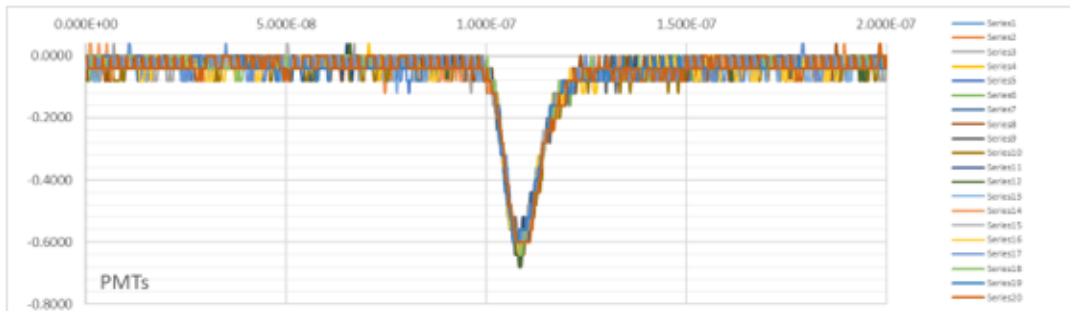
Figure 5.12: This is a sample of signal, composed by 20 pulses registered and acquired from the scope.
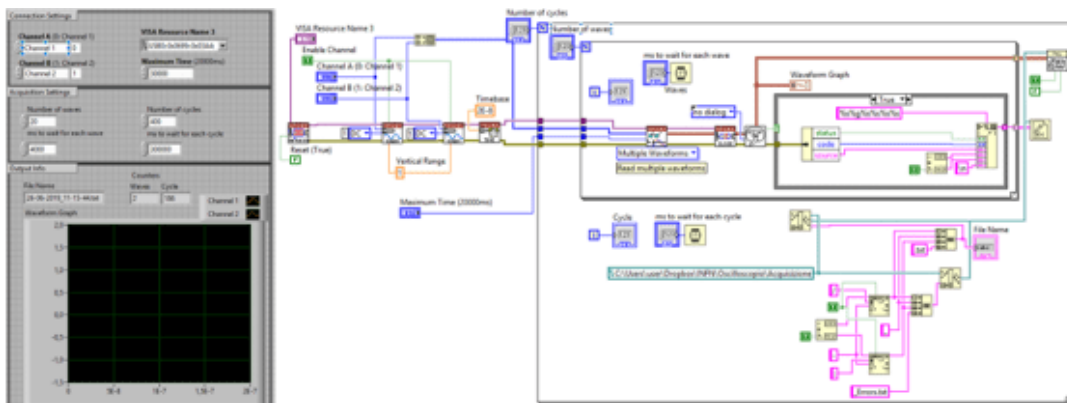

Figure 5.13: Block diagram of LabView DAQ program (right). GUI for the parameters set (left).

increase the transmittance. So we organized a cycle of 12h exposure to 70°C and 10%RH. During this time, the readout equipment was kept off to avoid damage due to the high temperature.

In Figure 5.20 what happened to crystal C409 has been displayed. In the upper graph we can see the peak values for the readout and reference SiPMs, and in the lower graph their ratio is shown. It is observed that the ratio increased of about 5% after the baking procedure. In this case, however, the reference SiPM shows a reduction of the light observed. We assume that this is due to the impact of the HOT cycle on the LED emission.

Other tests have been planned in conjunction with future upgrade that could allow to observe light emission and transmission at high temperature. However, we consider these results to be very encouraging in persisting in a more detailed study to achieve a precise description of these phenomena.
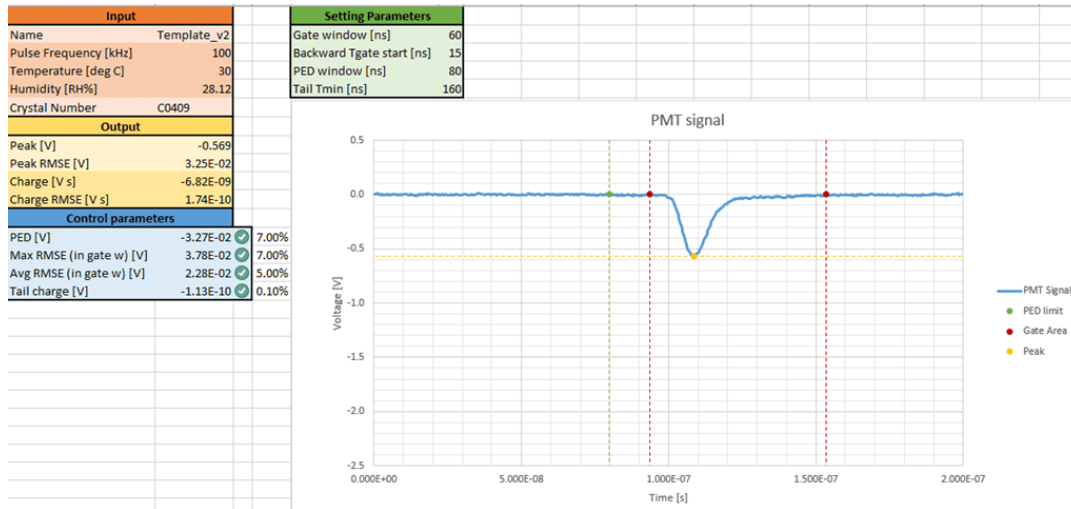
Figure 5.14: Post process signal with Excel datasheet. This signal is the average of 20 pulses. PED and Gate are visible. On the left side it is possible to check the parameters used for this signal and some important evaluation data.
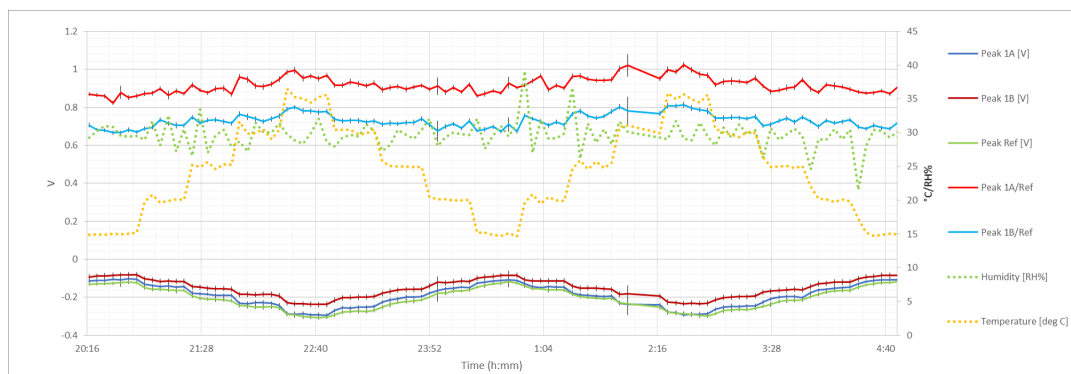
Figure 5.15: Setup behavior for temperature changing. It is possible to see how peaks of the various cells changes over time when temperature changes. Relative humidity is set steady at 30%.
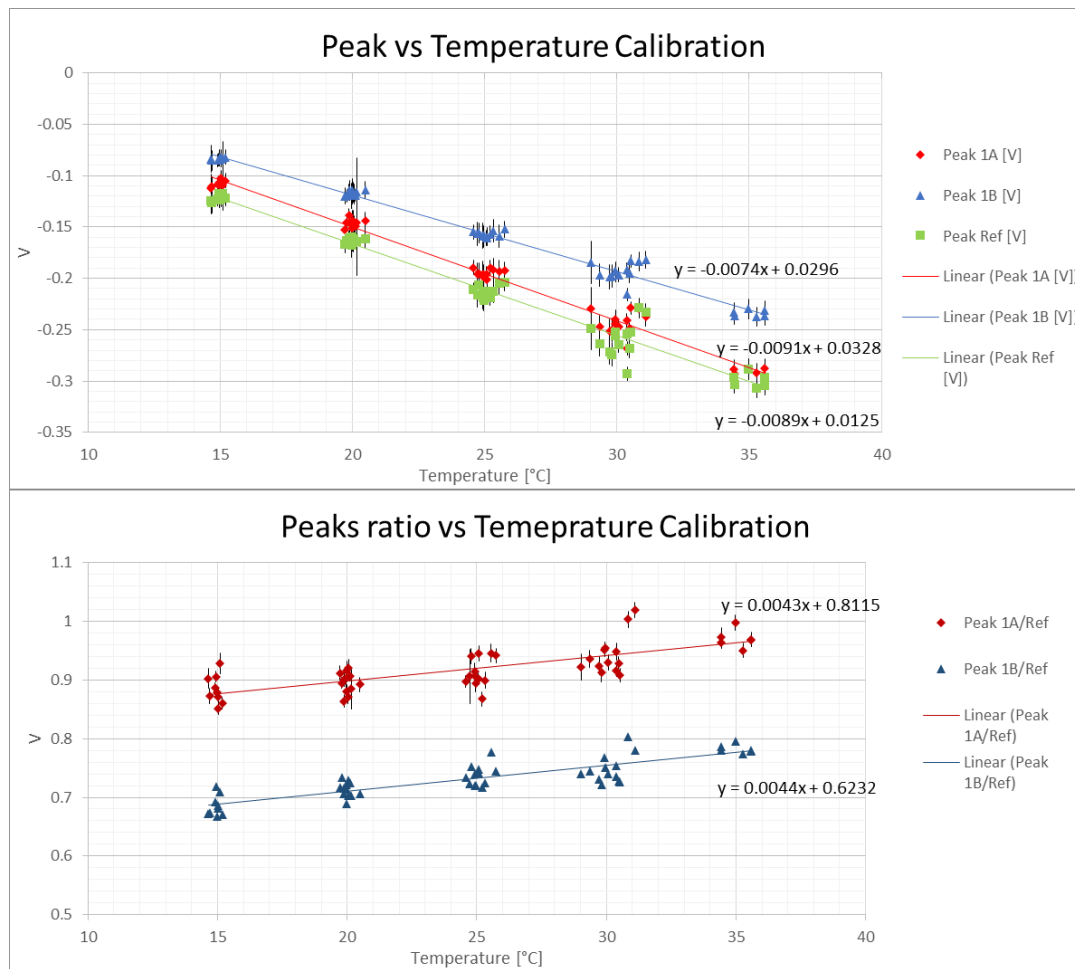
Figure 5.16: Temperature correlation between signal output and temperature; In the top image the single cell peaks are displayed, in the bottom image the ratio is displayed. The behavior is linear but the leaning shows there is a difference in the gain between the readout and the monitor SiPM.
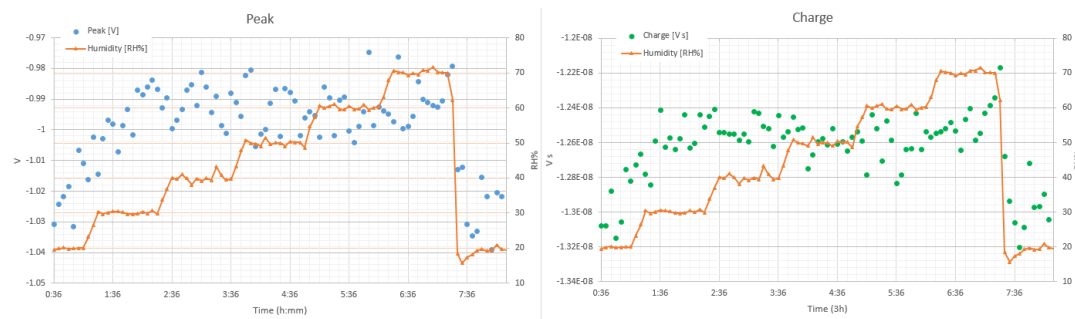
Figure 5.17: Setup behaviour for relative humidity changing. On the left the peak value is displayed, on the right the charge is displayed.
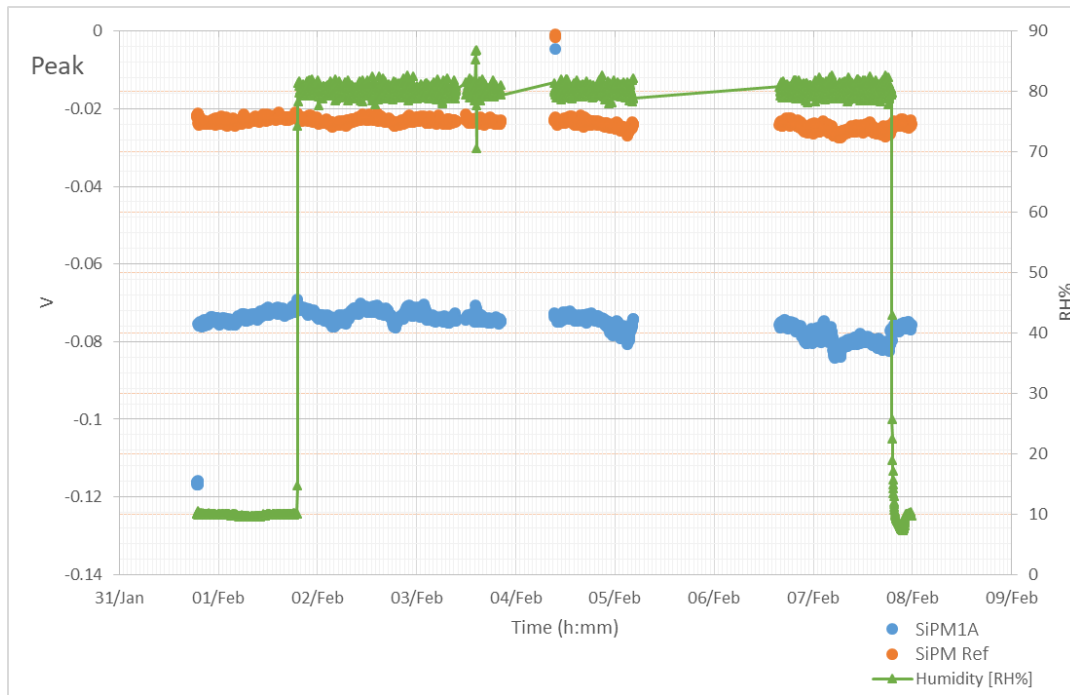
Figure 5.18: Humidity test with crystal C409. The green curve is the recorded humidity level inside the chamber, the blue curve is the readout SiPM peaks and the orange curve is the reference SiPM peaks.
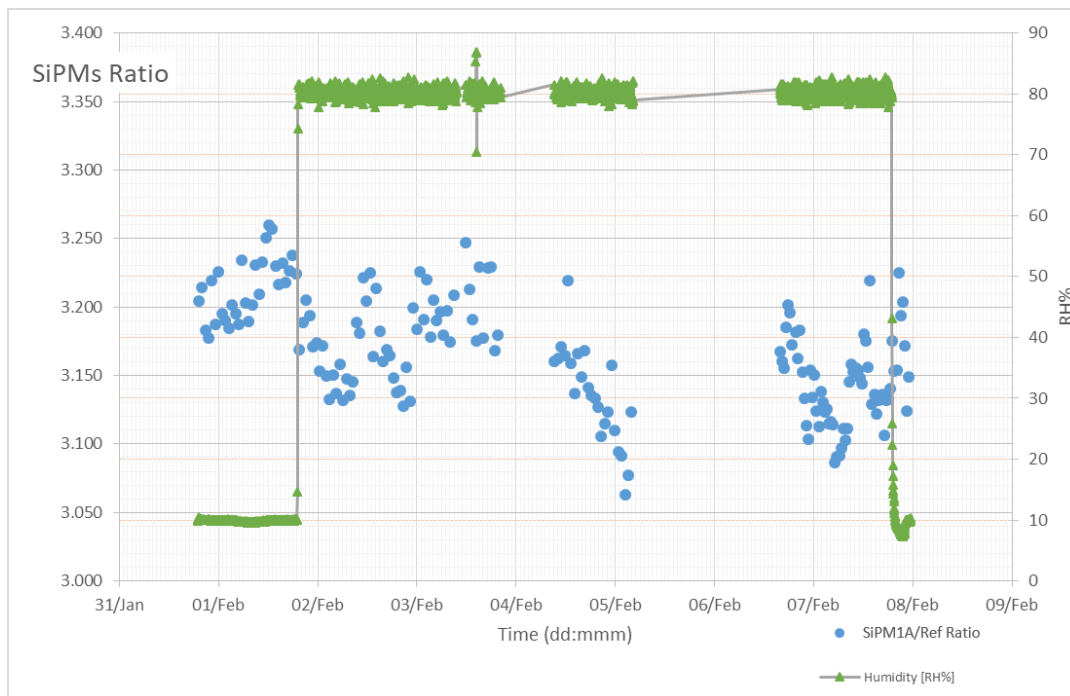
Figure 5.19: Humidity test with crystal C409. The peak ratio is shown.
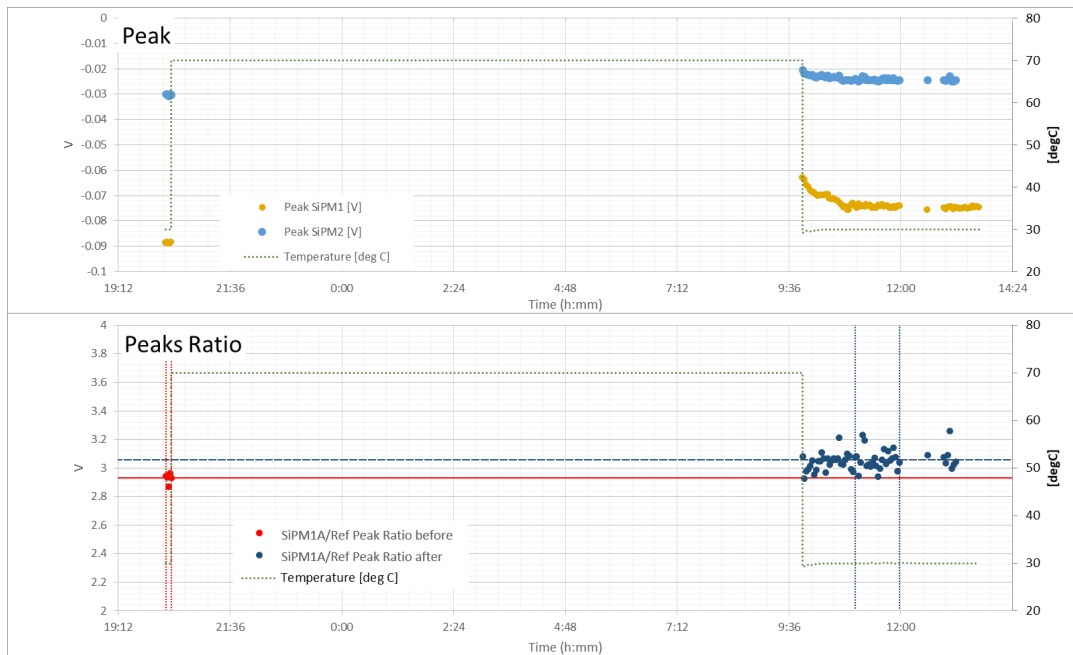
Figure 5.20: Crystal baking test with crystal C409. The green curve is the recorded temperature level inside the chamber, the blue curve is the readout SiPM peaks and the orange curve is the reference SiPM peaks in the upper graph. In the lower graph the ratio is shown. The dotted horizontal lines represent the average of peaks ratios before (red) and after (dark blue) the baking test.

Chapter 6

The Calorimeter inner ring structure design

The Inner Cylinder (IC) is the innermost mechanical structure of the calorimeter disk. Its goal is to support the crystals of the upper half of each disk, thus providing a reference surface for them, and to align the middle height crystals horizontally. It is connected with screws to the Backplane on the back and the Source plate on the front. An exploded view can be seen at Figure 3.1. It will be mounted after that the 7th row of crystals have been properly positioned [45] [46].

In Figure 6.1 the IC main components are shown, they are:

- one carbon fiber cylinder (a);

- two aluminum rings (b);

- three outer ribs (c).

The other components are the centering bushings (the blue items in the figure), some enforcement brackets on the rib structure side, the optical calibration device supports, which are the grey glued blocks in the innermost part, and a thermal pad glued in the inner part too, which will heat that surface for irradiation problems [47].

The inner cylinder design has to satisfy several requirements that are exposed below:

- it has to support the upper crystal matrix, i.e. a load of approximately 1000N;

- the amount of material has to be kept very low, in particular, low atomic number materials need to be used for not interfering with the particle trajectories passing through the inner bore;

- it needs to have very low outgassing properties in order to keep a 10^{-4}Torr vacuum environment;

- materials must be non-magnetic and high radiation resistant, considering the harsh environment where they will reside;

- minimize the mechanical interaction with the Backplane and the Source plate because those components are very delicate and we must assure not to damage them;

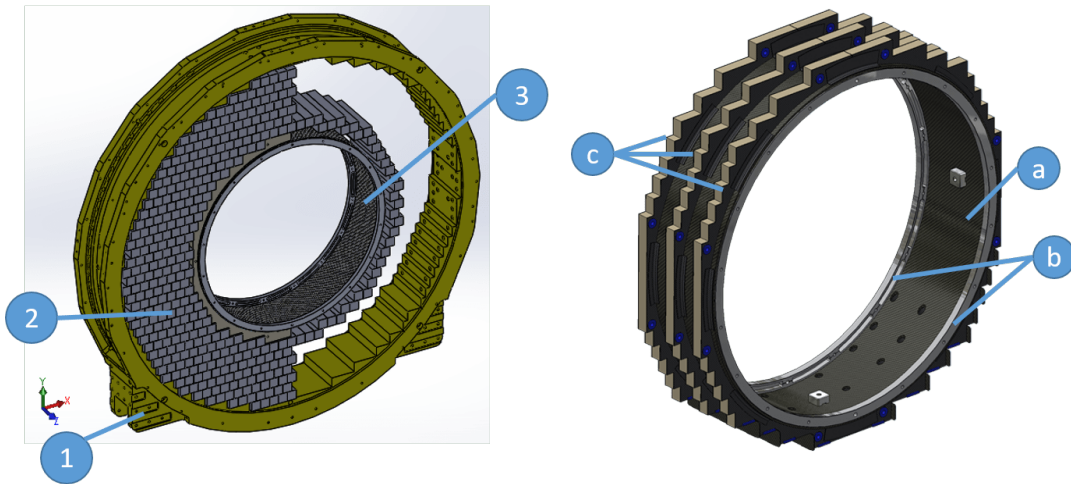- finally we need to be sure that the manufacturing process is feasible and on budget.

Figure 6.1: CAD model of the IC and the crystals. In the left image the aluminum outer ring (1), the crystal matrix (2) and the IC (3) are shown. In the image the right part of the crystal matrix, the Backplane and the Source plate have been suppressed for graphic reasons. In the right image a detailed view of the IC is presented: the carbon fiber cylinder (a), the two aluminum rings (b) and the crystal step structure (c).

The carbon fiber cylinder

The carbon fiber cylinder Figure 6.2 is a cylinder with an inner diameter of 712mm and a thickness of 4.2mm, made of $F - .220/193/50$ carbon fiber fabric with a cyanate ester resin. It is composed of 18 fabric plies $0° - 90°$ symmetric and balanced disposed. It has been designed to connect the two aluminum rings and to support surface for the step structure, minimizing the amount of employed material. This component has been already realized in a number of three units (one for spare) from CETMA [48] which is the firm in charge of the realization of the IC and the Source plane.

The aluminum rings

The aluminum rings are made of milled 5083 H111 aluminum alloy. They have an inner diameter of 672mm, an outer diameter of 712mm and a thickness of 13mm. They are the element which gives stiffness to the whole IC assembly. They are 42 times stiffer than the CF cylinder, so they will sustain the majority of the load. They present some milled shots to reduce the amount of material without compromising the stiffness, a couple of reference holes for the alignment and tapered holes for fastening with the Backplane and Source plane. They will be glued on the CF cylinder and they are now under fabrication.

The rib structure & steps

The rib structure required very long time to be designed. Several proposals have been made, to balance physical requirements, budget and feasibility. The first proposal was to create a very stiff structure, made of solid CF skin, filled with an aluminum sponge. It was rejected for the high risk of outgassing and creation of virtual
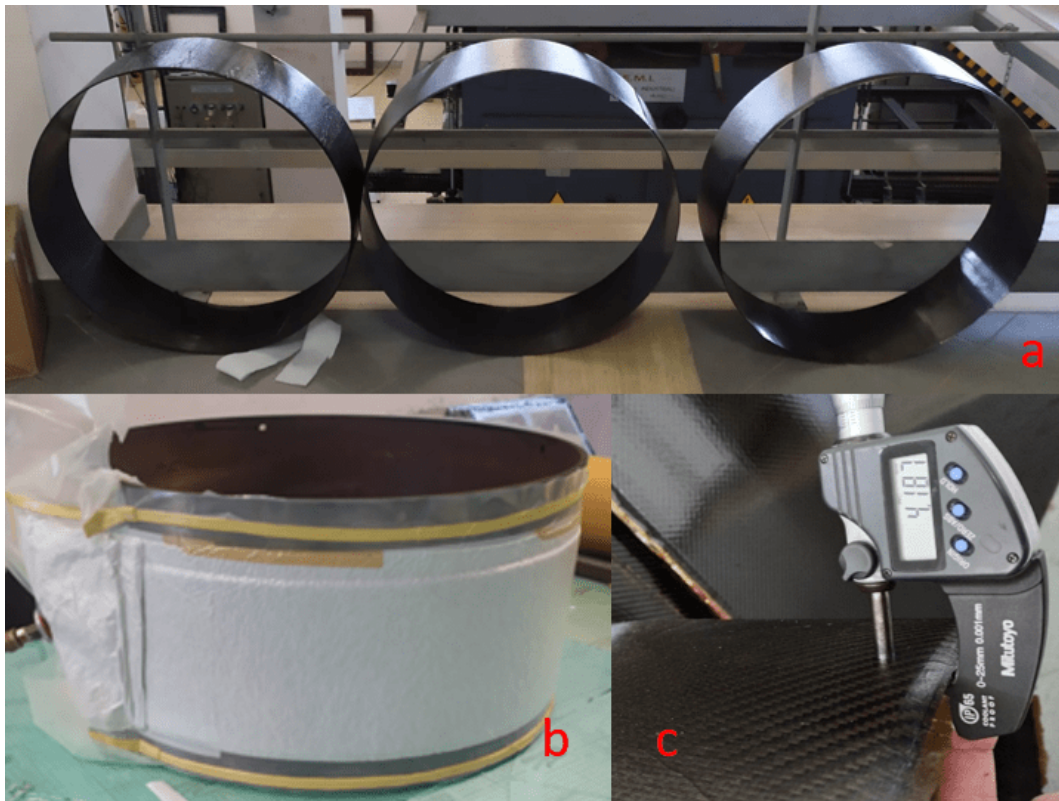
Figure 6.2: The three realized carbon fiber cylinders (a). The CF cylinder during forming with a vacuum bag (b). Measuring test of the CF cylinder (c).

leak spots for the aluminum gluing process and for the complex manufacturing process required. The second proposal was to use a milled Zedex structure. Zedex is a material like PEEK, for the outgassing properties and machinability, but with a lower thermal resistance and cost. This possibility was not carried out due to the not-availability of plates of the required dimensions, and for the excessive cost. The third and last proposal was to make ribs with a sandwich made of aluminum grooved honeycomb, with CF layers on the two sides, and create the crystal contact surface, with CF layers, to be glued in position in a second stage (Figure 6.3). This solution was approved from CETMA and was highly analyzed and sized properly, with my personal contribution, as shown below.

6.1 Calorimeter Inner Ring models

The hard part in the IC design was the choice of the right model to mimic the whole structure. There are too many components and too many mechanical interactions to model all the components in detail, so a simplified model was necessary.
The first step was to identify the loads on the IC, that however has a strong dependence on how the crystals will be assembled. In Figure 6.4 the crystal matrix contact scheme is represented. Crystals directly above the IC must lay down and load directly on the IC, with a total vertical force of approx. 1240N, represented with the red arrows in the image. At the same time crystals directly beneath the IC must support the crystal load; this reaction is represented with the blue arrows. But the constraint
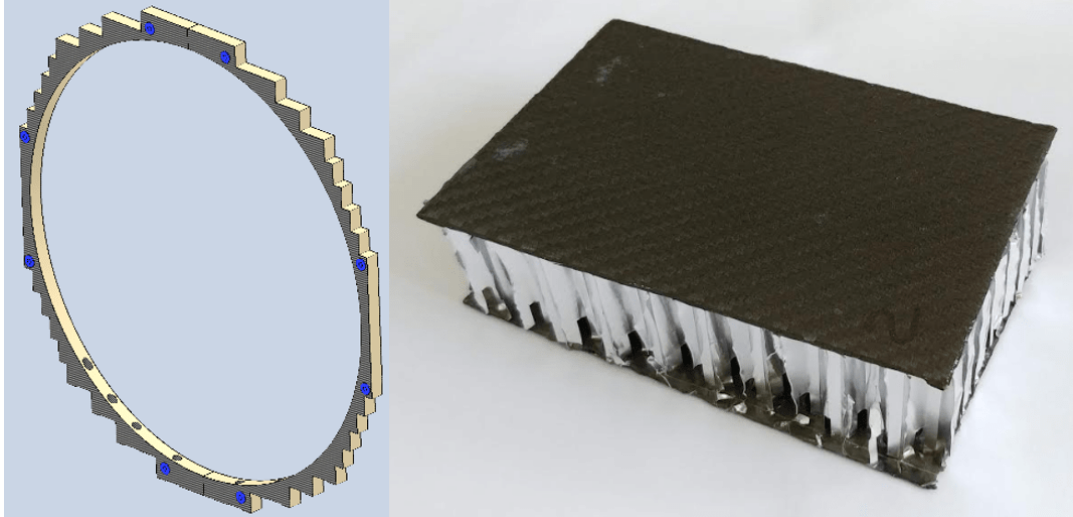
Figure 6.3: CAD model of one of the three ribs (left). A sample of the
CF and Al honeycomb sandwich used for the ribs (right).

cannot hold the IC in position, i.e. the IC can lift from that contact surface if its way
to deform can admit it. Thus, the pressure the IC will transfer to the crystals be-
low can be concentrated on some edges and surfaces, and we cannot say in advance
what the contact points will be.

The horizontal situation is different. We have the same load on each row since a
pushing mechanism (made with a spring) will be placed between the outer ring and
the crystals to push them inward with a force of approx. 50N. This will grant that
they will not move during transportation.

At the same time, it is important to underline that each crystal is wrapped with Ty-
wek and Tedlar, which creates a very compliance structure, whose behavior is hard
to predict. The stiffer the crystal matrix will be, the higher the localized pressures
will be, the lower the displacement of the inner ring will be. On the other hand, if
the crystal matrix will result very soft, the IC is capable to deform very easily, and
the containment constraint the side crystals can have, will be negligible. In any case
the interactions with the front and the back plane have been excluded. This choice
has two main reasons: (i) the stiffness of these two components is very low, because
of their structure and composition, so they can not contribute truly to supporting the
IC; (ii) we want to protect those components, so we need to avoid to load these com-
ponents during assembly. Indeed, in the assembling procedure, these components
will not be fastened until the loading crystal process will be ended.

In the next section the FEM models used for sizing the IC are presented.

6.2   FEM simulations

FEM simulations have been performed with Solidworks 2017 FEM software, and
some of the results have been verified with ANSYS simulations to check if the results
match.

The material used for the simulation was an elastic orthotropic model for the CF
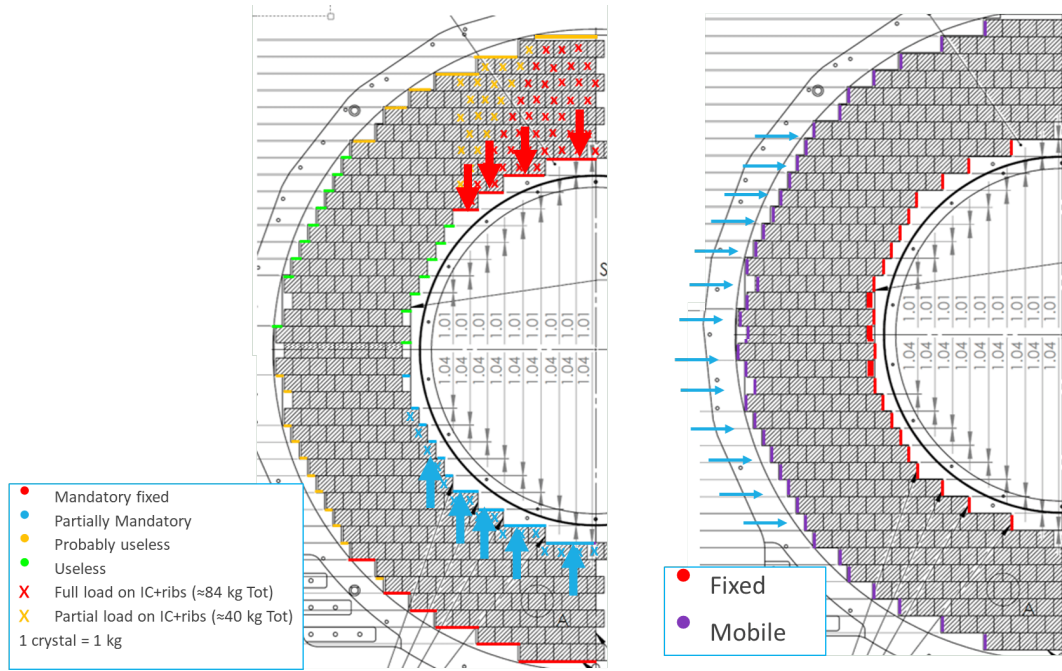and for the Al honeycomb, while an elastic isotropic model has been used for the

Figure 6.4: Vertical (left) and horizontal (right) contacts for the crystal matrix.

aluminum rings. The employed values are displayed in Figure 6.5.
In Figure 6.6 the three schemes of the horizontal model used are shown.

- Force model: the side crystals push the IC with a constant force, without controlling their displacement.

- Spring model: more similar to the reality, the force applied from crystals is related to their displacement, but at the same time it is difficult to estimate with precision the spring equivalent elastic constant.

- Fixed model: the horizontal displacement is fixed to zero, it means that the lateral IC surface cannot expand or contract.

The more realistic model is probably the spring model with a constraint as

$$F_i = k \cdot x_i + F_0 \tag{6.1}$$

where F_i is the horizontal force applied on the IC sides, F_0 is the preload we will apply during mounting, k is the elastic constant of a crystal row, and x_i is the horizontal displacement of IC sides. The problem of this formulation is the choice of k which is hard to estimate without an experimental tests of crystal rows.
The other two models are less realistic, but represent the upper and lower boundaries of what will happen and they were useful during simulations to predict our extreme possible conditions. Indeed, the force model is the situation when we have $k \to 0$, while the fixed model represents when $k \to \infty$.
In Figure 6.7 an example of comparison of the three models results is shown. The spring model has been used with two different k values, to show how outcome values can develop. The force can increase from 30N up to 230N per single layer, with a corresponding maximum deflection decrease from $1167\mu m$ to $56\mu m$. Because of

F-.220/193/50 Carbon Fiber + resin			3/8 0.003 Al Honeycomb		5052-H111 Aluminum		
Property	Value	Units	Value	Units	Property	Value	Units
Elastic Modulus in X	55000	N/mm^2	0.0068947573	N/mm^2	Elastic Modulus	71000	N/mm^2
Elastic Modulus in Y	55000	N/mm^2	0.0068947573	N/mm^2	Poisson's Ratio	0.33	N/A
Elastic Modulus in Z	7500	N/mm^2	689.4757296	N/mm^2	Shear Modulus	25900	N/mm^2
Poisson's Ratio in XY	0.04	N/A	0.5	N/A	Mass Density	2660	kg/m^3
Poisson's Ratio in YZ	0.04	N/A	0	N/A	Tensile Strength	270	N/mm^2
Poisson's Ratio in XZ	0.04	N/A	0	N/A	Compressive Strength		N/mm^2
Shear Modulus in XY	3000	N/mm^2	0.0068947573	N/mm^2	Yield Strength	115	N/mm^2
Shear Modulus in YZ		N/mm^2	165.4741751	N/mm^2			
Mass Density	1480	kg/m^3	337.8431075	N/mm^2			
Tensile Strength in X	550	N/mm^2	57.6656	kg/m^3			
Tensile Strength in Y	550	N/mm^2					
Compressive Strength in X	550	N/mm^2					
Compressive Strength in Y	550	N/mm^2					
Shear Strength in XY		N/mm^2					
Yield Strength	275	N/mm^2					

Figure 6.5: Material properties used for FEM simulations.

these results, it was difficult to find a configuration which does not create a very high concentrated stress on crystals, and having at the same time an acceptable deflection, which was stated as $< 100\mu m$.

About the vertical support contacts we analyzed two different scenarios (Figure 6.8) (right):

- the contact is localized at the outer edge (considering the expected IC deformation) of the lower steps (point support);

- the contact is distributed over the steps surfaces (line support).

As the horizontal constraints, these are two extreme situations, and the reality will stay in the middle.

In Figure 6.8 (right) it is possible to see the results of a simulation where the amount of CF layers were changed, and the effect on the upper surface displacement. In this analysis the crystal horizontal effect/constraint was removed. This will be used as comparison for the acceptance test we will perform at the manufacturer after the IC will have been built. The reality will probably stay in the middle of the red and blue line.

The other important information was that the amount of material used for the CF skins will relatively increase the structure stiffness by a factor of two, we could use 20 layers of CF, however this is improbable due to the quantity of material needed. Therefore, we decided to not increase stiffness using CF skins because of its modest contribution.

The other aspect to consider was which layer of crystals will support the structure. Indeed the IC can lay down on its first step, causing a major vertical displacement but a wider contact surface, or lay down on the other layers up to the 8th layer of crystals, with a minimum top vertical displacement but with a higher contact pressures. Of course a mixture of configurations are also possible. The outcome was that holding the IC from the higher layer creates very high pressure contacts, and the mechanism to adjust the contact surface would be difficult to realize. Moreover, it would touch just half crystal per side, and it was considered too risky.
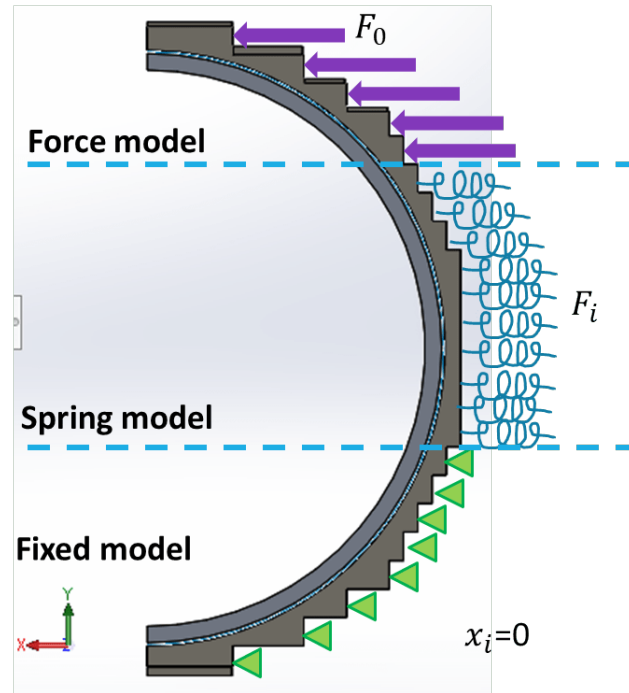
Figure 6.6: The analyzed three different horizontal constraint models.

	Force	Spring 1	Spring 2	Fixed
Preload [N]	30	30	30	N/A
k [N/m]	N/A	1.00E+06	1.00E+07	N/A
Max Stress (Mpa)	22.5	6.2	4.7	5.26
Location Max stress	Al bottom	Al bottom	CF bottom	CF bottom
Vertical deflection Al ring (Top) (um)	1167	168	86	56
Vertical deflection Zedex step (Top) (um)	1127	173	95	65
Horizontal deflection Al ring (Middle) (um)	554	30	16	0
Horizontal force sum (N)	510	900	1169	1192
Maximum horizontal force (N)	30	77	143	236

Figure 6.7: FEM results with the different models.

6.3   Inner cylinder final design and realization

After many simulations, the conclusion was that the IC has no problem about the resistance, because the stress in the structure is very low. The stiffness, on the other hand, is not high enough for the structure precision requirements, since it must be used as reference surface for many crystals. Because we are able to adjust the vertical deflection pushing with crystals by IC sides, we prefer to have a flexible structure, so limited amount of force will be required.

We do not want to stress the front and back plane, so they will be attached without tightening screws until the crystal installation process will end.

About vertical supports, we decided to make a thicker plane on the first level, with an adjusted mechanism which allows us to regulate vertical displacement offset during assembling. The same mechanism will be present on the next steps, in order to have a multiple adjusting mechanism in case of need.

The sandwich panel will be made of 1.4mm CF skins, made of 6 fabric layers each
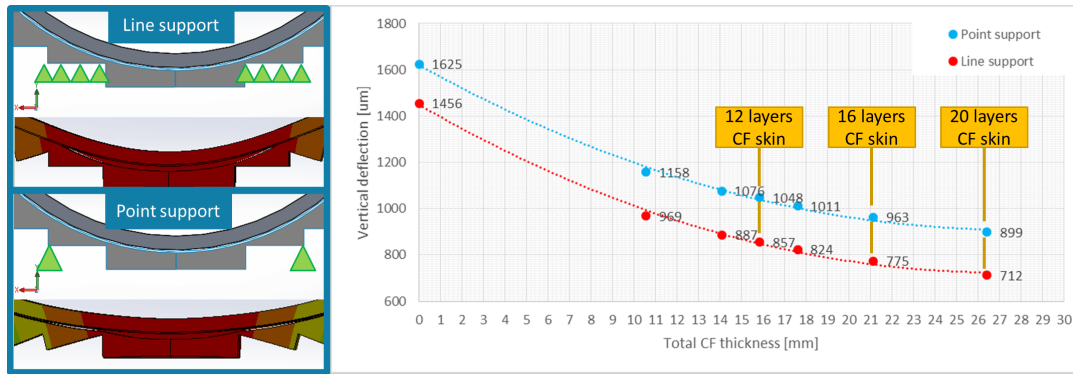
Figure 6.8: The different vertical constraint models (left). IC vertical deflection (i.e. the vertical variation of the diameter) vs the total thickness of CF sheets on ribs for the two different models without horizontal constraints (right).
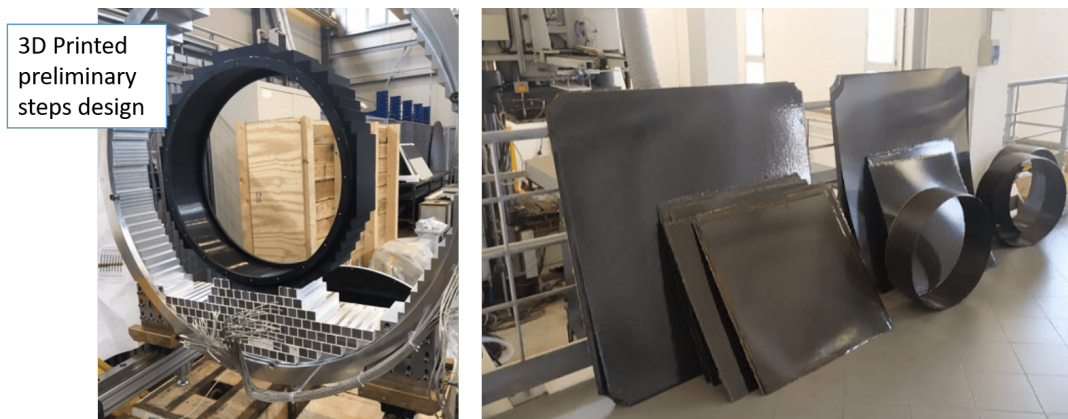

Figure 6.9: Test of a 3D printed IC structure on the mock-up at LNF (left). Some of the CF components realized at CETMA (right).

with a $0/90°$ orientation and cyanate ester resin and a core made of aluminum honeycomb (series 3003) 22mm thick, a cell size of 3/8", and a wall thickness of 0.003", with an average density of $50kg/m^3$ and with groove for outgassing.

Tunable nuts provide support from the bottom and optimize pressure distribution and CF plates create interface between ribs and crystals. L-shaped bended (4 plies-1 mm thick) CF brackets are placed to avoid detachment in the traction stress regions and pinhole references were placed to provide alignment. For assembling reason, steps ribs are made of two semi-circular halves to have a simple assembly/gluing procedure with the IC.

For the QC process, we will perform simplified structural tests on the semi-final sub-assemblies directly at CETMA to verify stiffness and mechanical resistance, then we will test the IC+ribs on the Aluminum disk mock-up at LFN. It this occasion we will test also the assembly procedures with the other calorimeter components (crystals, Al ring) and crystal piling up and also perform an outgassing test of the "Inner cylinder + steps".

The assembling procedure is summarized in the following steps:

1. Lay down the crystals of the 8 bottom layers.

2. Mount the IC, but fasteners to front-end plate and back-end plates will be loose.

3. Put a dummy weight (100 kg) on top of the IC to mimic the crystals weight.

4. Adjust lower screws and IC contacts on the lower crystal layers to control the top layers deflection.

5. Lay down the crystals of the central layers, and adjust horizontal pressure to control IC deformation (constantly monitor IC shape with dial indicators).

6. Remove dummy load.

7. Lay down crystals of the upper layers.

8. Adjust lower and lateral screws as necessary.

9. Tighten fasteners to the Source plate and Back plate.

Of course we need to test this procedure before to apply it.

At the moment of writing this Thesis, the design of the IC+ribs is concluded and the manufacturing is ongoing (Figure 6.9). CETMA is now working on the last parts and on the assembling structures and operations, and we are working together at the qualification procedure.

In Appendix 7.3 the technical drawings are presented.

Chapter 7

Pressure contact effects on crystal surface

Because of the IC design (chapter 7), a regulating device has been designed to adjust IC height during detector assembly. It consists of an aluminum nut embedded in the ribs, with a G10 screw accessible from the inner bore, which is the real element that supports the structure. To protect crystals beneath, a CF layer is placed between the screws and the crystals. In Figure 7.1 a drawing of the regulating design is shown. Because of the very small surface of the screw, a very high contact pressure is developed. Considering having eight adjusting mechanisms which distribute equally the IC load of approx. 1000N and a M10 screw with a contact diameter of 8mm, we will have an average pressure contact of:

$$\overline{p} = \frac{1000/8}{\pi 4^2} = 2.5 MPa \tag{7.1}$$

This value does not take into account the increase of pressure due to the Hertzian contact effect ([50]), and thus it will underestimate the real maximum contact pressure. If we do not place any material between the screw and the crystal, this pressure will push directly on crystal, damaging it.
Considering the CsI elastic limit (Figure 7.2):

$$R_{0.08\%} = 0.55 MPa \tag{7.2}$$

the average contact pressure can be a problem. Moreover, if we would like to take in consideration the possibility that during the adjusting procedure, we can accidentally load up to a couple of screws, the contact pressure can rise up to 10MPa. It will be too much for the crystal ultimate tensile stress load.
So we need to size properly the CF layer to interpose between the G10 screw and the crystals in order to avoid damaging crystals in unrecoverable manner, and this is the subject of this chapter.

7.1 FEM analysis

For the FEM analysis a very small portion of the model has been taken into account. A 2D axial symmetrical model has been defined, composed by a G10 peg of 8mm of diameter, a CF plate with a variable thickness, because it was the optimization purpose of this study, and a crystal chunk. A pressure of 2.5MPa as vertical load has been applied on the top surface of the peg, and the bottom of the crystal has been fixed. A not permeation constraint has been assigned to the three bodies, it means
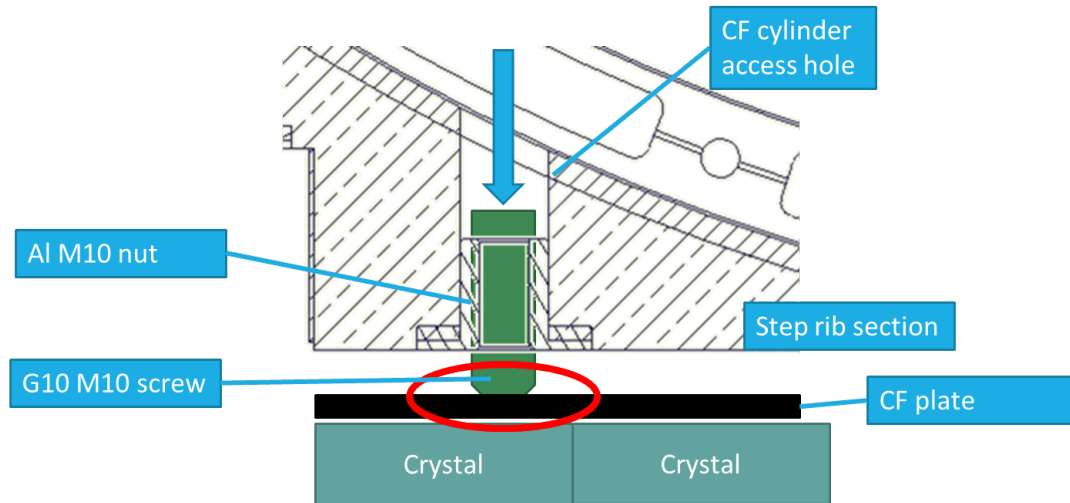
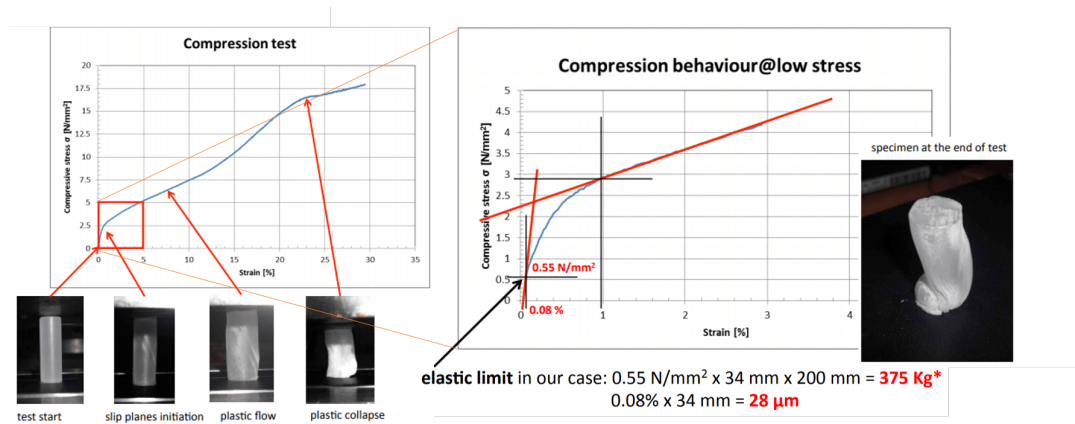**Figure 7.1:** Schematic drawing of the IC support regulating device.

Figure 7.2: CsI Compression test [49].

they are not bonded together but they are admitted to separate one to each other. All the materials have been considered elastic isotropic for a simpler analysis.

To reduce the calculation time, a mesh pattern has been assigned, having a finer and finer mesh, the closer the contact surface is. We can look at a picture of the preparation model in Figure 7.3. In Figure 7.4 Von Mises stresses and vertical displacement are presented. We can easily note the carbon fiber plate disengaging from the crystal surface when the load is applied.

A more interesting result is presented in Figure 7.5, where the pressure contact is displayed. We can see the Hertzian increase of pressure value on the outer border is present in the interaction between the peg and the CF plate, but it is totally absorbed and distributed, between the CF plate and the crystal, using a 1mm thick CF plate. In Figure 7.6 the effect on the maximum pressure on crystal surface of the CF plate thickness is presented.

Mesh has been refined to look at possible numerical errors, and it happened the maximum pressure obtained on the top CF plate depends on the mesh size (the peak value) and on the peg fillet radius, but the interaction between CF and CsI has no dependency on this.
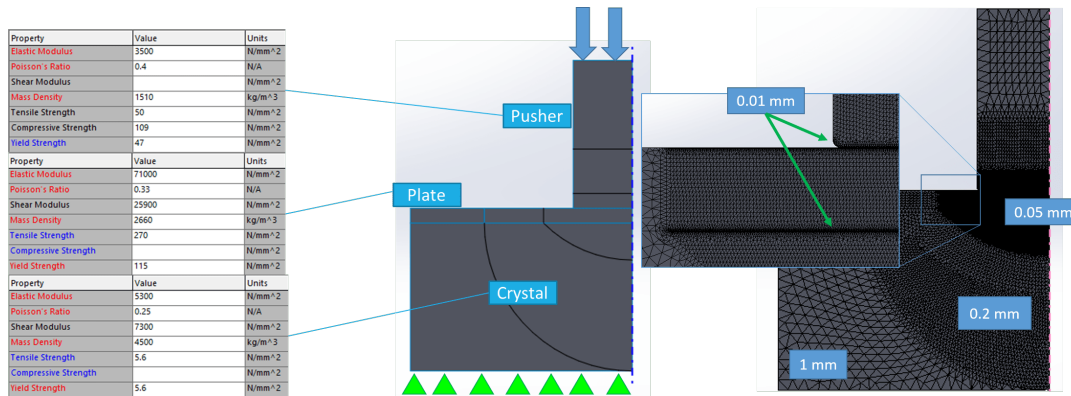
Figure 7.3: Contact pressure model with material properties used (left) and with the used mesh (right).
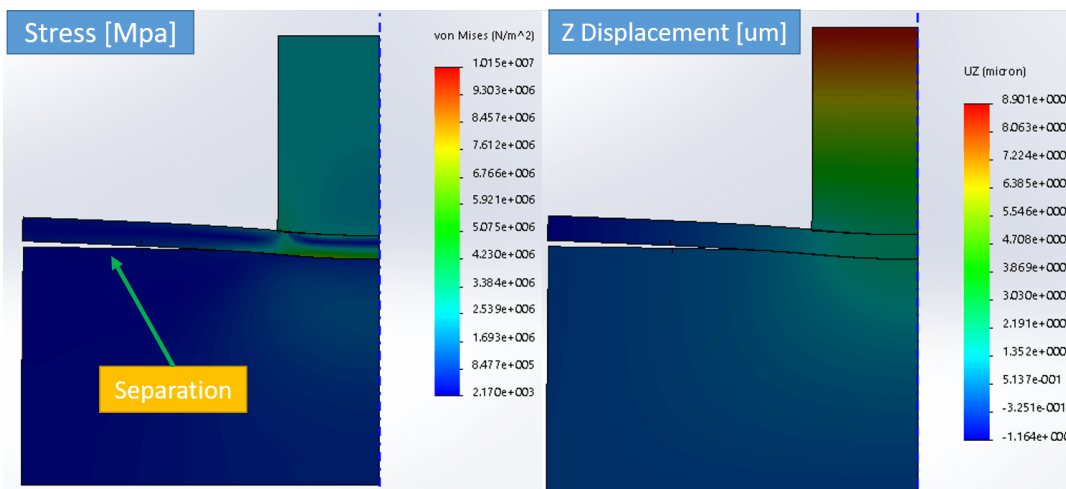
Figure 7.4: Numerical result from the FEM simulation with 1mm thick CF plate. Von Mises stresses are shown in the left image, while the vertical displacement is shown in the right image.

7.2 Set-up apparatus

To validate these numerical data and to test the interaction between the G10 screw and the crystals, a set-up has been developed to mimic the FEM analysis. The set-up was built in the cleanroom of Pisa INFN laboratory on a CMM machine (Figure 7.7 and Figure 7.8).

The set-up is made of an aluminum plate where the crystal is positioned, and a top aluminum surface that can move only vertically thanks to four cylindrical Teflon bushing on steel rods. On this aluminum top plate, there is a G10 peg (8mm diameter) in the bottom surface, which has a strain gauge mounted on its side to monitor the applied load. On the top surface the load is positioned, and it is composed of several 5kg lead blocks up to a total of 100kg.

The whole set-up has been placed on a CMM where it was possible to measure the CF plate deflection under load, and the crystal surface before and after the pressure has been applied, to verify if any footprint has been left from the load-unload cycle. This set-up has been used for three different CF plate thicknesses, in particular for 0.8, 1.6 and 2.6mm CF thick plates. We started with the thicker plate and we ended
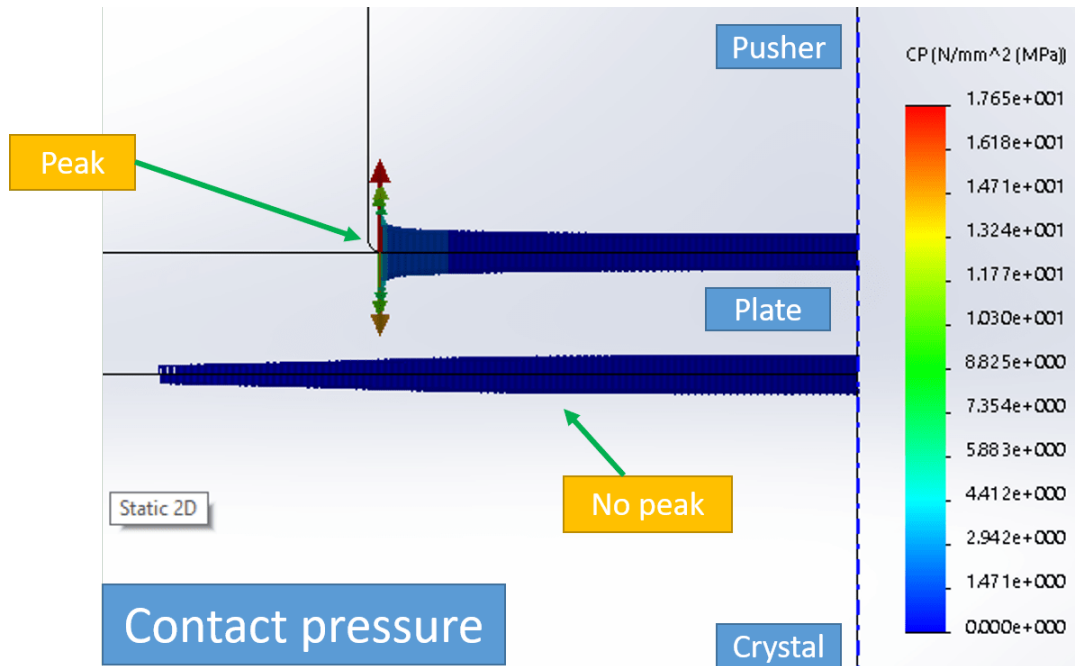
Figure 7.5: Numerical contact pressure result from the FEM simulation with 1mm thick CF plate.

with the thinner one, in order to have the worst loading condition at the end.

The measurement process started with the acquisition of the surface of the bare crystal with the CMM probe. Soon after the CF plate is inserted and the peg is lay down until it touches the CF plate. Then the CF plate is measured all around the peg with the CMM probe to register the starting condition.

Next, a load of 50kg is placed on top of the aluminum plate, and a new acquisition process begins, and the CF carbon fiber surface is measured. After another 50kg are placed on top, reaching the total amount of 100kg. It represents our worst case scenario, in which all pegs fail despite one. A new measurement is performed at this point.

Next, we remove all the lead blocks and the CF plate, and we measure again the top crystal surface to see if any permanent damage is present.

7.3 Results

The experimental results are presented in Figure 7.9 and Figure 7.10. In the first image we can look at the deflection the CF plates had during the loading process. It was useful to check if the FEM results are valid. In the side it is possible to look at a superimposed image, where the experimental data agree with the FEM model.

Unfortunately, an unexpected result was the permanent damage on the crystal surface. Despite no pressure over the yield point should have been reached, a footprint appeared on the crystal top surface. Moreover, it has increased more and more after different load cycle.

After some investigation, we concluded the reason this happened is that the peg and the CF surface was not perfectly coincident, and moreover, the bushing had a clearance, which permits a tilt of the upper platform. It has caused to concentrate all the
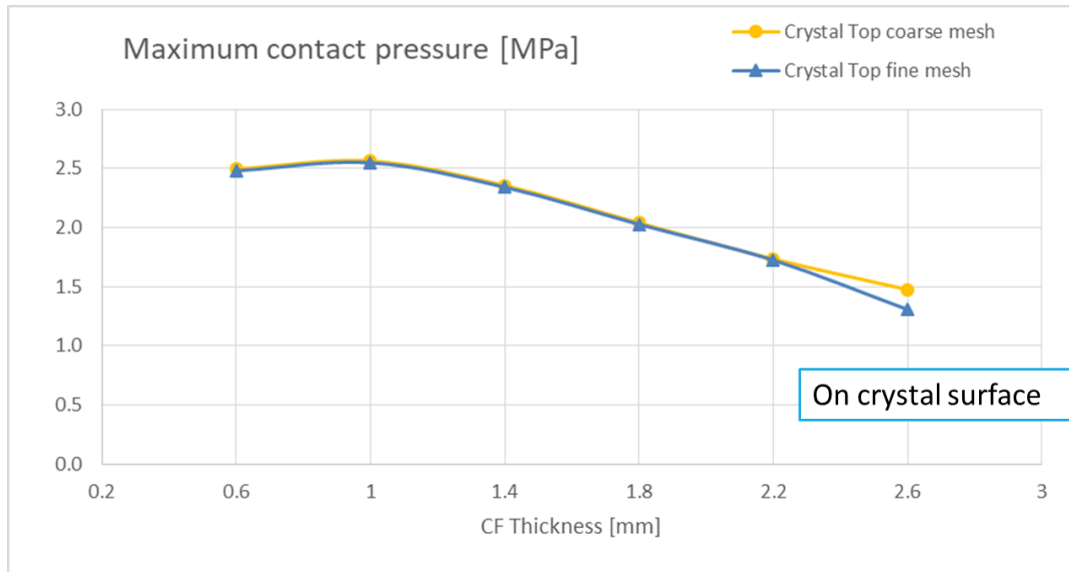
Figure 7.6: Numerical maximum contact pressure from the FEM simulation with variable CF plate thickness.

pressure not in a circle contact, but in a point, every time in a different randomly point of the peg surface. With this condition the pressure contact would have been higher enough to plastic deform the CsI. This happened during the load process, when load has been placed and it forced the structure to lean for a small period of time. Moreover, considering the CsI plastic properties, it can have a sort of viscous-plastic behavior.

We were able to confirm this hypothesis by a photoelastic measurement. Using a dummy plexiglass crystal, we tested the set-up and we have seen this concentration of stresses depending on the positioning of the weight (Figure 7.11).

Anyhow this kind of problem would have result also in the IC structure, because of the impossibility to have very high tolerances on these screws device. For this reason, we decided to use an auto adjusting foot made of PEEK, which can roll on the screw surface to be in a perfect contact with the CF plate beneath. This is now under construction and further tests.
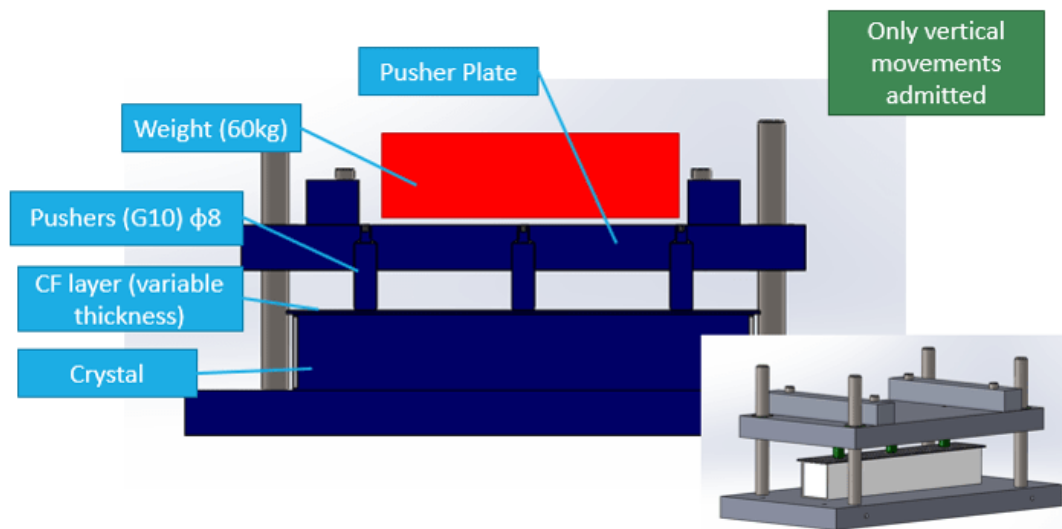
Figure 7.7: Set-up CAD model for the contact pressure on crystal.
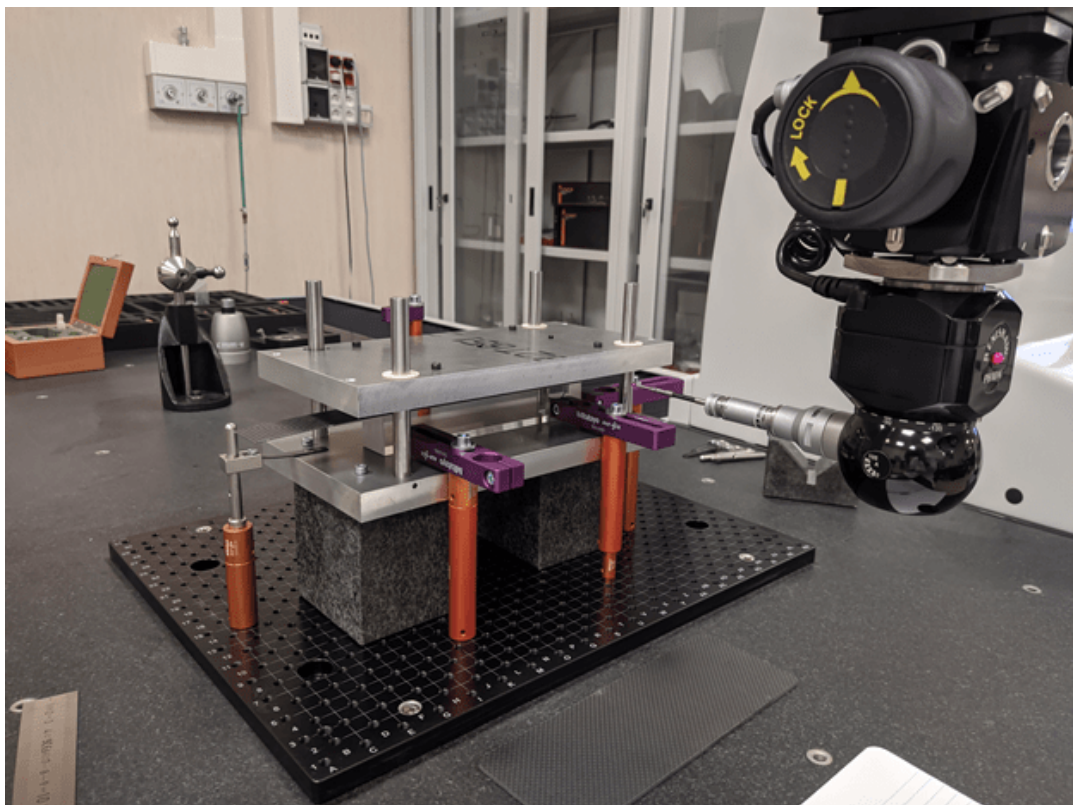
Figure 7.8: Set-up for the contact pressure evaluation built at the Pisa INFN laboratories.
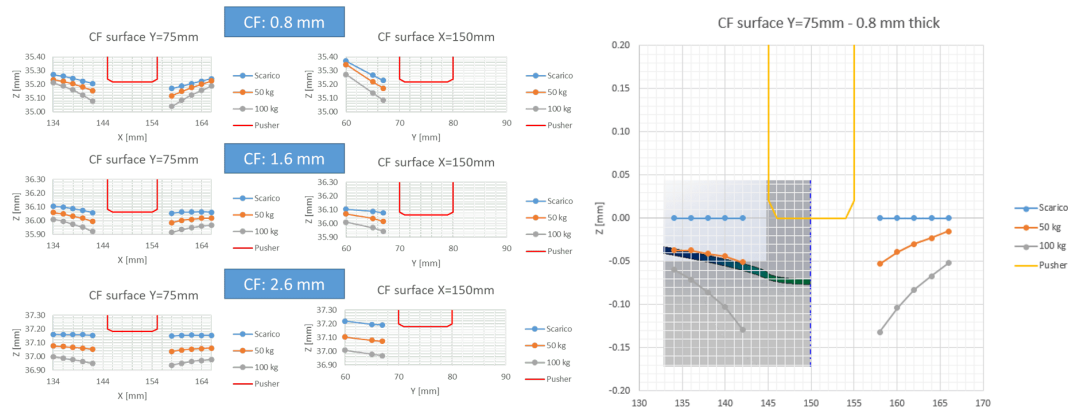
Figure 7.9: Experimental results with 0.8, 1.6 and 2.6mm CF thick plates. In the image the deflection of the carbon fiber plates measured on the CMM is presented. In the side image the concordance with the FEM simulation is presented, with superimposed images.
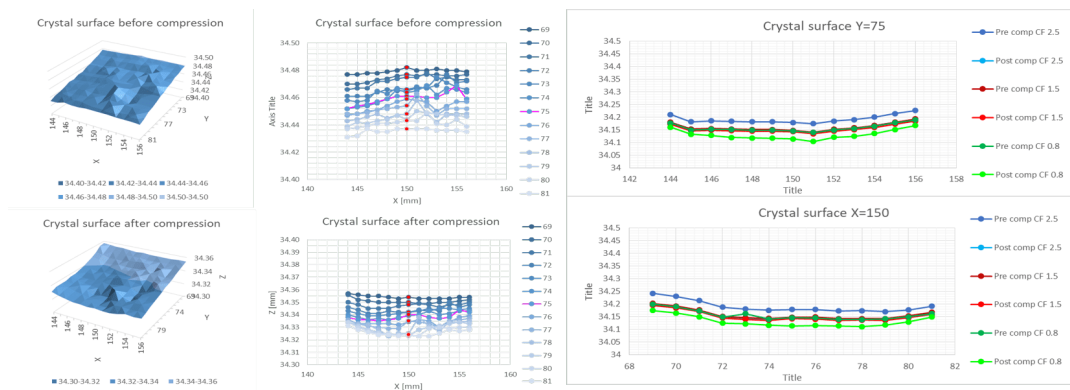

Figure 7.10: In the left image a 3D surface shows the acquired data from the CMM of the crystal surface before and after compression. In the left image two sections of the crystal surface are presented after three different load and unload cycles with the three different CF plates.
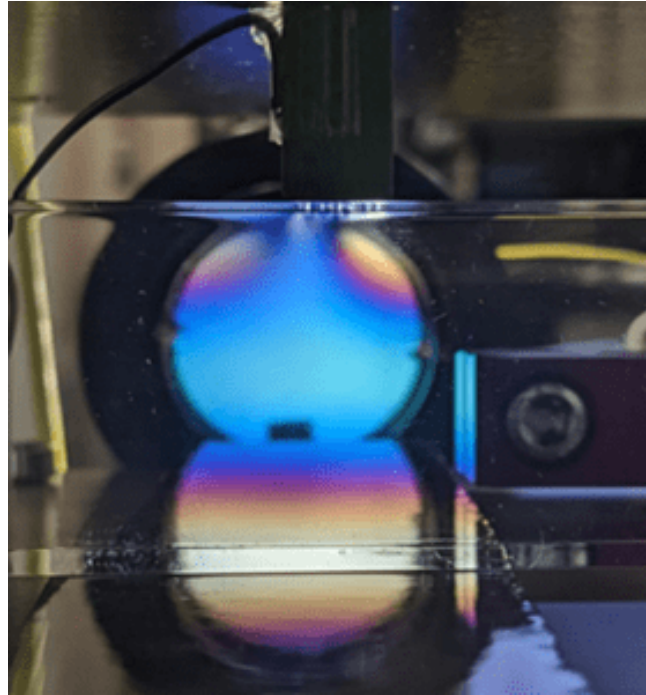
Figure 7.11: Photoelastic test on a plexiglass dummy crystal. It is possible to notice the stresses focuses just on a side of the peg.
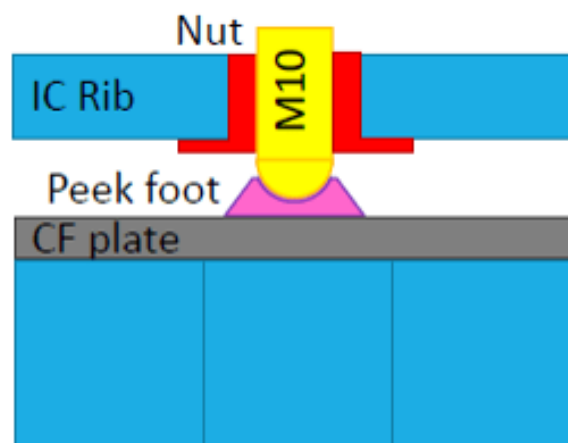
Figure 7.12: Scheme of the proposed feet to use on the IC G10 peg.

Conclusions and future prospects

The work reported in this Thesis has been dedicated to several important aspects of the development of the electromagnetic calorimeter of the Mu2e experiment at Fermilab.

Among these, the two most important aspects have been the mechanical structures design and optimization of the manufacturing processes, including the QC procedures, along with the study of the physical properties and characterization of the undoped CsI crystals, including the response to humidity.

Regarding the first subject, very detailed QC processes have been developed in order to obtain crystals with all the required characteristics.It included all the phases of a QC process, starting from the organization of the laboratory, with the necessary stations and procedures, the definition and realization of the required measurements, that led to the data analysis to the monitoring and correction of the production.

Starting from the outcome of the production, an analytic model for the crystal matrix structure dimensions has been developed, and it was necessary for the manufacturing of the aluminum ring, the IC and the Backplate, which are dependent to the crystal positions.

The final design of many components was also an important part of my work because of the tight time limits for building of the calorimeter [51]. As described in chapter 6 the IC was an important work to follow, also for the urgency to have this component ready in the near future, being a necessary part to proceed with the assembly, and one of the first components needed.Starting from a computer model, the IC has to deal with the production limitations and the crystals weaknesses, such as the very low yield point, taking in account the harsh environment it will be inserted in. Many analyses have been performed, which defined and optimized its dimensions. In particular the CF thicknesses have been chosen to avoid any damage to the crystals, since they are in contact between them. A FEM analysis has been done to mimic interferences between CF and CsI, and experimental tests have been defined and realized, showing FEM predictability and discrepancies.

The IC design was carried on in direct contact with the manufacturer in order to assure its feasibility and at this point it is at a good manufacturing point, single components have been realized but assembling is still to be done.

About the CsI properties, with this work, we started a characterization which will be useful for the future. Because of the limited number of applications undoped CsI crystals have been involved up to now, experience was more important than literature. Starting from the empirical evidence, a great effort has been made to create a set-up for the humidity induced damage, to assure a confident and reproducible results. The set-up has been further characterized and optimal parameters for CsI crystals have been identified. Moreover, the procedures and the equipment developed can be easily adapted to different type of crystals.

Some experiments have been made and first measurements have been recorded, showing the crystal behavior to humidity exposure environments and heat effects

on transmittance recovery. With this work we have started the process to define a mathematical characterization for the aspects described above, but since the experiment timescales were too long and we were impacted by logistic problem, such as traveling during the CoVid-19 pandemic, we are still in the data acquisition process. More analyses end experiments are in course and they will follow.

Since this type of crystal is gaining more and more interest , to have a good comprehension of its properties will be of course helpful. It regards not only the humidity tolerance, but also the mechanical properties, such as ambient temperature creep characteristic, which will be fundamental for further optimization in more spread CsI uses. Also developing procedures as heating cycles that can improve its transmittance will be a very good step in the future.

The next step will be a data acquisition campaign for the humidity CsI exposure tests. The tests will last one month each but before performing them we will need to solve some infrastructures problems in the lab, which allow us to be notified in case of power supply anomalies, because of the long time required by the tests.

With the manipulated crystals, new tests of the CsI baking will be held, considering the precise damage the crystals have got with humidity, and a monitoring at relativity high temperature will be implemented.
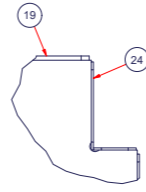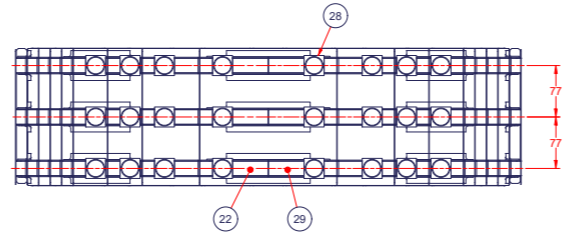
Technical Drawings

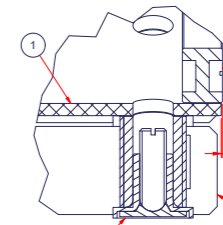In this appendix the INFN formal technical drawings for the IC construction are attached.

C (1 : 1)

B-B (1 : 4)

A-A (1 : 4)

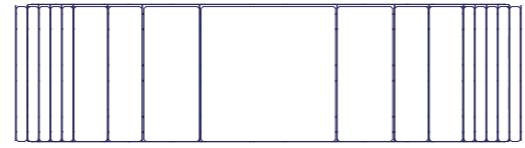A (1 : 1)

B (1 : 1)
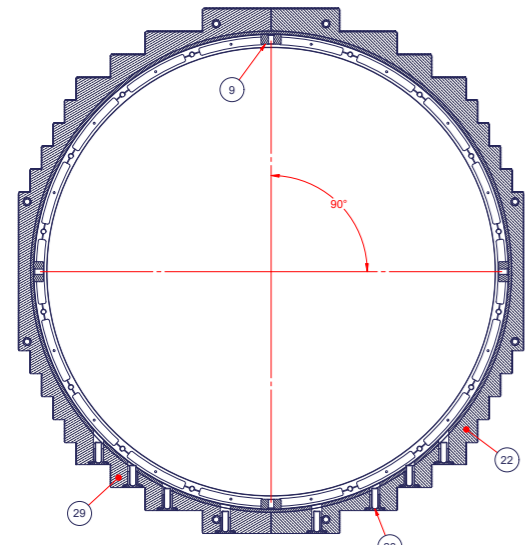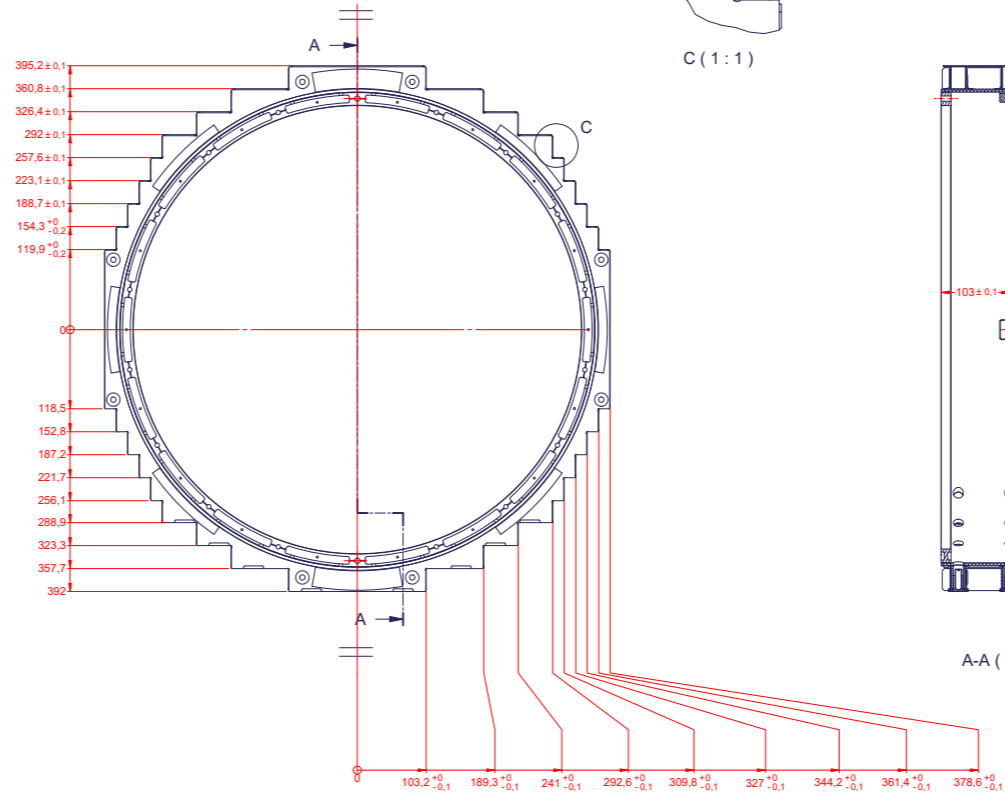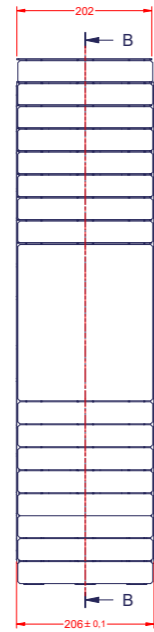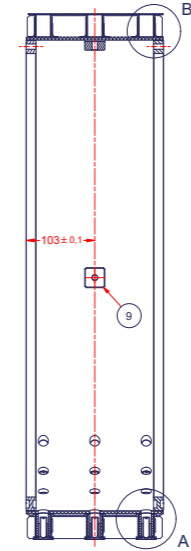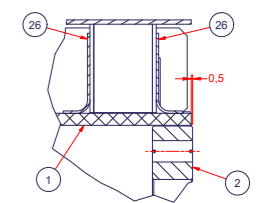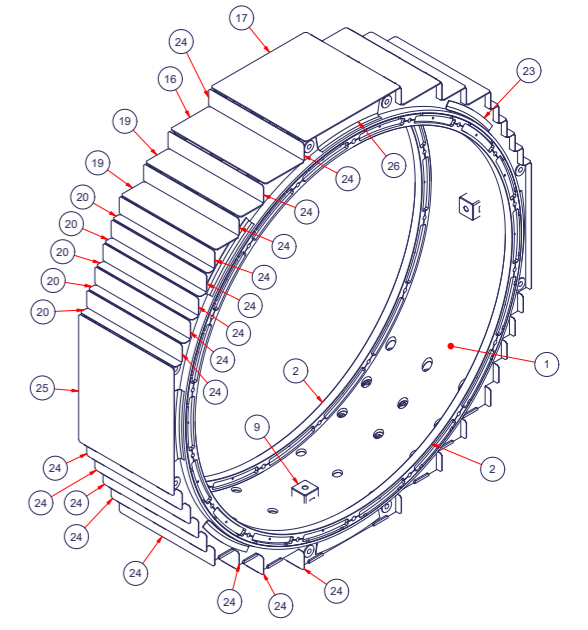
Parts List				
ITEM	QTY	PART NUMBER	DESCRIPTION	NOTE
1	1	Mu2e 08 00 00 - 01	Inner_Ring	
2	2	Mu2e 08 00 00 - 02	Reinforcerment_Ring	
9	4	Mu2e 08 00 00 - 05	Target Holder	
16	2	Mu2e 08 00 00 - 09	Plane	
17	1	Mu2e 08 00 00 - 08	Plane	
19	4	Mu2e 08 00 00 - 10	Plane	
20	10	Mu2e 08 00 00 - 11	Plane	
22	3	Mu2e 08 01 01 - 00	Inner Step	
23	36	Mu2e 08 00 00 - 04	CF Reinforcement	
24	32	Mu2e 08 00 00 - 20	V_Plane	
25	2	Mu2e 08 00 00 - 21	V_Plane	
26	12	Mu2e 08 00 00 - 03	Joint Reinforcement	
28	24	Mu2e 08 02 00 - 00	ADJ_Screw	
29	3	Mu2e 08 01 02 - 00	Inner Step	

INFN — Istituto Nazionale di Fisica Nucleare
LABORATORI NAZIONALI DI FRASCATI

Mu2e Experiment
EM Calorimeter

Inner_Ring

11,8 kg

WorkInProgress   1 of 1   Mu2e 08 00 00 - 00   0

1 : 4   A0

Beyond the crystals

In this appendix I will briefly present the other tasks I was involved with during my last three years working with the calorimeter group.
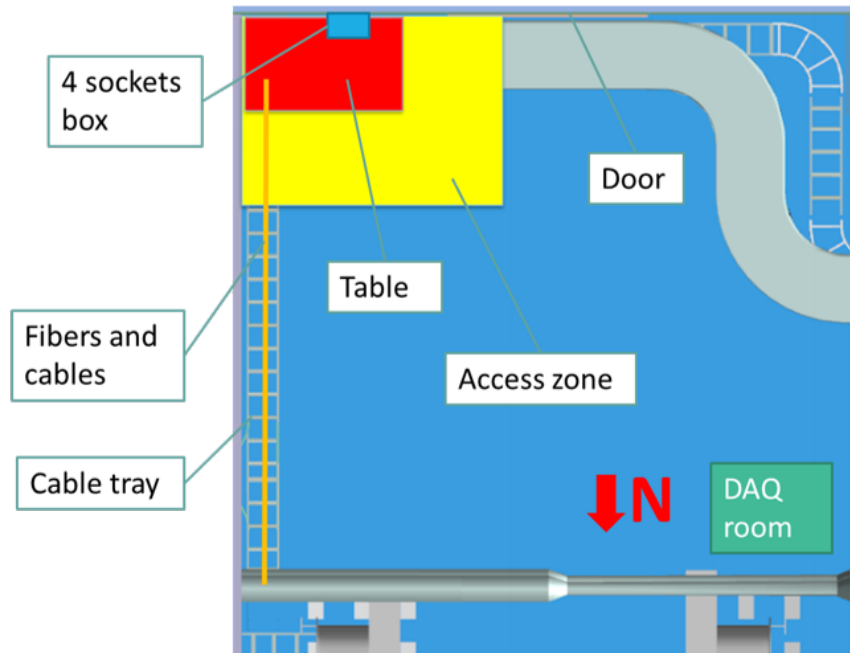
Figure 13: Plant of the DAQ room with the Laser station enlightened.

.1 The laser distribution system

A laser monitor system is used to control the photosensors gains, charge and timing resolutions, as well as to perform a fast equalization of time offsets. The overall system is presented in subsection 2.2.6. My work was focused on the organization of the laser station in the experimental apparatus, and the distribution system abroad the calorimeter [52].
The laser station is located out of the cryostat and it is made of:

- Laser primary distribution system [53];

- Digitizer board;

- pulse generator;

- scope;

- personal computer.

The laser is a 3B class category, and for this reason the whole system will be closed in a locked box with an interlock system. Before light will go out through fibers, there are attenuation filters, and it makes a Class 1 light emission, which will be safe also for accidentally fiber damage or breaking. The dedicated space for the station has been set up to a 3'×5' table with an access area of 3'. It will be placed in the DAQ room, in the South-East corner, and fibers will run along the ceiling cable tray, up to join the DAQ bundle cables to the IFB feed-through (Figure 13).
The main constraints the design had to deal with are:

- short term fiber bending radius of minimum 25 mm;
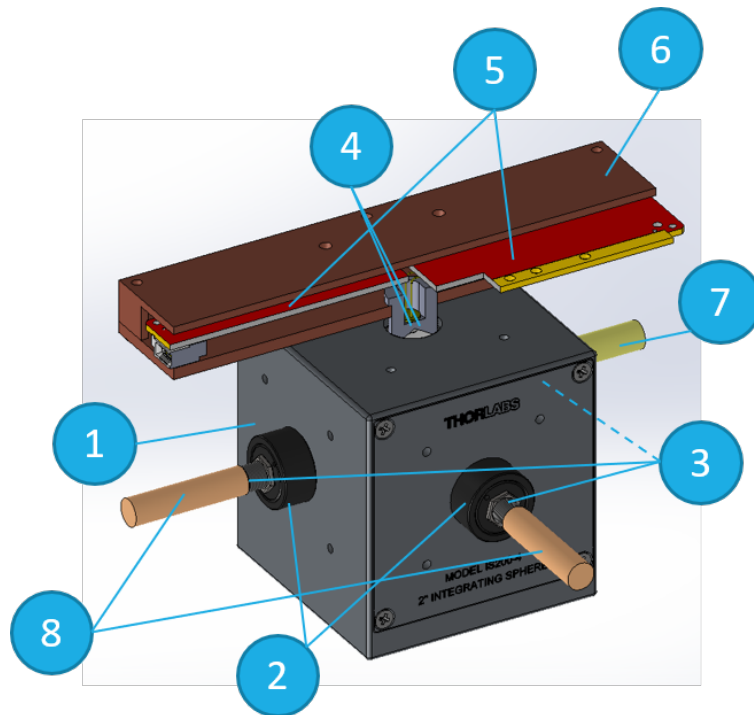
- long term fiber bending radius of minimum 50 mm;

Figure 14: Laser secondary distribution system: one sphere (1), two filters (2), three fiber connectors (3), two photodiodes (4), two FEE boards, with custom gain (5), one dedicated Faraday cage (6), one fiber inlet (7) and one bundle of fiber out (8). There are eight of these moduli on the calorimeter, four per each disks, and they are located between the crates.

- fit between two crates;

- leave space for Tracker alignment system;

- protection from radiation;

- dissipate heat (0.35 W per FEE);

- vacuum ok (no virtual leak, vacuum proof material);

- FEE electrically isolated;

- FEE easy to mount-dismount during maintenance;

- easiness to rout.

The secondary distribution system final design is showed in Figure 14 where all the components are listed. The showed modulus is mounted on a tungsten L-shaped shield to protect the electronics from the beam radiation, and they are grouped in a pair per each side of each calorimeter disk, for a total amount of 8 modulus. It is possible to look at a one fourth of the whole secondary distribution system in Figure 2.8.
The main characteristics are:

- the possibility to mount and dismount a Faraday cage without the help of a screwdriver, thanks to pear-shaped holes and a spring retaining system;
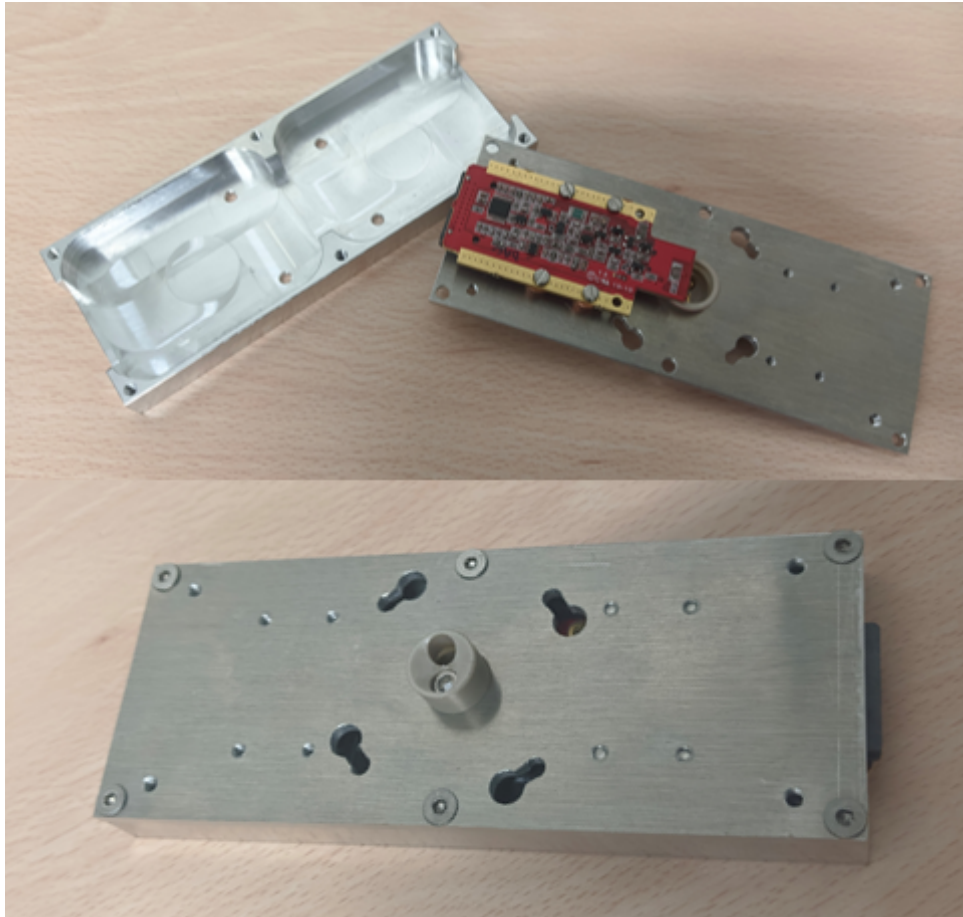
Figure 15: Prototype of laser Faraday cage with electronics.

- it is electrically and thermal isolated from the calorimeter structure;

- it will be cooled with the same cooling system of the crates, to have a good thermal stability;

- leaving a clear FOV for the calorimeter and the tracker.

From each sphere a bundle of 90 fibers will go to the SiPM holder, grouped in mini-bundle of 10 fibers each, with the same exact length. They will go to together to the IC, where they will spread to each holder location individually, organized by circular sectors. At the moment a prototype (Figure 15) of the Faraday cage has been realized in the Pisa INFN laboratories and it will be next tested in vacuum for thermal tests.

.2   The FEE cable system

A delicate matter of the calorimeter design was the FEE to Mezzanine board cables, not only for the electrical and signal problem, but also for the physical and maintenance requirements. There are indeed a very high number of cables, one per each FEE, and a very small space left for them [54] [55]. A lot of time has been spent to optimize the routing, to make cable resilient and to code each cable. In this section a glimpse of this work is presented.
The cable characteristics are:

PERFORMANCE DATA

Capacitance: 14 pF/ft (nominal)
Skew: 10 ps/m within pairs
Propagation Delay: 1.46 ns/foot
Flex Cycles: 8,000 cycles, single*
Current Rating: Single Conductor = 2.2 Amps*
Two Conductors = 1.6 Amps*
Shield DCR: 120Ω/1000ft
CC DCR: 164Ω/1000ft
Min. Bend Radius: .125"
Availability: Single, tape bonded
Temperature Rating: -40°C to 140°C, UL VW-1 Tested ***
DWV Working Voltage: 250 V****
Performance Rating:

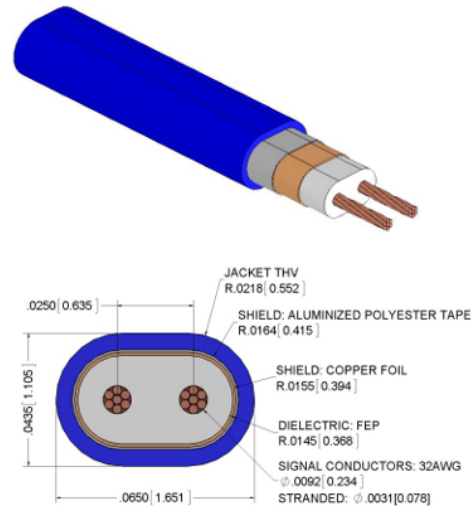| IL	.25m	1m
-3dB	14GHz	4GHz
-7dB	>20GHz	13GHz

Figure 16: TTF-32100-12-T01-TB Samtech patented cable used for FEE-Mezzanine connection with electro-mechanical characteristics.

Figure 17: The FEE cable connectors: the HDLSP at left and the ECDP-04-L2 at right.

- robust and easy to handle in the SiPM region;

- organized in circular sectors to distribute throughput in the DIRAC boards;

- divided tightly in Left/Right SiPMs groups;

- keeping same cable length for channels inside a sector;

- as much grouped as possible;

- reduced outgassing;

- cabled in a way that provide easy recognition;

- easy to disconnect also in the crate regions.

The used cable is the TTF-32100-12-T01-TB, that is a 32AWG Samtec cable suited for HV application at high frequency, with a THV jacket. It has been vacuum tested, with an outgassing rate of $5.6 \cdot 10^{-6} Torr \, l/s$ per 900m of cables (the whole calorimeter cable quantity), and it is radiation hard.
The cable has one single connector Mezzanine side, which connect four different FEEs of different crystals. The connectors we are going to use are a HDLSP and
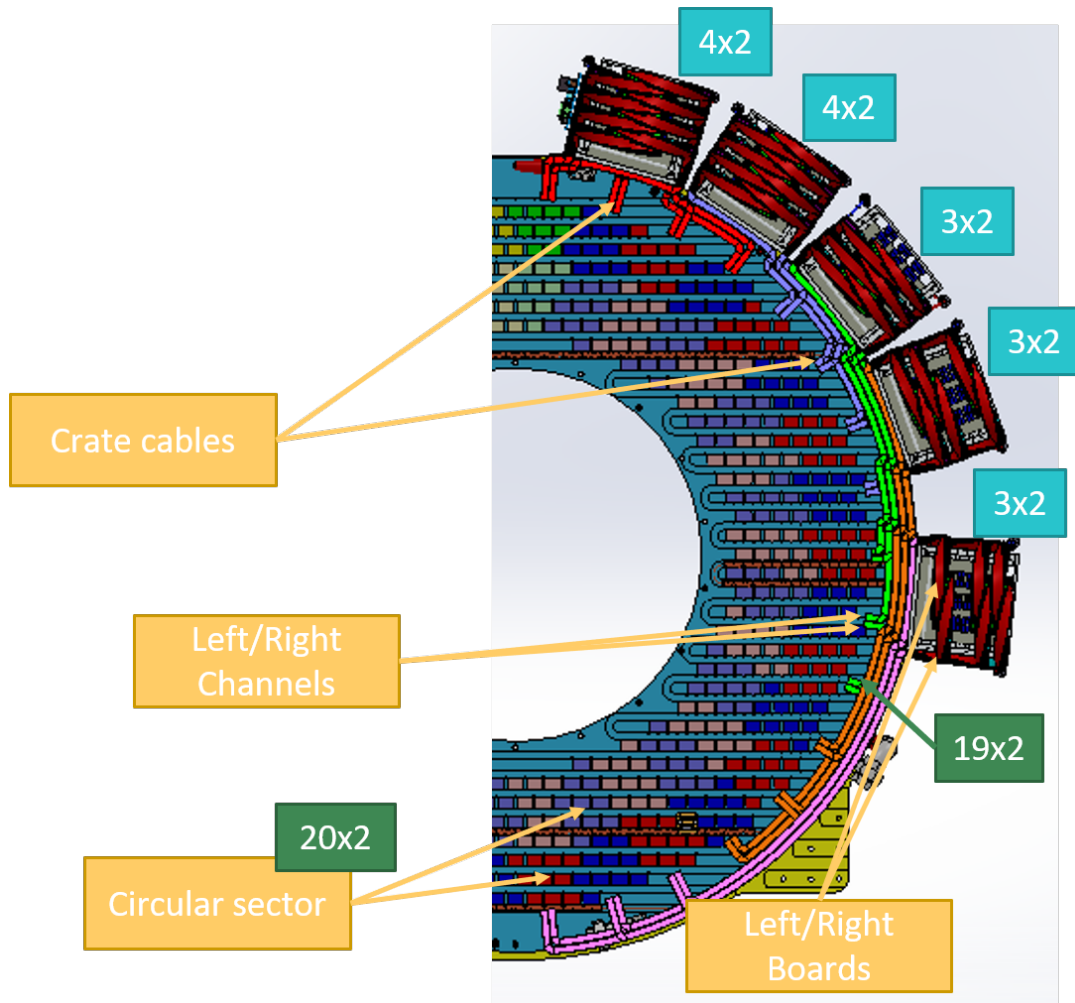
Figure 18: The FEE cable routing on half calorimeter disk. The light blue boxes represent the number of boards, and the green boxes represent the number of channels.

four ECDP-04-L2, each of them connected with six TTF duplex cable. The whole cable has been tested for magnetic permeability ($\mu_r < 0.01$), for outgassing rate ($7 \cdot 10^{-7} Torr\ l/s$ each) and for radiation hardness (>100krad).

The routing solution of the cables is that each disk is divided into two halves, each made of 17 circular sectors; Each board supplies a circular sector of 20 channels on 20 different crystals (apart 4 boards per disk which supply 19 channels); in each crate, half of the boards will supply the left channels, and the other half will supply the right ones and these boards will be adjacent; and there will be 8 boards in 4 crates and 6 boards in 6 crates (see Figure 18). The cables will be organized in ribbons in front of the crates to let an easy dismounting of connectors especially during further maintenance, when access space will be highly reduced, and to let to dismount a single board at time and they will be held in position by an aluminum rack fastened in the bottom of the crate, with a pushing mechanism to tight them up (Figure 19).

Each cable of each board will be of the same length, but for each board we will have different paths and lengths. The cables will run all along the outer ring, below the crates, to minimize the interference with the SiPM modules, and organized in different layers to do not cross each other. The cables will run in the central part of each
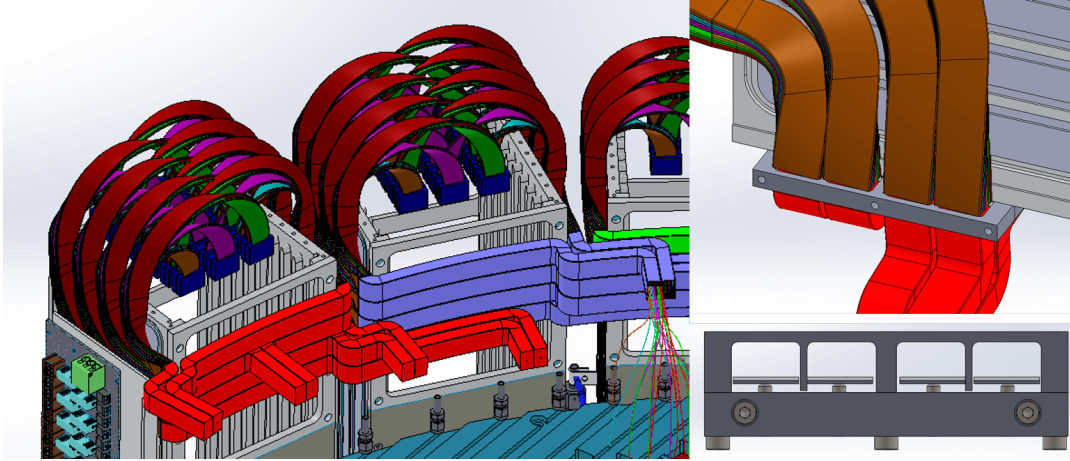
Figure 19: The FEE cable routing in front of the crate (left). The cable holding mechanism (right).

sector and spread to reach all the FEE board connectors. In Figure 20 a technical drawing of the cable routing in showed.

About the codification, each cable will be identified with a unique code, made of number and letters, which will help during the assembling procedures and the future maintenance. It will be composed in the following way:

$$d\# - p\# - c\# - b\# - s\# - h\# - r\# - l\# / x\#y\# \tag{3}$$

Where # can assume a different value according with the following legend:

- d [0,1]: represent the calorimeter disk;

- p [0,1]: represent the disk half (because there is a vertical symmetry);

- c [0,1,2,3,4]: represent the half disk crate;

- b [0,1,2,3]: represent the crate board;

- s [0,1]: represent the SiPM on a module (because there is 2 SiPMs per each module);

- h [0,1]: represent the board height connector position;

- r [0,1]: represent the board row connector position;

- l [0,1,2,3]: represent the connector location for each sub-cable (as explained before, there is 1 to 4 hydra cable);

- x [0:28]: represent the crystal horizontal position;

- y [0:36]: represent the crystal vertical position.

In Figure 21 it is possible to look at the channel-cable codification map example.

To help the manufacturing, cable lengths have been reduced to 16 different lengths, and to help the mounting procedures, cables will be pre-shaped and clamped before the installation on the calorimeter. To do this a set-up and a procedure have been realized (Figure 22). Some preliminary mock ups have been realized at Sidet Laboratory, where two boards have been connected (Figure 23).
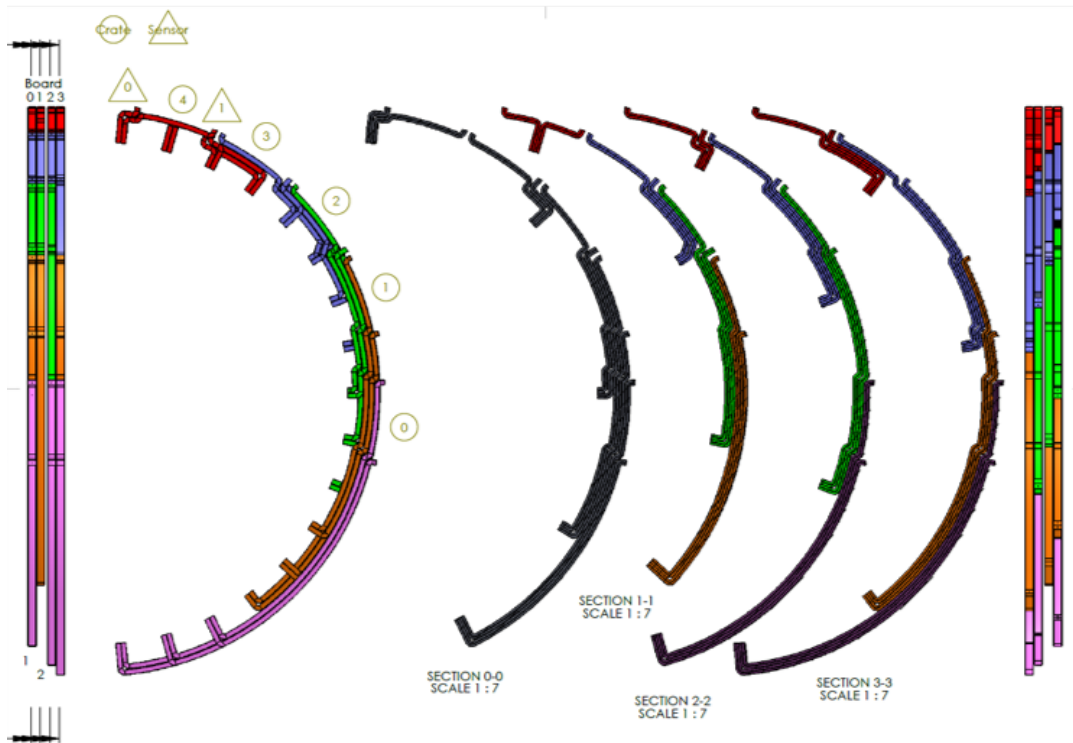
Figure 20: The FEE cable routing drawing in front of the Backplane.

.3 Assembling Cleanroom

For the assembly of the two calorimeter disks of the Mu2e detector, a room must be built at Fermilab. This room will be a temporary enclosure that will last for the estimated time for the assembling process, and then dismounted. The main operations that must be performed inside the room are:

- cleaning components (electronics, pipes, mechanics);

- storage of cleaned components (electronics, pipes, mechanics);

- degassing of crystals;

- assembling of the two disks;

- test of the two disks both mechanically and electronically;

- storage of the two disks (until the transfer to the experimental site).

To perform these activities there is a needing of an environment controlled room, in particular a low level for RH is required (below 40%) because of the sensitivity of the CsI crystal to humidity (see chapter 5). A good level of cleanness is strongly recommended, and a class 10000 (ISO 7) has been defined as required target. The designed site for this room is under the dome of the LabA at SiDet at Fermilab in order to be close to the QA room where most the components are stored and most of the instrumentation is already present.
The already existing QA Room must be directly connected to the assembly room, to move easily component from one room to the other one, and it will be used as
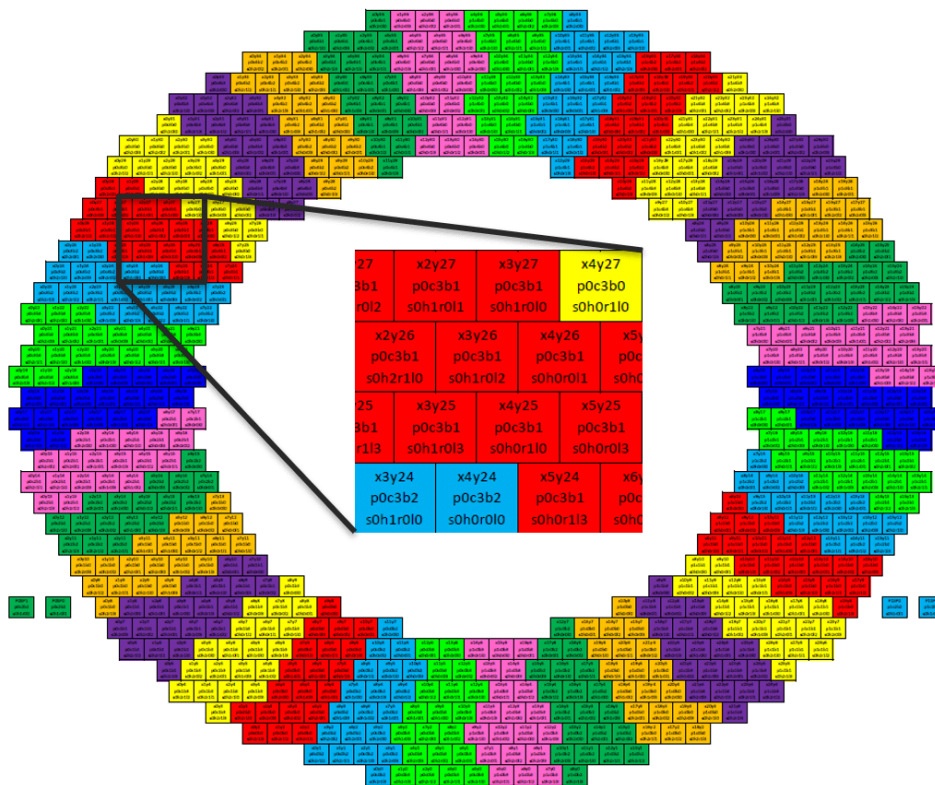
Figure 21: The FEE cable map referred to crystal location. The 4 out of the disk location represent the Laser calibration SiPMs

grey room, where all the cleanroom garments will be worn. One entrance for the incoming and out-coming of the bigger components directly connected with the main hall was necessary, and it will be used with only this goal. A second door has been installed for safety purposes.

For the installation of the cleanroom two main options have been taken in account: a brand-new economical cleanroom, made by Unistrut profiles and a plastic wrap, or to recycle a dismissed 100 class cleanroom from the Argonne Laboratories. After having evaluated the modifications needed to adapt the existing cleanroom and the economic impact to build the two solutions (see [56]), the second option have been chosen.

Starting from the existing components a new layout has been designed to fit in the dedicated location. An important modification was to remove the filtering air system in part of the cleanroom to permit the usage of a mobile crane for the mechanical installation of the crates and the back and front plane., despite the loss of cleanness level. In this way part of the cleanroom has 8 feet height clearance to make easier the installation of the components. The cleanroom indeed has been divided in two areas, the dirtier and taller dedicated for the mechanical installation of the components, and the cleaner for the installation of all the electronic boards and testing. In this latter area, a cooling station pipeline will be installed to cool the calorimeter under testing operation, which are planned to turn half disk a time. Moreover, a nitrogen flux supply has been installed in the cleanroom, which satisfy safety requirement, to flux nitrogen inside the calorimeter once the crystals have been installed, to
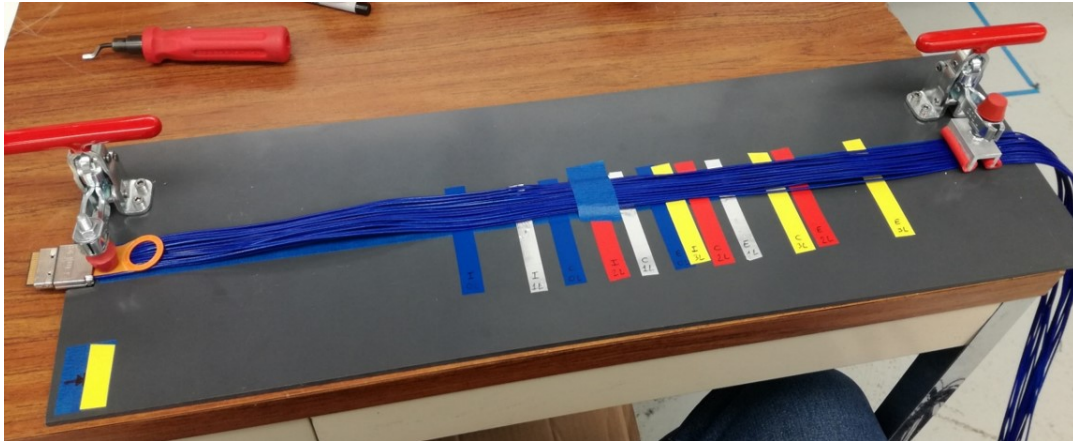
Figure 22: The FEE cable set-up to shape cables in the final form

protect from moisture. Indeed, the humidity level will be kept, thanks to a double de-humidification system, at 30%RH. A lower value will make a very uncomfortable environment for people which require to stay in the cleanroom for long period of time. In Figure 24 the most important sizes of the cleanroom are showed.

For the installation, Fermilab required a detailed procedures plan [57]. After the installation, the internal layout of the stations have been carried out, considering the required space for all the operations and the space needed for safety requirements [58]. In Figure 25 it is possible to see the actual layout.

At the moment (March 2021) the cleanroom has been finished for the structure and services installation, and equipment is started to be installed inside (Figure 26). In Appendix .3 the technical drawings for the cleanroom building are attached.

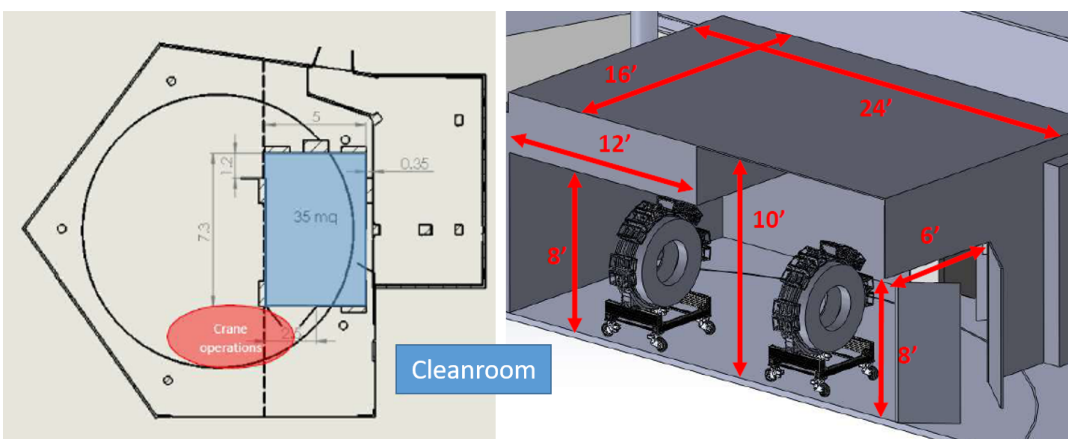**Figure 23:** The FEE cable set-up to shape cables in the final form

Figure 24: CAD image of the cleanroom plant (left) and a 3D view with the most important dimensions (right)
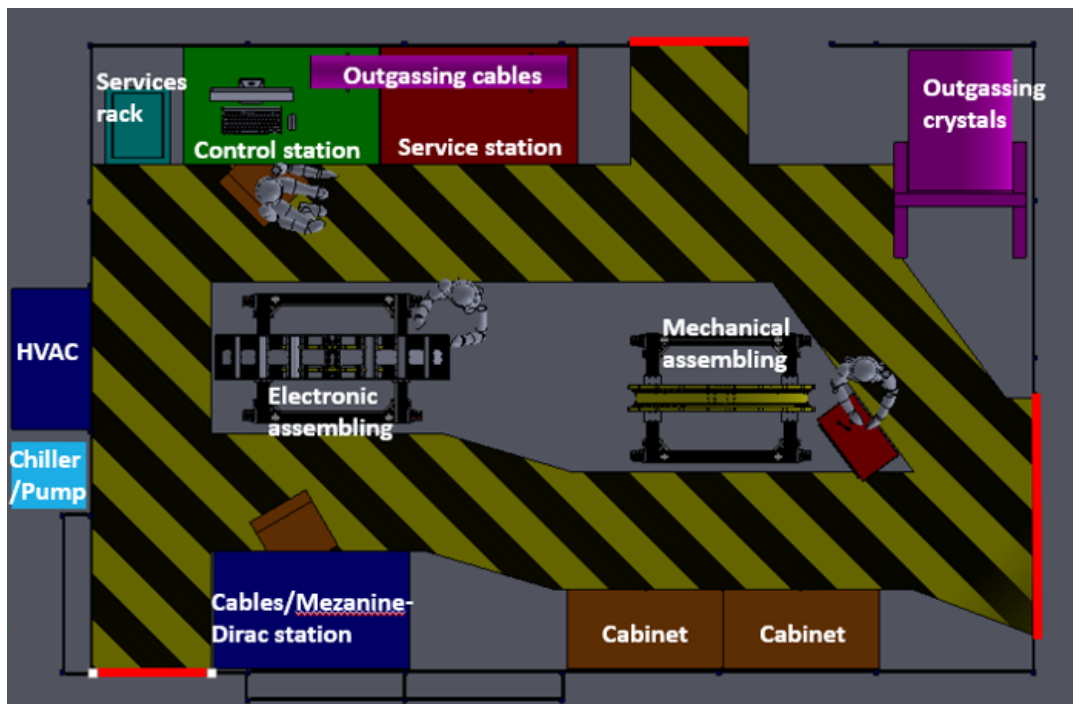
Figure 25: The cleanroom layout with all the necessary stations required for assembling and testing.

Figure 26: A picture of the cleanroom layout taped on the floor before the installation (left). A picture of the actual cleanroom installed at SiDet (right).
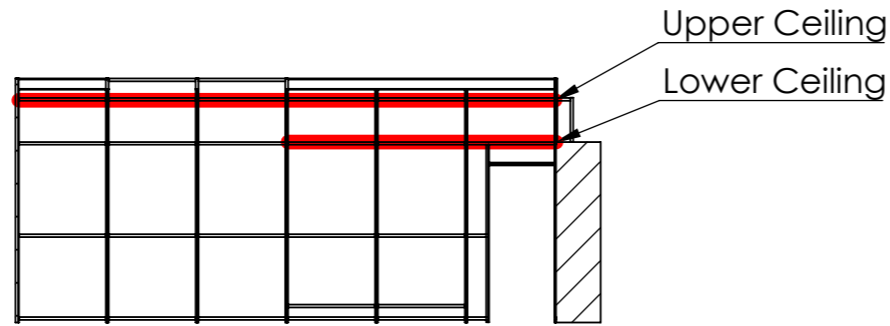
Cleanroom Technical Drawings

In this appendix the technical drawings for the Fermilab cleanroom construction are attached.
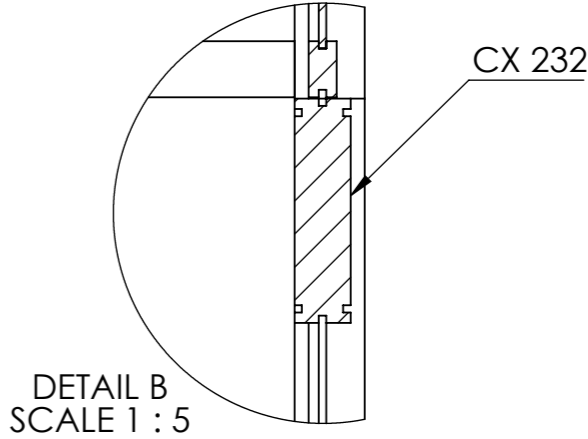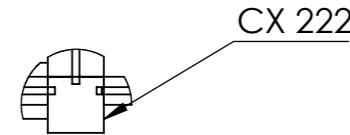
Upper Ceiling
Lower Ceiling

SECTION X-X
SCALE 1 : 100
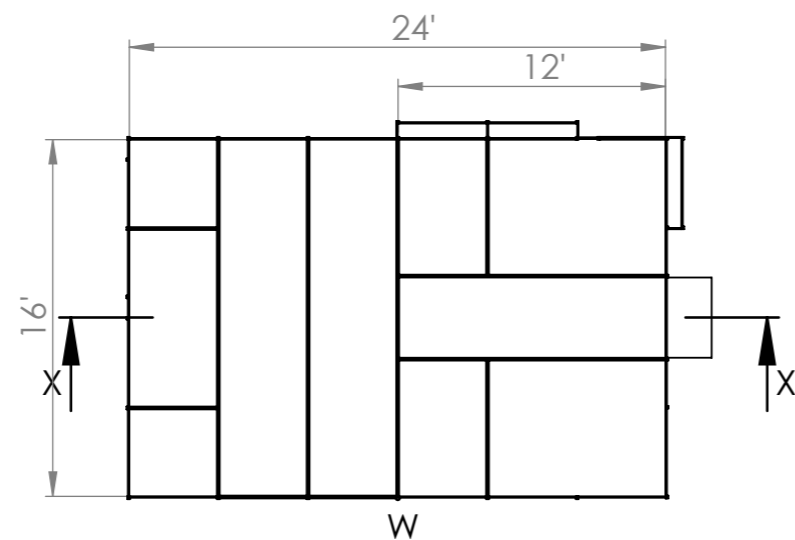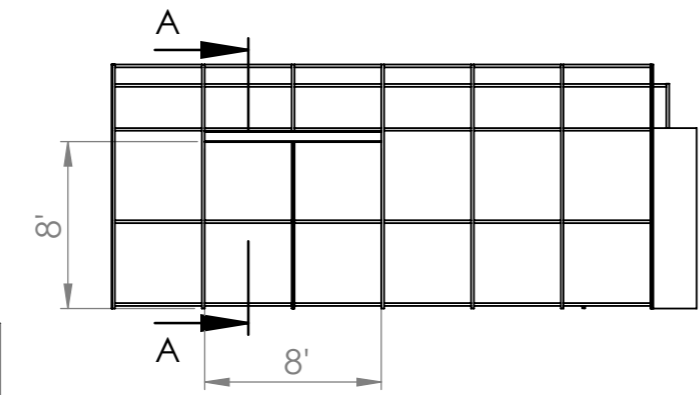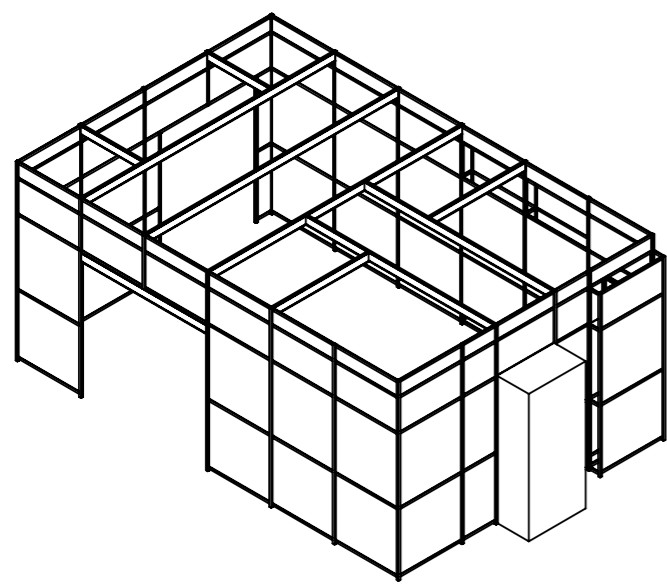
CX 232

DETAIL B
SCALE 1 : 5

CX 222

DETAIL W
SCALE 1 : 5

24'
12'
16'
X
X
W

A
A
8'
8'

B

SECTION A-A
SCALE 1 : 100

UNLESS OTHERWISE SPECIFIED:			NAME	DATE
DIMENSIONS ARE IN INCHES	DRAWN			
TOLERANCES:	CHECKED			
FRACTIONAL ±				
ANGULAR: MACH ± BEND ±	ENG APPR.			
TWO PLACE DECIMAL ±				
THREE PLACE DECIMAL ±	MFG APPR.			
INTERPRET GEOMETRIC	Q.A.			
TOLERANCING PER:				
MATERIAL	COMMENTS:			
FINISH				

NEXT ASSY   USED ON
APPLICATION

DO NOT SCALE DRAWING

TITLE:

SIZE DWG. NO.   REV
B CleanRoom

SCALE: 1:50 WEIGHT: SHEET 1 OF 1

Num. articolo	Num. parte	Size	Quantità
1	Cx221^CleanRoom	10'	4
2	Cx222^CleanRoom	11'	12
3	Cx226^CleanRoom	11'	3
4	Cx226^CleanRoom	10'	1
5	Cx230^CleanRoom	11'	9
6	Cx211^CleanRoom	1'	8
7	Cx211^CleanRoom	4'	19
8	Cx211^CleanRoom	2'	3
9	Cx232^CleanRoom	8'	1
10	Cx232^CleanRoom	6'	1

HVAC

30

120

607.50

	NAME	SIGNATURE	DATE			TITLE:
DRAWN						
CHK'D						
APPV'D						
MFG						
Q.A				MATERIAL:		DWG NO.

CleanRoom

A3

WEIGHT:

SCALE:1:50

SHEET 1 OF 1
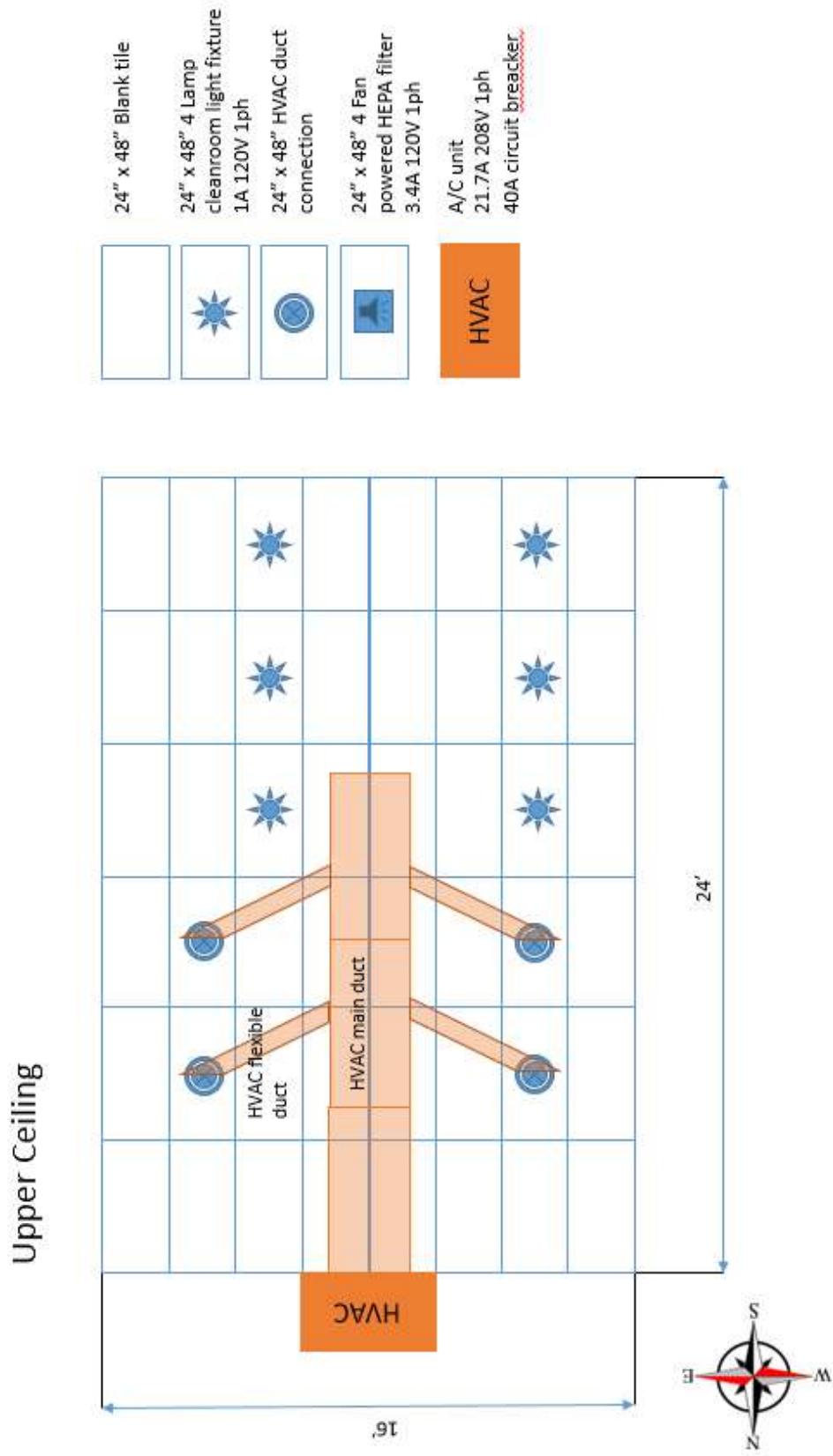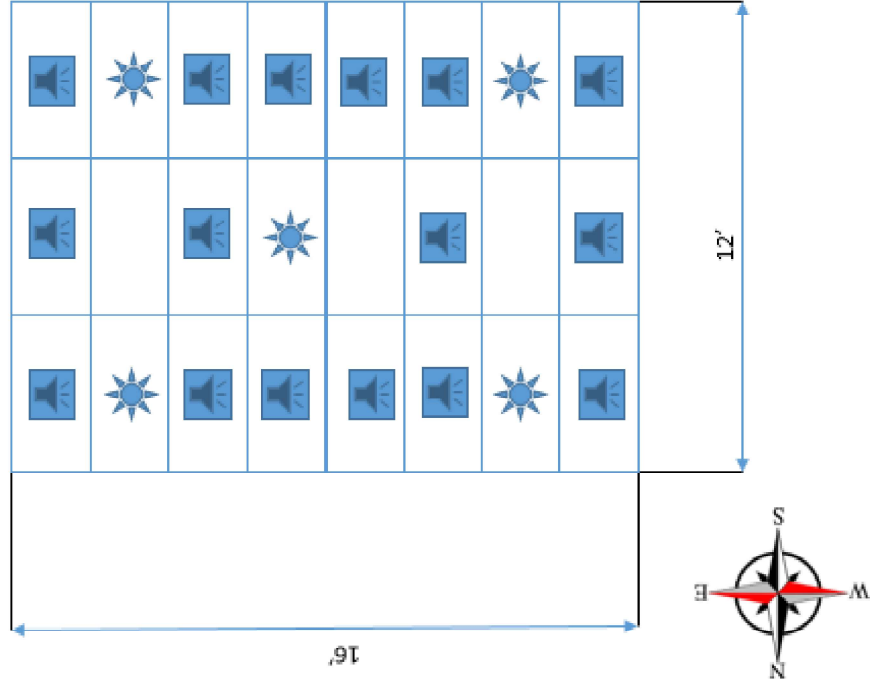
5   Drawings

Legend:
- 24″ x 48″ Blank tile
- 24″ x 48″ 4 Lamp cleanroom light fixture 1A 120V 1ph
- 24″ x 48″ HVAC duct connection
- 24″ x 48″ 4 Fan powered HEPA filter 3.4A 120V 1ph
- HVAC — A/C unit 21.7A 208V 1ph 40A circuit breacker

Upper Ceiling

HVAC flexible duct

HVAC main duct

HVAC

16'

24'

Lower Ceiling

Legend

Symbol	Description
(blank tile)	24" x 48" Blank tile
(light)	24" x 48" 4 Lamp cleanroom light fixture 1A 120V 1ph
(duct)	24" x 48" HVAC duct connection
(fan)	24" x 48" 4 Fan powered HEPA filter 3.4A 120V 1ph
HVAC	A/C unit 21.7A 208V 1ph 40A circuit breacker

16'

12'

Bibliography

[1]   L. Bartoszek et al. *Mu2e Technical Design Report*. 2015. arXiv: 1501.05241.

[2]   Guido Altarelli. *The Standard Model of Particle Physics*. arXiv:hep-ph/0510281: CERN-PH-TH/2005-206.

[3]   G. Aad et al. "Observation of a new particle in the search for the Standard Model Higgs boson with the ATLAS detector at the LHC". In: *Physics Letters B* 716.1 (2012), 1–29. ISSN: 0370-2693. DOI: 10.1016/j.physletb.2012.08.020. URL: http://dx.doi.org/10.1016/j.physletb.2012.08.020.

[4]   S. Chatrchyan et al. "Observation of a new boson at a mass of 125 GeV with the CMS experiment at the LHC". In: *Physics Letters B* 716.1 (2012), 30–61. ISSN: 0370-2693. DOI: 10.1016/j.physletb.2012.08.021. URL: http://dx.doi.org/10.1016/j.physletb.2012.08.021.

[5]   Wilhelm H. Bertl et al. "A Search for muon to electron conversion in muonic gold". In: *Eur. Phys. J. C* 47 (2006), pp. 337–346. DOI: 10.1140/epjc/s2006-02582-x.

[6]   Fermilab. *History of Fermilab*. URL: https://history.fnal.gov/history-fermi.html.

[7]   Fermilab. *Why are we called Fermilab?* URL: https://news.fnal.gov/2017/01/why-are-we-called-fermilab/.

[8]   James L. Popp. "The MECO experiment: a search for lepton flavor violation in muonic atoms". In: *Nuclear Instruments and Methods in Physics Research Section A: Accelerators, Spectrometers, Detectors and Associated Equipment* 472.3 (2001), 354–358. ISSN: 0168-9002. DOI: 10.1016/s0168-9002(01)01270-0. URL: http://dx.doi.org/10.1016/S0168-9002(01)01270-0.

[9]   G. Pezzullo and P. Murat. "The calorimeter-seeded track reconstruction for the Mu2e experiment at Fermilab". In: *2015 IEEE Nuclear Science Symposium and Medical Imaging Conference (NSS/MIC)*. 2015, pp. 1–3. DOI: 10.1109/NSSMIC.2015.7581921.

[10] O. Atanova et al. "Measurement of the energy and time resolution of a un-doped CsI + MPPC array for the Mu2e experiment". In: *Journal of Instrumentation* 12.05 (2017), P05007–P05007. ISSN: 1748-0221. DOI: 10.1088/1748-0221/12/05/p05007. URL: http://dx.doi.org/10.1088/1748-0221/12/05/P05007.

[11] Raffaella Donghia. "Performance studies for the electromagnetic calorimeter of the Mu2e experiment af Fermilab". MA thesis. Rome, Italy: Università Tor Vergata, 2015.

[12] N. Atanov et al. "Measurement of time resolution of the Mu2e LYSO calorimeter prototype". In: *Nuclear Instruments and Methods in Physics Research Section A: Accelerators, Spectrometers, Detectors and Associated Equipment* 812 (2016), 104–111. ISSN: 0168-9002. DOI: 10.1016/j.nima.2015.12.055. URL: http://dx.doi.org/10.1016/j.nima.2015.12.055.

[13] N. Atanov et al. "Design and status of the Mu2e electromagnetic calorimeter". In: *Nuclear Instruments and Methods in Physics Research Section A: Accelerators, Spectrometers, Detectors and Associated Equipment* 824 (2016), 695–698. ISSN: 0168-9002. DOI: `10.1016/j.nima.2015.09.074`. URL: `http://dx.doi.org/10.1016/j.nima.2015.09.074`.

[14] The Mu2e Project et al. *Mu2e Conceptual Design Report*. 2012. arXiv: `1211.7019 [physics.ins-det]`.

[15] Raffaella Donghia on behalf of the Mu2e calorimeter group. *Design, R&D and status of the crystal calorimeter for the Mu2e experiment*. 2016. arXiv: `1607.01301 [physics.ins-det]`.

[16] Raffaella on behalf of the Mu2e calorimeter group Donghia. *Performance study of single undoped CsI crystals for the Mu2e experiment*. Feb. 2016. arXiv: `1602.02983`.

[17] M. Angelucci et al. "Longitudinal uniformity, time performances and irradiation test of pure CsI crystals". In: *Nuclear Instruments and Methods in Physics Research Section A: Accelerators, Spectrometers, Detectors and Associated Equipment* 824 (2016), 678–680. ISSN: 0168-9002. DOI: `10.1016/j.nima.2015.11.042`. URL: `http://dx.doi.org/10.1016/j.nima.2015.11.042`.

[18] Saint Gobain. *Saint Gobain web page*. URL: `www.crystals.saint-gobain.com`.

[19] Valeri Saveliev. "Silicon Photomultiplier - New Era of Photon Detection, Advances in Optical and Photonic Devices". In: *IntechOpen* (2010). DOI: `10.5772/7150`. URL: `https://www.intechopen.com/books/advances-in-optical-and-photonic-devices/silicon-photomultiplier-new-era-of-photon-detection`.

[20] Hamamatsu. *TSV MPPC array*.

[21] N Yahlali et al. "Imaging with SiPMs in noble-gas detectors". In: *Journal of Instrumentation* 8.01 (2013), C01003–C01003. ISSN: 1748-0221. DOI: `10.1088/1748-0221/8/01/c01003`. URL: `http://dx.doi.org/10.1088/1748-0221/8/01/C01003`.

[22] Luca Morescalchi et al. "Automated Test Station for the Characterization of Custom Silicon PhotoMultipliers for the Mu2e Calorimeter". In: June 2019, p. 017. DOI: `10.22323/1.343.0017`.

[23] S. Di Falco et al. "Components Qualification for a possible use in the Mu2e Calorimeter Waveform Digitizer". In: *Journal of Instrumentation* 12.03 (2017), C03088–C03088. ISSN: 1748-0221. DOI: `10.1088/1748-0221/12/03/c03088`. URL: `http://dx.doi.org/10.1088/1748-0221/12/03/C03088`.

[24] Bertrand Echenard et al. *Source calibration system design*. Internal presentation: `Mu2eDoc12464`.

[25] Vincenzo Incorvaia et al. *Design of the cooling system of the Mu2e Electromagnetic Calorimeter at Fermilab*. Internal presentation: `Mu2eDoc34256`.

[26] Francesco Ruiu. "Design and thermal analysis of the Mu2e electromagnetic calorimeter cooling system at Fermilab". In: *Università di Pisa* (2017-2018).

[27] Leonardo Lucchesi. "Design, thermal analysis and validation test of the Mu2e electromagnetic calorimeter cooling system at Fermilab". In: *Università di Pisa* (2016-2017).

[28] N. Atanov et al. *The Mu2e Calorimeter Final Technical Design Report*. 2018. arXiv: `1802.06341 [physics.ins-det]`.

[29] *Amcrys official page*. URL: `http://www.amcrys.com/`.

[30] *Siccas official page*. URL: `http://www.siccas.com/`.

[31] M. Cordelli et al. *QA of 72 pre-production un-doped CsI crystals from SICCAS, Amcrys and Saint Gobain*. Feb. 2016. Internal note: `Mu2eDoc20074`.

[32] Pasciuto Daniele on behalf of the Mu2e calorimeter group. *Calo QA Lab at SiDet, Info and documents*. Internal report: `Mu2eDoc16988`.

[33] Eleonora Diociaiuti. "Study of the Mu2e sensitivity to the $\mu^- \to e^+$ conversion process". In: *Università degli studi Tor Vergata* (2019-2020).

[34] M. Cordelli et al. *Summary of CsI crystals production and related QA tests*. Internal presentation: `Mu2eDoc35564`.

[35] Daniele Pasciuto et al. *Dimensional control of un-doped CsI crystals: methodology and production results*. Internal report: `Mu2eDoc20859`.

[36] Daniele Pasciuto. *Survey of second SICCAS pre-series crystals*. Internal presentation: `Mu2eDoc15522`.

[37] Daniele Pasciuto et al. *CsI crystal piling up tolerances in Mu2e Calorimeter*. Internal report: `Mu2eDoc22223`.

[38] Daniele Pasciuto. *Crystal piling up measurements & Assembly room status*. Internal presentation: `Mu2eDoc18327`.

[39] Stefano Miscetti et al. *Production Crystal Specifications for Mu2e*. Internal document: `Mu2eDoc7051`.

[40] Alessandro Saputi. *CsI, SiPM and SiPM holders drawing*. Internal document: `Mu2eDoc22220`.

[41] E. Blucher et al. "Tests of cesium iodide crystals for an electromagnetic calorimeter". In: *Nuclear Instruments and Methods in Physics Research Section A: Accelerators, Spectrometers, Detectors and Associated Equipment* 249.2 (1986), pp. 201 –227. ISSN: 0168-9002. DOI: `https://doi.org/10.1016/0168-9002(86)90669-8`. URL: `http://www.sciencedirect.com/science/article/pii/0168900286906698`.

[42] Ronald E. Ray. "The KTeV pure CsI calorimeter". In: *Conf. Proc. C* 940925 (1994). Ed. by H. A. Gordon and D. Rueger, pp. 110–115.

[43] P. N. Shanahan. "The performance of a new CsI calorimeter for the KTeV experiment at Fermilab". In: *Frascati Phys. Ser.* 6 (1996). Ed. by A. Antonelli et al., pp. 717–726.

[44] *Interdipartimental Crystal Research & Analysis Center official page*. URL: `https://www.dicea.univpm.it/icrys`.

[45] Daniele Pasciuto on behalf of the Mu2e calorimeter group. *The Inner Cylinder and steps*. Internal presentation: `Mu2eDoc33758`.

[46] Daniele Pasciuto on behalf of the calorimeter group. *Inner Cylinder Design*. Internal presentation: `Mu2eDoc33177`.

[47] Daniele Pasciuto et al. *Inner Ring Heating System*. Internal presentation: `Mu2eDoc35445`.

[48] *CETMA official page*. URL: `http://www.cetma.it/index.aspx`.

[49]   Franco Grancagnolo on behalf of the Mu2e calorimeter group. *Stress test of calorimeter crystals*. Internal presentation: `Mu2eDoc8675`.

[50]   H. Hertz, D. E. Lenard P. translated by Jones, and London: Macmillan Schott G.A. "Hertz, H., 1896. On the contact of elastic solids". In: *Miscellaneous Papers, Chapter V, pp.146-162* (1896).

[51]   N. Atanov et al. "Construction status of the Mu2e crystal calorimeter". In: *Journal of Instrumentation* 15.09 (2020), pp. C09035–C09035. DOI: `10.1088/1748-0221/15/09/c09035`. URL: `https://doi.org/10.1088/1748-0221/15/09/c09035`.

[52]   Daniele Pasciuto et al. *Laser diffusive spheres mounting*. Internal presentation: `Mu2eDoc28462`.

[53]   Carlo Ferrari. *Short Report on Calorimeter Laser System*. Internal presentation: `Mu2eDoc27067`.

[54]   Daniele Pasciuto on behalf of the calorimeter group. *FEE cabling and fibers - Mu2e Calorimeter CRR*. Internal presentation: `Mu2eDoc24483`.

[55]   Daniele Pasciuto on behalf of the calorimeter group. *Description and routing of Calorimeter FEE-MB cables*. Internal presentation: `Mu2eDoc29916`.

[56]   Daniele Pasciuto. *Estimate cost for mu2e Calorimeter assembling room*. Internal presentation: `Mu2eDoc20122`.

[57]   Daniele Pasciuto. *Assembling procedure for the calorimeter temporary cleanroom at SiDet, LabA*. Internal presentation: `Mu2eDoc22133`.

[58]   Daniele Pasciuto. *Assembly Clean room update*. Internal presentation: `Mu2eDoc24882`.